Alma Mater Studiorum – Università di Bologna

DOTTORATO DI RICERCA IN

MECCANICA E SCIENZE AVANZATE DELL'INGEGNERIA

Ciclo XXX

Settore Concorsuale: 09/C2

Settore Scientifico Disciplinare: ING-IND/18

DESIGN, CHARACTERIZATION AND OPTIMIZATION OF PLASMA ASSISTED PROCESSES FOR THE TREATMENT AND SYNTHESIS OF HIGH VALUE-ADDED MATERIALS

Presentata da: Enrico Traldi

Coordinatore Dottorato **Supervisore**

Prof. Marco Carricato **Prof. Vittorio Colombo**

Esame finale anno 2018

"Man's highest activity is searching for the truth. It is the factor which distinguishes us from animals, and our specific activity is to grasp the truth in all its forms."

-Georges Lemaître

“To be sure, it is not the fruits of scientific research that elevate man and enrich his nature, but the urge to understand, the intellectual work, creative or receptive.”

-Albert Einstein

INDEX

Introduction

In the last decades, the continuous technological progress in the scientific, industrial and biomedical fields has led to a growing demand of advanced functional materials, *i.e.* materials that are prepared or modified to address a specific application. The production of these high value-added materials usually requires the development of new processes and the optimization and improvement of conventional ones in order to obtain the desired properties and to be economically competitive.

Plasma assisted processes proved to be a fundamental technology to produce advanced functional materials. Indeed, the wide choice of plasma sources with their peculiar physics and chemistry, with pressures ranging from few Pascals to high pressures (one to tens of bars) and temperatures varying from room temperature to 10-25 kK, makes it possible to treat and synthesize several kinds of valuable polymeric, metallic and ceramic materials for countless industrial applications. While some plasma processes have been thoroughly studied and they are now commonly used in large scale production systems, such as low-pressure plasmas for the fabrication of electronic devices or Radio Frequency (RF) thermal plasmas for nanoparticles synthesis, other ones have been implemented in industrial systems only recently or are still under preliminary scientific studies, such as Cold Atmospheric Plasmas (CAP) for materials treatment.

The ever-changing demands of innovative materials from several scientific and industrial fields make it necessary to study and to optimize the more established plasmas technologies, thus consolidating and widening their key-role in the production of high valued-added materials. At the same time, these demands have fostered the efforts of the scientific researchers to further comprehend the complex mechanisms governing the physics of CAPs in order to disclose their full potentialities. Indeed, the flexibility, the simple scalability and the environmentally friendliness of CAPs make them a promising and valuable technology for industry, provided that an effective and reliable control of their effects is guaranteed. Therefore, a constant and interdisciplinary research focused on the investigation and development of plasma assisted

processes is essential to successfully employ different technologies in the realization of valuable innovative materials.

During my Ph.D. studies at Alma Mater Studiorum-Università di Bologna, I have been thoroughly involved in the activities of the Research Group for Industrial Applications of Plasmas (IAP group), focusing my studies on the design, characterization and optimization of processes assisted by cold or thermal plasmas for materials' treatment and synthesis, *e.g.* modification of surface wettability and coating deposition. Furthermore, I had the opportunity to study and employ several diagnostic techniques and morphological and chemical analysis methods, which are fundamental tools to characterize the processes under investigation and its effectiveness. During these years I also took part in research activities concerning other aspects of plasma science, such as the development and investigation of an atmospheric pressure inductively coupled plasma source for biomedical applications. Furthermore, most of my activities were carried out in collaboration with numerous industrial and academic partners and in the international framework of the European networking projects MPNS COST Action MP1101 "Biomedical Applications of Atmospheric Pressure Plasma Technology" and CMST COST Action TD1208 "Electrical Discharge with Liquids for Future Application", thus widening and consolidating my expertise.

This dissertation is organized in three main parts, reporting the more significant results achieved on the plasma-assisted treatment and synthesis of materials during my studies. In the first one I will describe an integrated approach for the design and optimization of processes assisted by low-power atmospheric pressure RF thermal plasmas. In the second part, two studies related to the use of CAPs to modify the wettability of synthetic and natural polymeric materials will be discussed. The first one concerns the plasma functionalization of a polyester to increase its hydrophilicity and the development of a prototype plasma system for the treatment of polymeric films; the second one covers the deposition of hydrophobic coatings onto cotton threads in a dynamic configuration. Finally, the last part of this work will be focused on the design and the study of plasma assisted processes (both atmospheric pressure and low pressure) to produce nanocomposite coatings with antibacterial properties. Firstly, the deposition of a nanocomposite coating containing copper nanoparticles performed by means of low pressure plasma sources will be reported. This activity was carried out in the Group of Physics of Thin Films and Surfaces of the Department of Macromolecular Physics (Faculty of Mathematics and Physics, Charles University, Prague), in the framework of widening my knowledge on

processes assisted by low pressure plasmas. Lastly, a study on the co-deposition of nanocomposite coatings using a non-equilibrium atmospheric pressure plasma jet will be described.

Part of the achieved results presented in this work have been reported in the following papers published on international journals:

1. E. Traldi, M. Boselli, M. Gherardi, V. Colombo, *A Simulative and Experimental Approach for the Design and Optimization of Atmospheric Pressure Low Power RF Thermal Plasma Processes*, invited paper for the Special Issue of Plasma Processes and Polymers "Numerical Modelling of Low-Temperature Plasmas for Various Applications — part II: Research papers on numerical modelling for various plasma applications" 2017, 14, 1600167.
2. A. Liguori, E. Traldi, E. Toccaceli, R. Laurita, A. Pollicino, M.L. Focarete, V. Colombo, M. Gherardi, *Co-Deposition of Plasma-Polymerized Polyacrylic Acid and Silver Nanoparticles for the Production of Nanocomposite Coatings Using a Non-Equilibrium Atmospheric Pressure Plasma Jet*, Plasma Processes and Polymers 2016, 13, 623-632.

Results reported in this work were also presented at the following international conferences:

1. *An experimental and computational study of the interaction between the jet of an ICP torch and a cylindrical substrate*, poster presentation at 42nd IEEE International Conference on Plasma Sciences (ICOPS 42), Belek, Antalya, Turkey, 24- 28 May 2015.
2. *An experimental and computational study of the interaction between the jet of an ICP torch and a cylindrical substrate*, poster presentation at 22nd International Symposium on Plasma Chemistry (ISPC 22), Antwerp, Belgium, 5-10 July 2015.
3. *An experimental and computational study of the interaction between the jet of an ICP torch and a cylindrical substrate*, poster presentation at 6th Central European Symposium on Plasma Chemistry (CESPC – 6), Bressanone, Italy, 6-10 September 2015.
4. *Single step process for the deposition of nanocomposite antibacterial coatings using a non-equilibrium atmospheric pressure plasma jet*, poster presentation at Joint meeting of COST Actions CMST TD1208 and MPNS MP1101, Bertinoro, Italy, 13-16 September 2015.
5. *Plasma treatment of materials and for materials synthesis*, oral presentation at 2nd International Workshop on Applied Science & Entrepreneurship, Ghent, Belgium, 26-27 November 2015.
6. *Atmospheric pressure non-equilibrium plasmas for material treatment: surface modification and thin film deposition*, oral presentation at MRS Spring Meeting & Exhibit, Phoenix, USA, 28 March-1 April 2016.

7. *Atmospheric pressure non-equilibrium plasmas for material treatment and nanofabrication*, oral presentation at EMN Meeting on Biomaterials 2016, Phuket, Thailand, 4-7 April 2016.
8. *Atmospheric pressure non-equilibrium plasma jet for acrylic acid plasma-polymerization and co-deposition of antibacterial nanocomposite coatings*, poster presentation at Gordon Research Conference "Plasma Processing Science", Andover (NH), USA, 24-29 July 2016.
9. *New research tools for the field of cold atmospheric plasma applications*, oral presentation at the National Congress of the Italian Society of Biomaterials (SIB 2017), Milano, Italy, 24-26 May 2017.
10. *Deposition of polymeric films and co-deposition of nanocomposite coatings by means of a cold atmospheric pressure plasma jet*, oral presentation at 17th international Conference on Plasma Physics and Applications (CPPA2017), Magurele-Bucharest, Romania, 15-20 June 2017.
11. *Cold atmospheric pressure plasma for the deposition of polymeric films and the codeposition of nanocomposite coatings*, oral presentation at 23rd International Symposium on Plasma Chemistry (ISPC 23), Montreal, 30 July-4 August 2017.
12. *Co-deposition of antibacterial nanocomposite coatings using a non-equilibrium atmospheric pressure plasma jet*, poster presentation at 8th International Workshop on Polymer Metal Nanocomposites (Nanoworkshop 2017), Prague, Czech Republic, 12-15 September 2017.

During my Ph.D. I had also the opportunity to work on the design, development and optimization of a RF thermal plasma source for the treatment of infected wounds, a topic that belongs to the growing field of Plasma Medicine. The results achieved in this activity are not reported in this dissertation, since it is focused on the design and optimization of plasma assisted processes for materials' treatment and synthesis. However, those results were presented in the following international conferences:

1. *Treatment of infected ex-vivo skin tissue with a low power atmospheric inductively coupled plasma source optimized through design oriented simulations*, poster presentation at Joint meeting of COST Actions CMST TD1208 and MPNS MP1101, Bertinoro, Italia, 13-16 September 2015.
2. *Atmospheric non-equilibrium plasma sources and processes with a focus on plasma medicine & antibacterial applications*, oral presentation at 68th Annual Gaseous Electronics Conference (GEC-68)/9th Annual International Conference on Reactive Plasma (ICRP-9)/33rd Symposium on Plasma Processing (SPP-33), Honolulu, USA, 12-16 October 2015.
3. *Treatment of infected ex-vivo human skin tissue with a low power atmospheric inductively coupled plasma source optimized through design oriented simulations*, poster presentation

at 6th International Conference on Plasma Medicine (ICPM 6), Bratislava, Slovacchia, 4-9 September 2016.

In addition, I have been co-supervisor for the following MA and BA theses:

1. M. Fiorini, *Progettazione assistita da simulazione numerica e diagnostica FT-IR per la ottimizzazione di una sorgente di plasma ad induzione per applicazioni "plasma medicine",* Alma Mater Studiorum-Università di Bologna.
2. T. Gallingani, *Ottimizzazione di processi assistiti da sorgenti di plasma atmosferico di non equilibrio per la funzionalizzazione di polimeri, la deposizione di coating e la sintesi di nanostrutture*, Alma Mater Studiorum-Università di Bologna.
3. R. Riccioli, *Caratterizzazione e analisi di efficacia di una sorgente industriale di plasma atmosferico per il trattamento automatizzato di materiali termosensibili*, Alma Mater Studiorum-Università di Bologna.
4. G. Vinelli, *Progettazione, realizzazione e caratterizzazione funzionale di sorgenti di plasma atmosferico di non equilibrio per l'idrofobizzazione di fibre tessili*, Alma Mater Studiorum-Università di Bologna.
5. R. Licastro, *Caratterizzazione e ottimizzazione sperimentale di una sorgente plasma ICP modificata per trattamenti Plasma Medicine*, Alma Mater Studiorum-Università di Bologna.
6. M. Ulivi, *Ottimizzazione funzionale di una sorgente plasma jet di non equilibrio per processi di polimerizzazione e sintesi di nanoparticelle in liquido*, Alma Mater Studiorum-Università di Bologna.

1. Integrated Approach for the Design and Characterization of Processes Assisted by Low-Power RF Thermal Plasma Sources Based on the Comparison of Simulative and Experimental Data

1.1. Introduction

Since their first appearance in the field of plasma science in 1961 [1], atmospheric pressure Radio-Frequency (RF) thermal plasma torches have become the technologic core of several industrial processes, thanks to their intrinsic characteristics, such as high enthalpy density, purity, scalability and flexibility in the selection of geometries and operating parameters [2], Most of these processes, such as Chemical Vapour Deposition (CVD), synthesis of nanoparticles, powders spheroidization, thermal spraying and waste destruction [3–6], make use of medium-high power RF torches (from tens of kW up to a few MW), however several other ones are supported by low-power torches (few kW), especially when high precision and purity are required. The low-power RF technology includes the well-known analytical techniques Inductively Coupled Plasma-Mass Spectrometry (ICP-MS) and Inductively Coupled Plasma-Optical Emission Spectroscopy (ICP-OES) [7,8], the pure silica overcladding of preforms for the production of optical fibers (for which torches are usually operated at higher power in industrial systems) [9–14], the accurate measurement of the physical properties of materials at high temperature [15,16], the precision figuring of optical surfaces in Reactive Atom Plasma (RAP) process [17–21], and the application of RF plasmas for biomedical applications [22,23].

To obtain the best performances in these processes it is fundamental to carry out properly the design and optimization of the plasma sources and the systems in which they are integrated, considering the effects of varying the operating and geometric parameters on the investigated

process, which is usually very complex due to the flexibility aforementioned. These parameters include: the generator frequency and power; the estimated coupled power to the plasma (since its exact calculation requires experimental tests, such as calorimetric measurements); the geometry of the coil; the flow rate and the composition of the different gases employed (plasma, sheath and carrier gas flows); the typology and position of the injection probe; other parameters specific to the process in which the RF torch has to be employed such as the geometry of the reaction chamber for the synthesis of nanoparticles. Simulation modelling proved to be a valuable tool for this purpose especially during the early stages of process design, as it consents to study these effects without the need for expensive prototypes, which are characteristic of "*try & fail"* approaches. Several research groups have developed reliable numerical models to study low-power atmospheric pressure RF thermal plasmas in the last years: the first models developed by Boulos, Proulx and Mostaghimi [24–33], the works of Colombo *et al.* on RF torches for industrial applications [10,34–41], the studies of the research groups of Montaser [42–46] and Bogaerts [47–54] on analytical RF torches, and several others [20,21,55–66]. However, simulative data are presented jointly with experimental ones only in few of these works, allowing through an integrated approach to characterize in depth the subjects studied therein and validate the numerical models [10,48,52,63,65,66].

Nevertheless, several diagnostic techniques can be employed to study RF discharges and the behaviour of their effluents in order to obtain useful information on the processes in which they are implemented: High Speed Imaging (HSI), CCD camera imaging and Schlieren Imaging (SI) can be used to characterize the shape and the turbulence phenomena related to the discharge and the ignition transient of the torch [65–68], OES [10,48,52,69] and Fourier Transform-Infrared (FTIR) spectroscopy [23,70] can be employed to study the chemical species composition in the plasma region and in the effluents of the torch, respectively, and UV irradiance can be measured for biomedical applications [23].

Considering the amount of relevant information that can be obtained from the integrated use of numerical models and experimental diagnostic techniques, the industrial systems in which RF thermal plasmas are employed would clearly benefit from adopting such approach during their design, investigation and optimization.

During my Ph.D. studies several activities on RF thermal plasmas have been carried out adopting this integrated approach. As example of its use, a case study of a RF torch operating at different power levels (maximum 1 kW) and flow rates, is reported in this chapter, investigating the behaviour of the effluent of the plasma discharge with and without a cylindrical metallic substrate placed downstream of the torch outlet, adopted as representative

of industrial processes such as the pure silica overcladding phase in the production of optical fibers [9–14]. Regarding the numerical study, the plasma generation region inside the torch is simulated in a 2-D axisymmetric environment in order to obtain the temperature and velocity profiles at the outlet of the torch. These profiles are used as a hot gas boundary condition for 3-D simulations of a plasma jet produced by the RF torch either in a free flow regime or impinging on a cylindrical stainless steel (SS) substrate. HSI and SI of the flow region and temperature measurement on the surface of the substrate by using an IR sensor are performed to experimentally characterize the process and make a comparison of the obtained data with the numerical outputs. These results have been reported also in a scientific work published on *Plasma Processes and Polymers* [71].

1.2. Process Modelling

1.2.1. 2-D Simulations

1.2.1.1. 2-D Governing Equations

The plasma discharge generated in the RF torch is modelled within a 2D axisymmetric geometry using the commercial software ANSYS FLUENT© [72] to solve fluid equations integrated by user-defined functions that implement the electromagnetic field and the radiative losses terms. The following assumptions, also adopted in previous works of the author's research group [35–37,39], are employed:

- plasma is in local thermodynamic equilibrium (LTE) [3];
- the flow is steady and laminar;
- plasma is considered optically thin;
- the viscous dissipation term in the energy equation is neglected;
- displacement currents are neglected.

The equations employed for the transport of mass, momentum, and energy are written as follows:

$$\nabla \cdot \rho \boldsymbol{u} = 0 \tag{1.1}$$

$$\nabla \cdot (\rho \boldsymbol{u}\boldsymbol{u}) = -\nabla p + \nabla \cdot \boldsymbol{\tau} + \rho \boldsymbol{g} + \frac{1}{2} Re(\boldsymbol{J} \times \boldsymbol{B}^*) \tag{1.2}$$

$$\nabla \cdot (\rho \boldsymbol{u} h) = \nabla \cdot \left(\frac{k}{c_p} \nabla h\right) + \frac{1}{2} Re(\boldsymbol{J} \cdot \boldsymbol{E}^*) - R \quad (1.3)$$

where ρ is the plasma gas density, $\boldsymbol{u}$ is the gas velocity, p is the gas pressure, $\boldsymbol{\tau}$ is the viscous stress tensor, $\boldsymbol{g}$ is the gravitational acceleration, $\boldsymbol{J}$ is the complex phasor for the current density induced in the plasma, $\boldsymbol{B}$ and $\boldsymbol{E}$ are the complex phasors for the magnetic and electric field respectively (the superscript '*****' indicates the complex conjugate), h is the enthalpy, k is the thermal conductivity, c_p is the specific heat at constant pressure and R is the volumetric radiative loss. The electromagnetic field generated in the plasma region is expressed by Maxwell's equations written in their vector potential formulation [73]:

$$\nabla^2 \boldsymbol{A} - i\,\mu_0 \sigma \omega \boldsymbol{A} + \mu_0 \boldsymbol{J_{coil}} = 0 \quad (1.4)$$

where $\boldsymbol{A}$ stands for the vector potential complex phasor, $\boldsymbol{J_{coil}}$ is the complex phasor for the current flowing in the coil, μ_0 is the magnetic permeability of the free space ($4\pi \cdot 10^{-7}$ H m^{-1}), σ is the plasma electrical conductivity and $\omega = 2\pi f$, f being the frequency of the electromagnetic field. The electric field $\boldsymbol{E}$ and the magnetic field $\boldsymbol{B}$ which appear in Equation 1.2 and 1.3 can be expressed by means of the vector potential $\boldsymbol{A}$ in accordance with the following expressions:

$$\boldsymbol{E} = -i\omega \boldsymbol{A} \quad (1.5)$$

$$\boldsymbol{B} = \nabla \times \boldsymbol{A} \quad (1.6)$$

The current density induced in the plasma is obtained from the simplified Ohm's law:

$$\boldsymbol{J} = \sigma \boldsymbol{E} \quad (1.7)$$

To calculate the thermodynamic and transport properties of the gas mixture and the corresponding radiative losses, the contributions from both argon and air are taken into account, using data from Murphy *et al.* [74] and Cressault *et al.* [75,76]. Linear interpolation of the Net Emission Coefficients (NEC) based on the molar fractions of Ar and air is employed to obtain the volumetric radiative loss R, as suggested by Cressault *et al.* [77]. The NEC approximation employs the Planck function and different mechanisms of radiation losses (*e.g.* the transitions between energy states of molecules and atoms), also considering reabsorption phenomena that

may occur in the plasma. Further details on this model can be found in the works of Lowke *et al.* [78,79] and Gleizes *et al.* [76,77,80–83].

1.2.1.2. 2-D Axisymmetric Computational Domain and Boundary Conditions

The 2-D axisymmetric computational domain includes the RF torch, consisting of two concentric quartz tubes and a three-turns coil, and a volume of space surrounding it. These elements are reported in Figure 1.1 with their dimensions. Pure Ar is supplied through two different inlet regions located in the head of the torch: central gas from the central quartz tube and sheath gas from the gap between the two tubes, pointed by the blue and the green arrows respectively in Figure 1.1. Central gas is used to sustain and stabilize the plasma generation, while sheath gas is necessary to confine the plasma discharge and prevent the damage of the confinement tube caused by overheating. The velocity direction of central and sheath gas flows is assumed constant as the mass flow rate changes: the axial and the tangential components which compose the unit vector defining the direction of the velocity of the supplied gas flows are 0.26 and 0.97, respectively. A sheath gas characterized by a swirl component is sufficient to protect the confinement tube of the torch for low power systems (below 5 kW) [10], however RF torches which operate with higher plate power usually require to adopt a water cooled confinement tube and an axial injection for the sheath gas. Simulations were performed under four different operating conditions, as reported in Table 1.1. Assuming an efficiency of 80% for the overall system consisting of the solid state generator and the matching network, coupled power to the plasma was assumed to be 280 W and 400 W, respectively, for 350 W and 500 W generator plate power. The RF current frequency is set to 13.56 MHz. The coil current was continuously adjusted by the numerical solver to match the volume integral of the joule power in the numerical domain with the imposed coupled power. This is accomplished by adjusting dynamically the coil current. No-slip boundary condition is imposed on every wall surface. At the outlet, backflow temperature is set to 300 K with a gauge pressure of 0 Pa to represent the atmospheric air surrounding the torch. The numerical domain is composed by approximately 70000 quadrilateral cells.

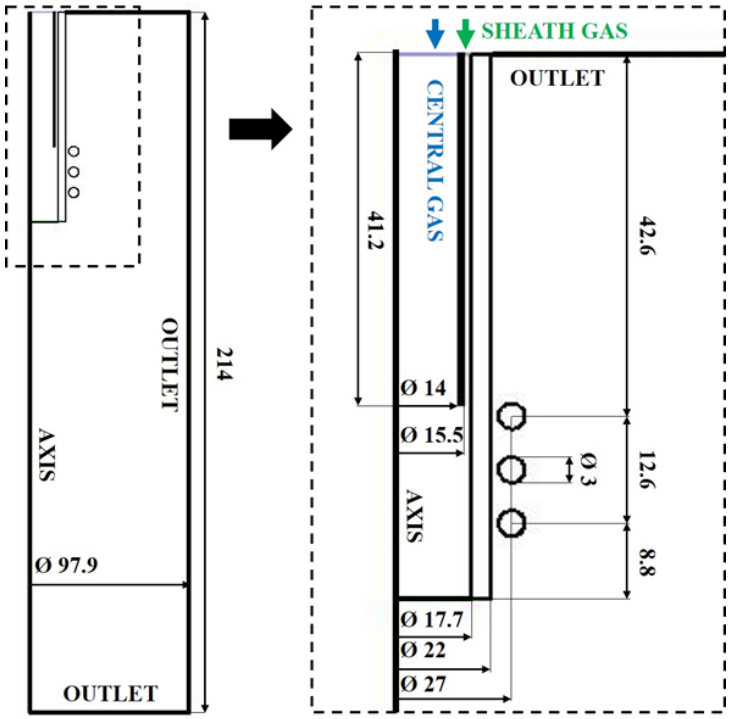

Figure 1.1 Schematic of the overall 2-D axisymmetric computational domain (left), and of the RF torch (right). All dimensions are reported in mm [71].

Table 1.1 Operating conditions imposed in 2D axisymmetric simulations [71].

Operating condition	**Plate power P [W]**	**Central gas flow rate Q_{ce} [slpm]**	**Sheath gas flow rate Q_{sh} [slpm]**
A	350	0.9	8
B	350	0.9	12
C	500	2	8
D	500	2	14

1.2.2. 3-D Simulations

1.2.2.1. 3-D Governing Equations

The jet produced by the hot gaseous effluents exiting the RF torch is simulated in a 3-D computational domain either in a free flow regime or impinging on a cylindrical SS substrate using the software ANSYS FLUENT©. The equations employed for transport of momentum

and energy (Equation 1.2 and 1.3) are modified with respect to those implemented in the 2-D axisymmetric model to reduce the computational effort, which would be much higher in a 3-D domain. Indeed, the following different assumptions were adopted:

- the electromagnetic effects are neglected, thus considering the effluent of the discharge as a high temperature gas not electrically conductive;
- the flow is steady and turbulent effects are implemented using the Reynolds Stress Model (RSM) [72];
- Discrete Ordinates (DO) radiation model is implemented in order to take into account the radiative heat exchange to the substrate and the torch outlet [72];
- the viscous dissipation term in the energy equation is neglected.

The first assumption is based on 2-D results as it was observed that the joule effect due by the electric current is negligible in the downstream region. The terms in Equation 1.2 and 1.3 related to the electromagnetic field and $\boldsymbol{J}$ are then neglected, while the term related to the volumetric radiative losses is still considered. According to the RSM model the equations for the transport of the Reynolds stresses are simultaneously solved:

$$\nabla \cdot \left(\rho \boldsymbol{u} \overline{u_i' u_j'}\right) = D_{T,ij} + D_{L,ij} + P_{ij} + G_{ij} + \phi_{ij} + \varepsilon_{ij} \qquad (1.8)$$

where $\rho\overline{u_i' u_j'}$ are the Reynolds stresses, $D_{T,ij}$ represents the turbulent diffusion, $D_{L,ij}$ represents the molecular diffusion, P_{ij} is the stress production, G_{ij} is the buoyancy production term, ϕ_{ij} is the pressure strain term and ε_{ij} is the dissipation tensor [72]. Linear Pressure-Strain model is implemented to evaluate the pressure strain term and Scalable Wall Functions were adopted to evaluate near-wall effects. The radiative transfer equation is obtained taking in account the Gray bodies assumption in DO radiation model:

$$\nabla \cdot (I(\boldsymbol{r}, \boldsymbol{s})\boldsymbol{s}) + (a + \sigma_S) I(\boldsymbol{r}, \boldsymbol{s}) = an^2 \frac{\sigma T^4}{\pi} + \frac{\sigma_S}{4\pi} \int_0^{4\pi} I(\boldsymbol{r}, \boldsymbol{s}') \Phi(\boldsymbol{r}, \boldsymbol{s}') d\Omega' \qquad (1.9)$$

where $\boldsymbol{r}$ is the position vector, $\boldsymbol{s}$ the direction vector, $\boldsymbol{s'}$ the scattering direction vector, s the path length, a the absorption coefficient, n the refractive index, σ_S the scattering coefficient, σ the Stefan-Boltzmann constant, I the radiation intensity, T the local temperature, Φ the phase function and Ω' the solid angle [72].

Considering the previous assumptions, the equation for the transport of energy is modified by the turbulence and the DO radiation model terms as follows:

$$\nabla \cdot (\rho \boldsymbol{u} h) = \nabla \cdot \left(\frac{k_{eff}}{c_p} \nabla h \right) - R + R_{DO} \qquad (1.10)$$

where k_{eff} is the effective conductivity (sum of k and the turbulent thermal conductivity) and R_{DO} is the source term related to the DO radiation model.

1.2.2.2. 3-D Computational Domain and Boundary Conditions

The 3-D computational domain consists of a cylindrical volume inside which a solid cylindrical substrate of SS located 30 mm downstream the outlet of the RF torch is impinged by the gaseous hot temperature effluents produced by the plasma discharge, as represented in Figure 1.2. Velocity and temperature profiles obtained by means of 2-D axisymmetric simulations for the operating conditions reported in Table 1.1 at the outlet of the torch are used as boundary conditions for pure Ar inlet in the 3-D simulations of the RF torch downstream region. Two operating conditions, A and B, are simulated in a free flow regime, while the remaining two, C and D, are simulated including the solid cylindrical substrate in the computational domain, as shown in Figure 1.2.

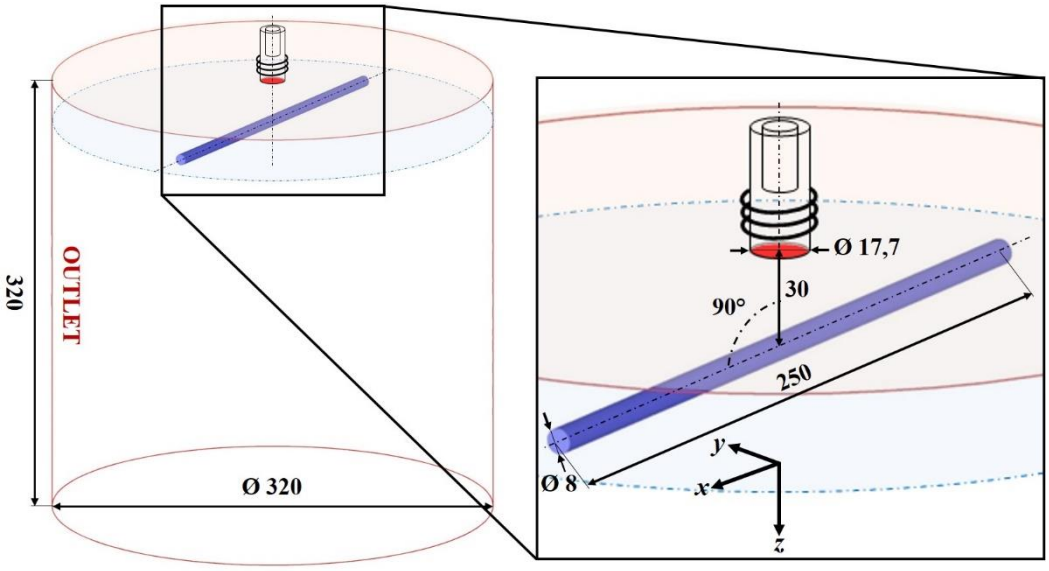

Figure 1.2. Schematic of the 3-D computational domain (left), of the velocity inlet which stands for the outlet of the torch (the dark red circle on a light red plane) and of the cylindrical substrate located downstream the RF torch (on a light blue plane). The axes of the Cartesian coordinate system are also shown (right). All dimensions are reported in mm [71].

At the outlet, backflow temperature is set to 300 K and gauge pressure is set to 0 Pa, similarly to the 2-D axisymmetric simulations. The 3-D domain is meshed using approximately 252000 polyhedral cells for the simulations in free flow regime (conditions A and B). In the simulations with the jet impinging on the substrate (conditions C and D), the volume of the substrate is composed by about 108000 cells and the surrounding region by about 567000 cells. The turbulent intensity and turbulent viscosity ratio, which are the boundary condition concerning the turbulence, were set to 5 % and 10, respectively, at the velocity inlet and for the outlet backflow. No-slip boundary condition is imposed on every wall surface of the substrate. To correctly discretize the propagation of thermal radiation in the DO radiation model 32 directions are used, with a 2×2 pixel resolution for the control angles. Internal emissivity values are set for the inlet, the walls of the substrate and the outlet (respectively 0.01, 0.07 and 0.95). a = 0 m^{-1}, σ_S = 0 m^{-1} and n = 1 were set for both Ar and air. Values for density (8030 kg m^{-3}) and specific heat at constant pressure (502.5 J kg^{-1} K^{-1}) of SS are assumed temperature-independent, while the following equation, obtained by linear interpolation of data at different temperatures [84] was used to evaluate its thermal conductivity (k_{SS}, W m^{-1} K^{-1}):

$$k_{SS} = 0.0133T + 11.256 \quad (1.11)$$

1.3. Experimental Setup and Diagnostic Techniques Adopted

1.3.1. Plasma Source and SS Cylindrical Substrate

The plasma source used to perform the experimental studies consists of two coaxial quartz tubes having inner diameters of 17.7 and 14 mm, respectively, as shown also in the modelled geometry of Figure 1.1. The inner tube prevents the mixing of central and sheath gas before reaching the coil region. The external confinement tube is surrounded by a three-turn air-cooled copper coil fed by a 13.56 MHz RF solid state power generator with a maximum plate power of 1 kW (Stolberg HF-Technick AG) and the related matching network (agilo 1315a MC10, COMET Group). Tests were performed at atmospheric pressure using Ar 5.0 for both central and sheath gas, with velocity components as reported in 1.2.1.2. An 8 mm diameter rod made of SS AISI 304, whose axis intersects perpendicularly the axis of the RF torch, was placed 30 mm below the outlet of the plasma source to study the impingement of the jet produced by the

torch and a substrate. The operating conditions employed during the tests and the diagnostics techniques adopted to characterize each of them are reported in Table 1.2.

Table 1.2. Operating conditions experimentally investigated and corresponding diagnostics adopted [71].

Operating condition	Diagnostics adopted
A	HSI, SI
B	HSI, SI
C	SI
D	SI, T measurement on the substrate

1.3.2. Visualization Techniques: High Speed Imaging and Schlieren Imaging

The discharge behavior and the characteristics of the hot effluents downstream the exit of the torch have been investigated using a high speed camera (Memrecam GX3, NAC Image Technology) both for HSI and for SI, with a setup similar to the ones presented in previous works [67,85,86]. During acquisitions the high speed camera was operated at 500 frames s^{-1} with a continuously open shutter. SI was performed using a Z-type optical setup and the high speed camera was operated at 2000 frames s^{-1} and shutter speed was set to 1/100000 s for the acquisitions without the substrate, while it was operated at 3000 frames s^{-1} and shutter speed was set to 1/200000 s for the acquisitions with the substrate placed downstream the torch outlet. The imaging setup for SI shown in Figure 1.3 consists of a 450 W ozone free xenon lamp (Newport-Oriel 66355 Simplicity Arc Source), a slit and a filter, two parabolic mirrors with a focal length of 1 m, two planar mirrors and a knife edge positioned vertically. The filter is employed to reduce the intensity of the light beam in order to adapt it to the luminosity of the plasma and to increase the sharpness of the schlieren shapes, or streaks, in each frame. Two different experimental configurations have been studied using SI: for the first one the axis of the substrate is set coaxial with the collimated beam of the light source (as represented in Figure 1.3), for the second one the axis of the substrate is set perpendicular to both the collimated beam and the torch axis.

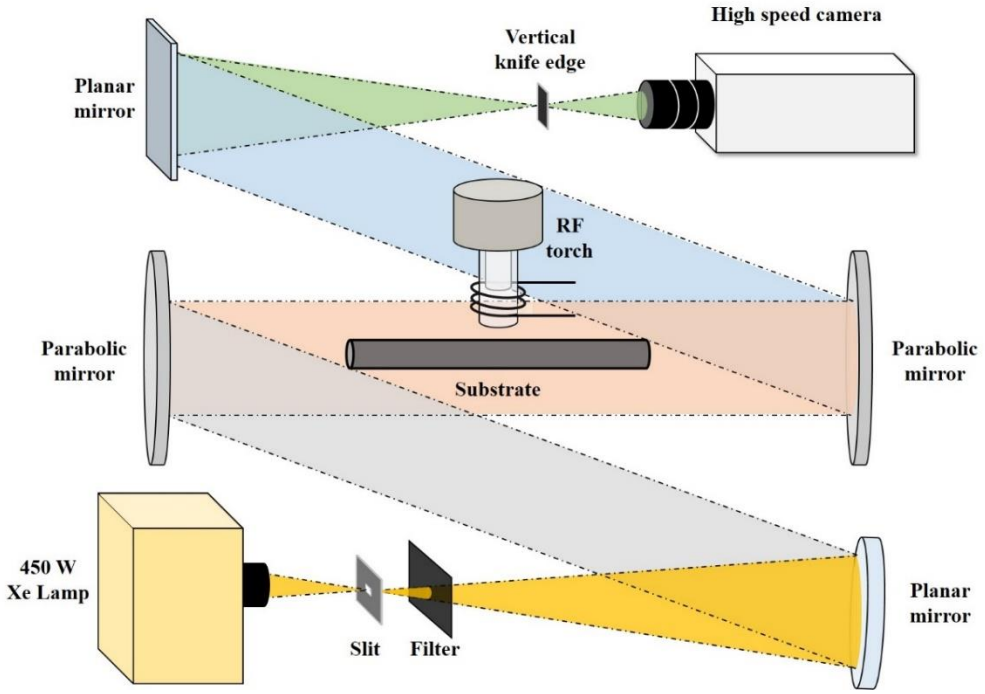

Figure 1.3. Setup adopted to perform SI. The cylindrical substrate is placed downstream the torch outlet [71].

1.3.3. Contactless Temperature Measurement on the Surface of the Substrate

Measurement of the temperature on the surface of the substrate has been performed using an IR sensor (CTLaser LT CF1, Optris GmbH) in order to avoid any perturbation of the flow during the measurement. The IR sensor is designed to give the mean temperature in a circular spot as small as 1 mm of diameter and its measurement accuracy is inversely dependent from the spot size. Consequently, the temperature measurement has been performed with the IR sensor placed at a distance of 7 cm, thus minimizing the sensor spot size on the surface of the substrate, as shown in Figure 1.4. The IR sensor was pointed on the surface of the substrate at the intersection between two planes: one perpendicular to the axis of the torch and including the axis of the substrate and another one perpendicular to the axis of the substrate and including the axis of the torch. Before operating it, the IR sensor has been calibrated by measuring the emissivity of the SS substrate for some values of temperature in a controlled range, using a hot plate in order to heat up the substrate and then a thermocouple to measure the actual temperature on its surface. Temperature measurement on the surface of the substrate was not performed for condition C, as the temperature reached by the substrate (higher than 560 K) induced a shift in the color of SS [87], with a corresponding change in emissivity and loss of calibration capacity of the IR sensor.

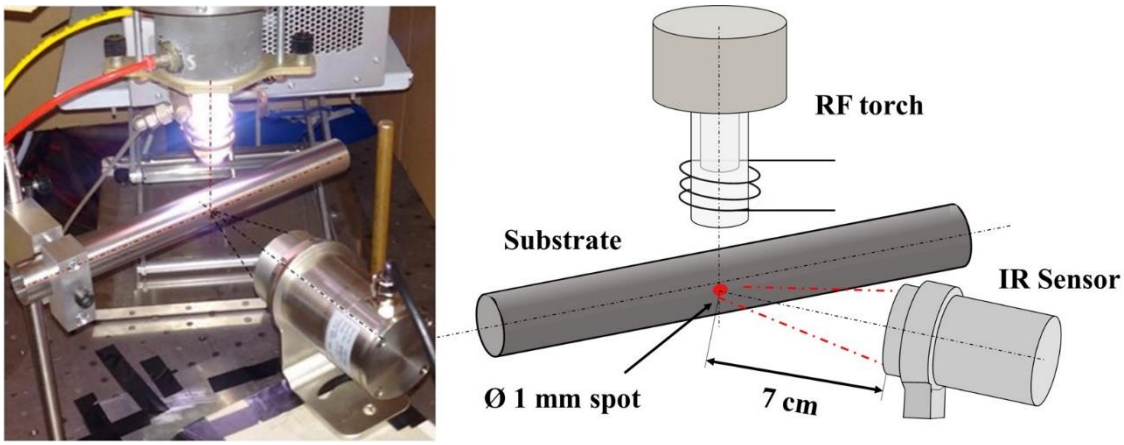

Figure 1.4. Picture (left) and schematic (right) showing the setup for IR measurement of the temperature of the substrate impinged by the RF torch gaseous effluent [71].

1.4. Results and Discussion

1.4.1. 2-D Simulations Results of the RF Torch Discharge

Results obtained from the solution of the governing equations used for the 2-D simulations under the boundary conditions of Table 1.1 are presented in this section. The discharge inside the RF torch was studied (as well as in the downstream region) for the four operating conditions in order to obtain the velocity and temperature profiles at the torch outlet. The calculated temperature fields are shown in Figure 1.5, Figure 1.6, Figure 1.7 and Figure 1.8, respectively, for conditions A, B, C and D.

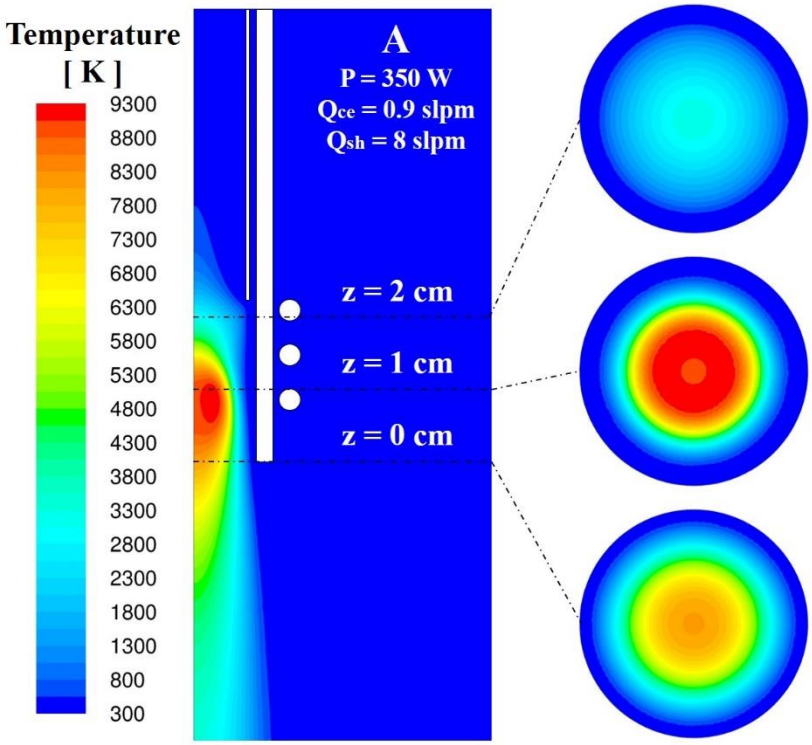

Figure 1.5. 2-D contours of temperature inside the RF torch and in the downstream region (left) and on three horizontal planes located at z = 0, 1, 2 cm upstream the outlet of the torch, respectively, from bottom to top (right) for operating condition A [71].

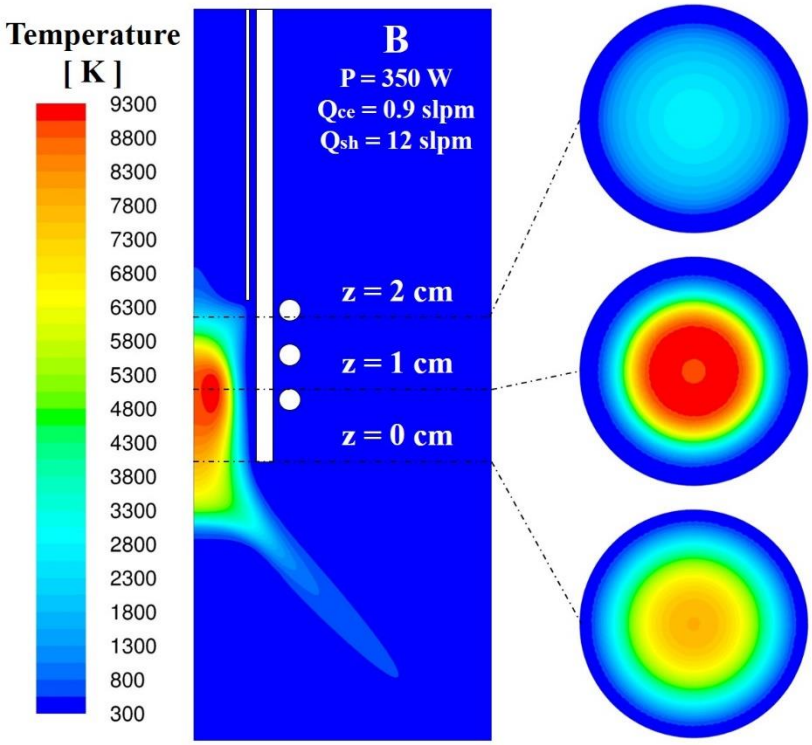

Figure 1.6. 2-D contours of temperature inside the RF torch and in the downstream region (left) and on three horizontal planes located at z = 0, 1, 2 cm upstream the outlet of the torch, respectively, from bottom to top (right) for operating condition B [71].

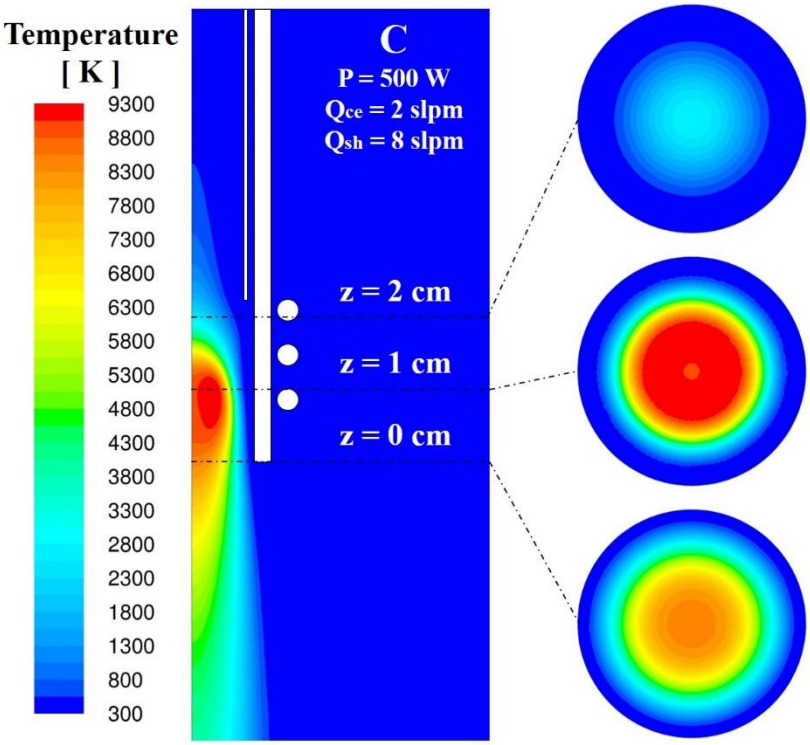

Figure 1.7. 2-D contours of temperature inside the RF torch and in the downstream region (left) and on three horizontal planes located at z = 0, 1, 2 cm upstream the outlet of the torch, respectively, from bottom to top (right) for operating condition C [71].

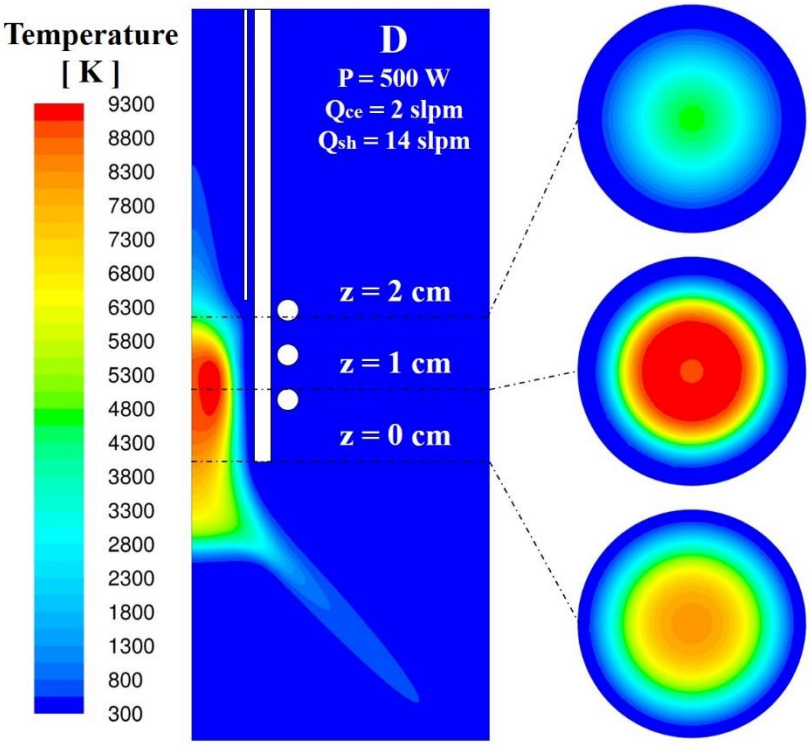

Figure 1.8. 2-D contours of temperature inside the RF torch and in the downstream region (left) and on three horizontal planes located at z = 0, 1, 2 cm upstream the outlet of the torch, respectively, from bottom to top (right) for operating condition D [71].

It can be observed that for higher sheath gas flow rates (operating conditions B and D) the outflow of the RF torch spreads radially and drifts apart from a jet-like behavior, compared to condition A and C. For condition B and D the zone that reaches the highest temperatures is located at z = 1 cm upstream the outlet of the torch, while for condition A and C the same zone is displaced downstream, leading to higher temperatures at the outlet of the torch. In Figure 1.9 and Figure 1.10 are reported plotted vector velocity fields for each operating condition. For conditions A and C the velocity vectors of the effluent of the discharge are directed downstream, with the surrounding air following the direction of the plasma plume; while for condition B and D they spreads radially from the torch and a counter flow of air moving towards it can be observed.

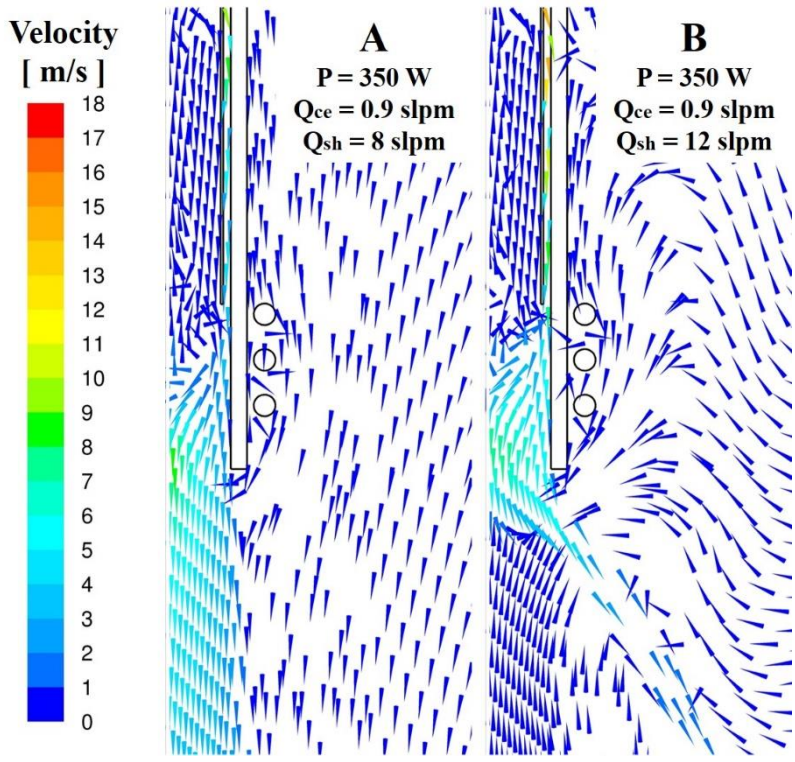

Figure 1.9. Vector velocity fields inside the RF torch and in the downstream region corresponding to the operating conditions A and B [71].

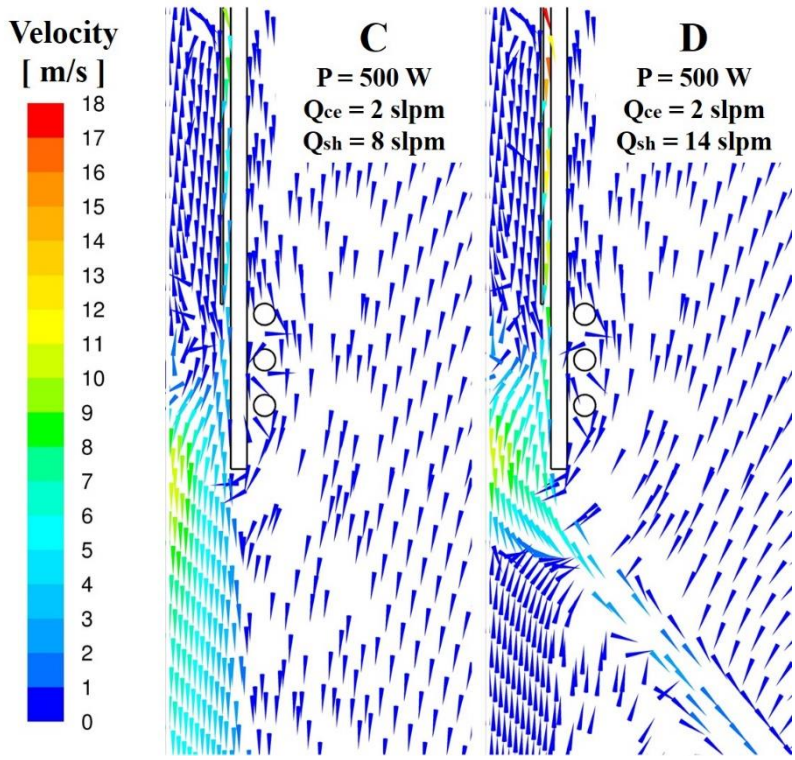

Figure 1.10. Vector velocity fields inside the RF torch and in the downstream region corresponding to the operating conditions C and D [71].

The shape of the plasma plume can be explained by the gauge pressure fields, shown in Figure 1.11 and Figure 1.12. In fact, it can be observed that for conditions B and D a zone of negative gauge pressure is located at the outlet of the torch and the pressure inside the torch is near to atmospheric except close to the confinement tube; for conditions A and C, the pressure inside the torch is higher than atmospheric and a zone of slightly negative gauge pressure is located downstream the RF torch. We can assume that using high sheath gas flow rates induces negative gauge pressure at the outlet of the torch, generating a reverse flow of air moving towards its axis and inducing a "splitting" of the plasma plume. The same phenomenon doesn't occur for low sheath gas flow rates, as it is prevented by the positive pressure inside torch due to the values of the central gas flow rate. For condition B and D, the counter flow of air induces an air entrainment in the jet leading to a drastic cooling of the gas effluents downstream the outlet of the torch. The causes for this behavior can be confirmed when analyzing the distribution of the mole fraction of Ar in the downstream region of the RF torch, as reported in Figure 1.13 and Figure 1.14.

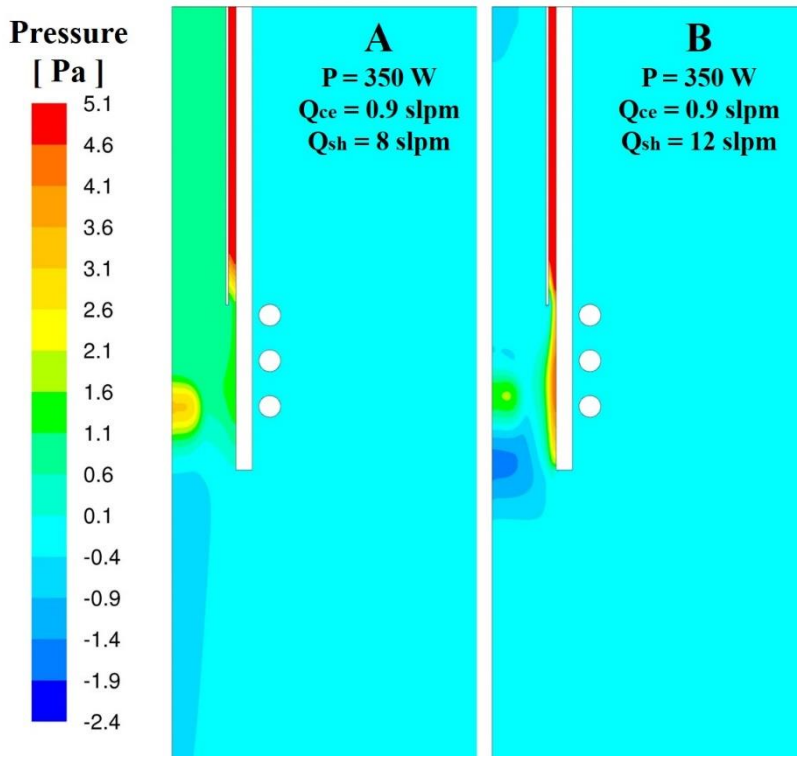

Figure 1.11. 2-D contours of gauge pressure inside the RF torch and in the downstream region corresponding to operating conditions A and B [71].

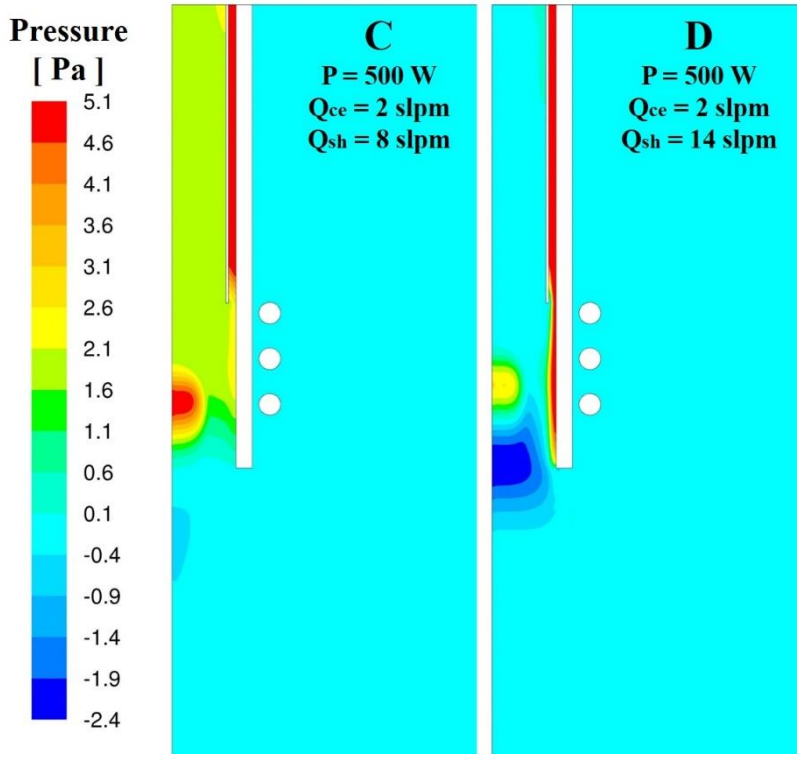

Figure 1.12. 2-D contours of gauge pressure inside the RF torch and in the downstream region corresponding to operating conditions C and D [71].

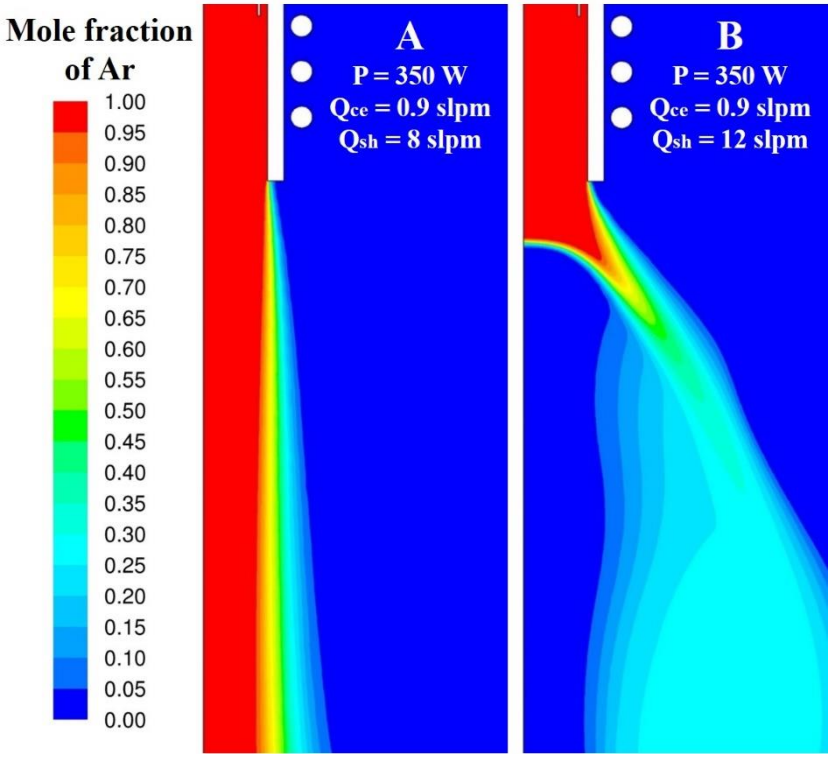

Figure 1.13. Mole fraction of Ar distributions corresponding to the operating conditions A and B [71].

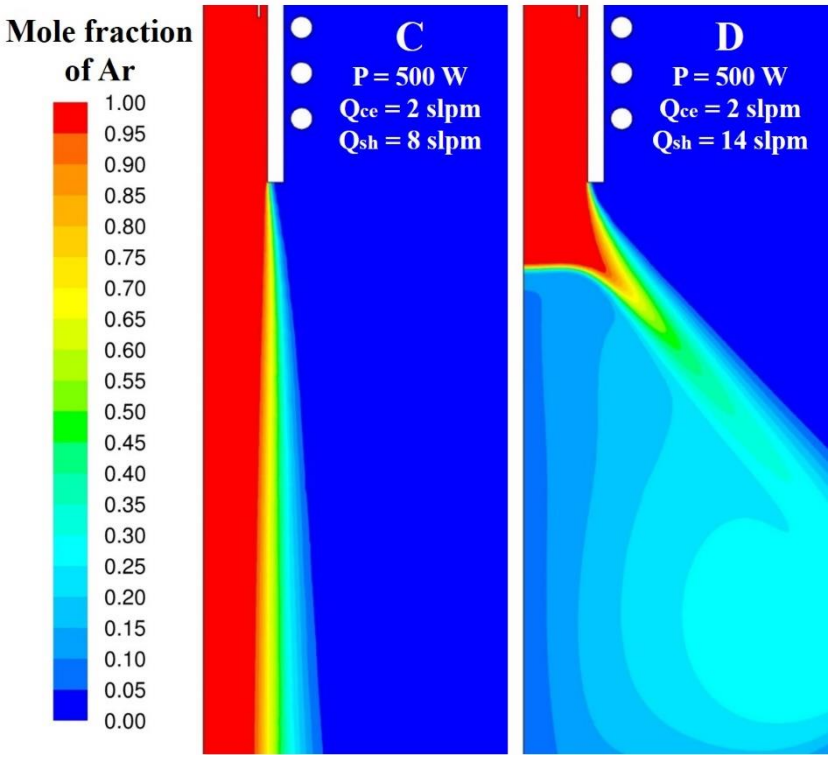

Figure 1.14. Mole fraction of Ar distributions corresponding to the operating conditions C and D [71].

Profiles of the velocity components and the temperature at the outlet of the quartz tube for the four operating conditions are shown in Figure 1.15. Tangential velocity is considerably more intense for conditions B and D with respect to conditions A and B, due to the fact that it is strongly related to the sheath gas flow rates. Furthermore, for conditions C and D the maximum values of tangential velocity are located closer to the confinement tube; this can be caused by the interaction of the sheath and central gas flows; the latter having higher rates for these conditions with respect to the other ones (A and B). Radial velocity profiles show that the flow is characterized by a centripetal component for conditions A and C (except near the tube wall) and by a centrifugal component for conditions B and D. This effect is produced by the unbalancing of centripetal Lorentz forces in the plasma jet and centrifugal forces in the sheath gas, the latter prevailing for high sheath gas flow rates. For operating conditions B and D, calculated axial velocities show a more uniform behavior along the radius of the quartz tube than for operating conditions A and C. On the contrary, temperature profiles at the outlet of the RF torch show a similar behavior under the different operating conditions. The different behavior of the effluent of the discharge in the region downstream the torch exit in different operating conditions seems to be related primarily to the interaction between the central and sheath gas flows. It seems that changes in the power coupled to the plasma (in the range 350-500 W) have just a slight effect on the temperature of the discharge.

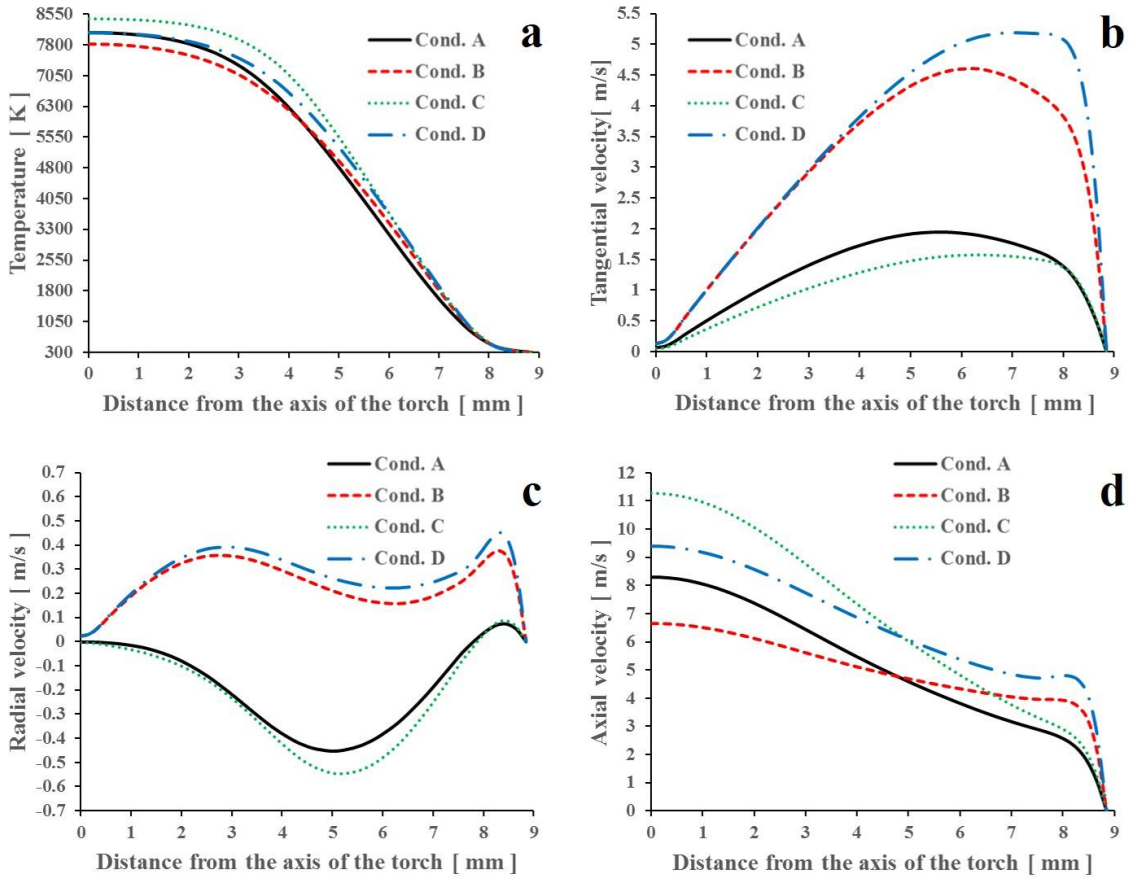

Figure 1.15. Profiles of temperature (a), tangential velocity (b), radial velocity (c) and axial velocity (d) at the outlet of the RF torch for the operating conditions A, B, C and D [71].

1.4.2. Comparison between 3-D Simulations Results and Experimental Results

As previously described, the temperature distribution and the velocity profiles at the outlet of the RF torch as obtained from 2-D simulations were implemented as boundary conditions for 3-D simulations aimed at more effectively studying the behavior of the effluent of the discharge downstream the torch outlet. The numerical results of the 3-D simulations are here presented and compared to the experimental ones acquired from the diagnostics techniques. To help visualizing the results of 3-D simulations, 2-D contours on perpendicular planes *xz* and *yz* (as defined by the Cartesian coordinate system in Figure 1.2) are shown hereafter.

In Figure 1.16 and Figure 1.17, a comparison between the frames obtained using HSI and the 3-D simulative contours of radiative power losses and of temperature has been performed for operating conditions A and B, as they properly represent the two behaviors (jet-like and radially spread) that have been evidenced during the experimental investigation of the behavior of the

low-power RF torch. Comparing Figure 1.16c with Figure 1.16d and Figure 1.17c with Figure 1.17d, both conditions present a symmetric behavior of the effluent of the torch, as velocity and temperature profiles coming from axisymmetric 2D simulations are imposed as boundary condition and there is no presence of a substrate which can affect the flow. A less idealized 3D simulation of an RF ICP discharge could present a less symmetric behavior; however, it is reported that at 13.56 MHz of coil current frequency the discharge in the torch is almost axisymmetric [41].

As shown in Figure 1.16, the simulated contours of radiative power losses and temperature for condition A show a good agreement with the shape of the discharge. In fact, the brighter zone of the plasma plume can be easily identified in both the simulated contours (for radiative losses higher than $1 \cdot 10^4$ W m^{-3} and for temperatures higher than 4000 K). As shown in Figure 1.17c, the plasma plume shape is qualitatively represented by the temperature distribution, comparing the bright region of the HSI frame with the 1100 K temperature contour obtained from simulation. While HSI frame (Figure 1.17a) shows a region midst the plasma plume where light is not emitted (or at least with an intensity which is too low to be detected by the camera), no discontinuities are present in the temperature contours. Therefore, the temperature distribution can't properly represent the light emitted from the effluent of the discharge for operating condition B. The radiative losses contours (Figure 1.17b) are more suited to represent this behavior of the plasma plume, since there is an evident discontinuity for the values in the range $8 \cdot 10^4$ - $2 \cdot 10^5$ W m^{-3}. However, also radiative losses contours can't properly represent the characteristics and geometry of the effluent of the discharge, as the zone of light emission is shorter along the axial direction of the plasma plume and the curved shape of the plume can't be discerned, while it is clearly visible in HSI frame and in the temperature distribution (Figure 1.17a and Figure 1.17c). This disagreement could be related to the air entrainment in the jet, which occurs due to the high sheath gas flow rate in condition B, as presented in Figure 1.13. This air entrainment is shown by the color change in the plasma plume from the region directly downstream the outlet of the torch and the farthest one. In fact, the light emitted from the plasma plume turns from white to orange, differently to the jet seen in Figure 1.16a for condition A; phenomenon that can be related to the emission spectra from an air plasma.

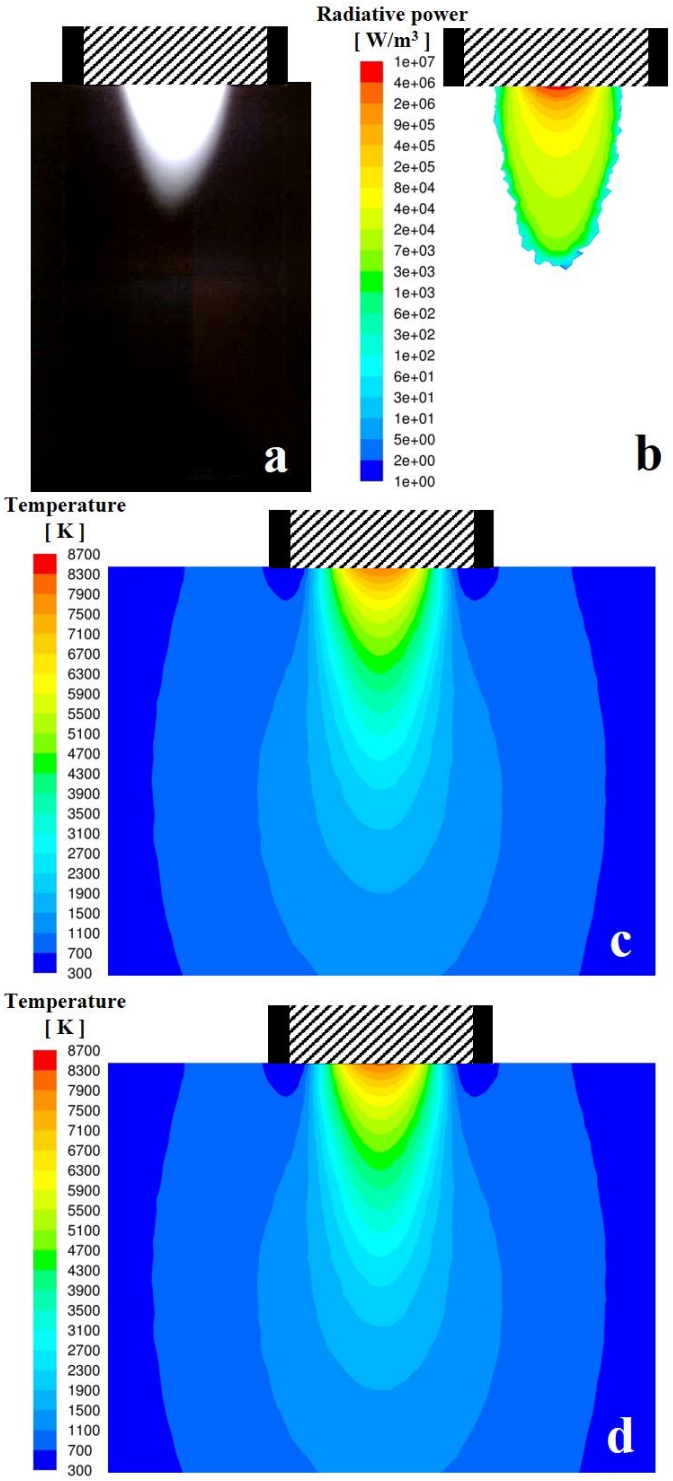

Figure 1.16. Comparison between experimental and numerical results of the 3-D simulation for operating condition A: side view of the plasma plume obtained from HSI (a), contours of simulated radiative power losses (b) and simulated temperature distributions on plane *xz* (c) and *yz* (d). The non-striped pattern in the torch represents the confinement tube [71].

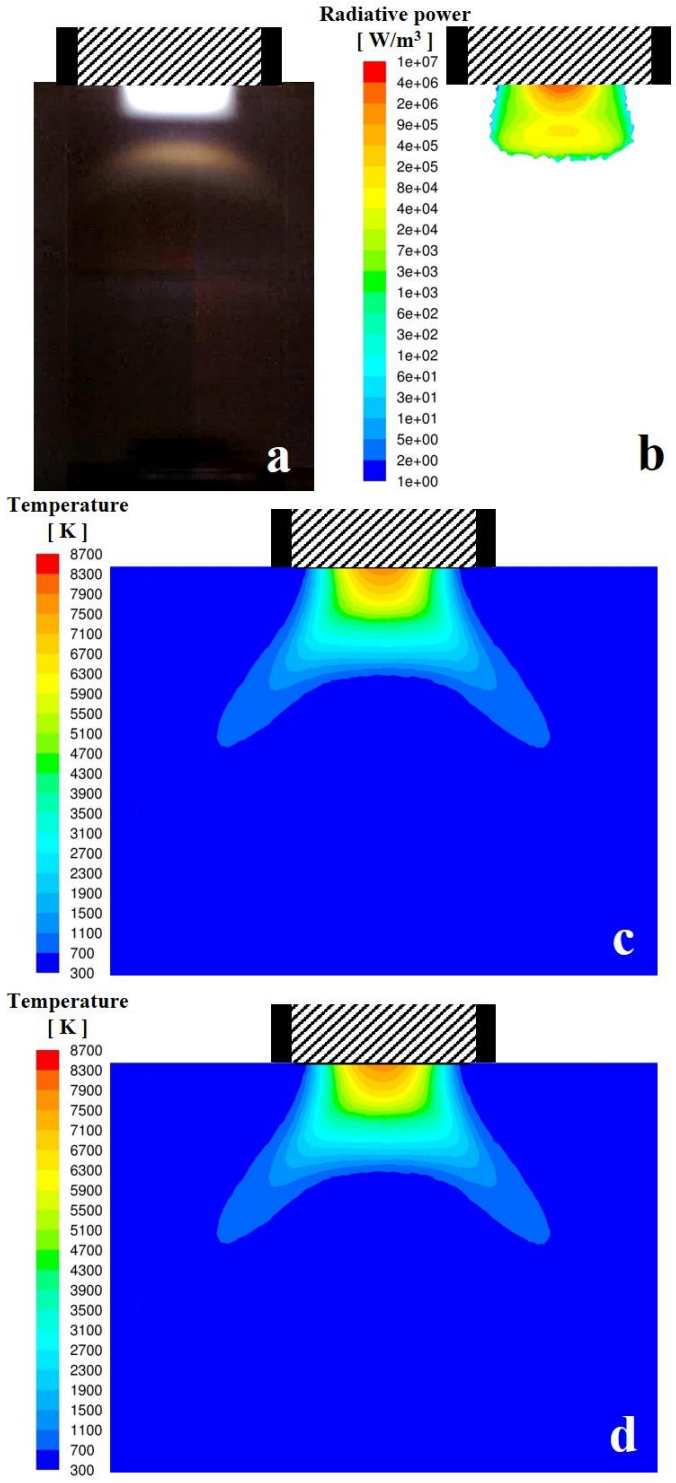

Figure 1.17. Comparison between experimental and numerical results of the 3-D simulation for operating condition B: side view of the plasma plume obtained from HSI (a), contours of simulated radiative power losses (b) and simulated temperature distribution on plane *xz* (c) and *yz* (d). The non-striped pattern in the torch represents the confinement tube [71].

Frames obtained from SI of the operating conditions A and B are shown in Figure 1.18 and Figure 1.19, respectively. A plasma plume laminar at the outlet of the torch with the onset of a few eddies on the fringes of the jet can be observed for condition A (Figure 1.18), while for

condition B an intense turbulent behavior is shown (Figure 1.19). A comparison between frames obtained from SI and plots of the velocity vectors for conditions A and B is reported in Figure 1.20, showing a good qualitative agreement between experimental results and simulations. In Figure 1.20a and 1.20b a laminar plasma plume is clearly visible and the mixing with surrounding air occurs only at its boundaries or farther than twice the inner diameter of the quartz tube. Also for condition B the calculated velocity vectors reproduce properly the bow-like geometry of the plasma plume and show the counter flow of air moving towards the quartz tube (Figure 1.20c and 1.20d), with turbulent phenomena related to air-Ar mixing taking place both in the central and in the external parts of the plume.

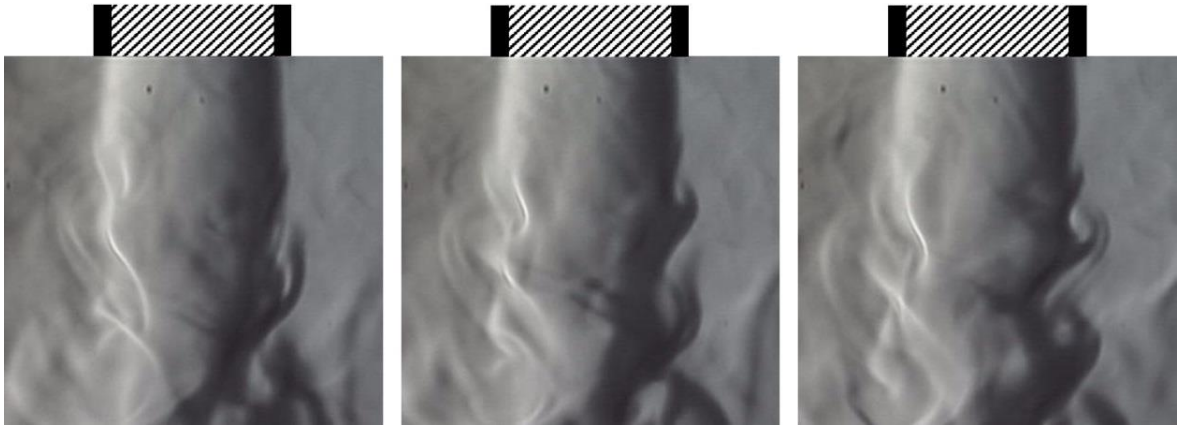

Figure 1.18. Sequential frames at 250 fps of SI side views for operating condition A. The non-striped pattern in the torch represents the confinement tube [71].

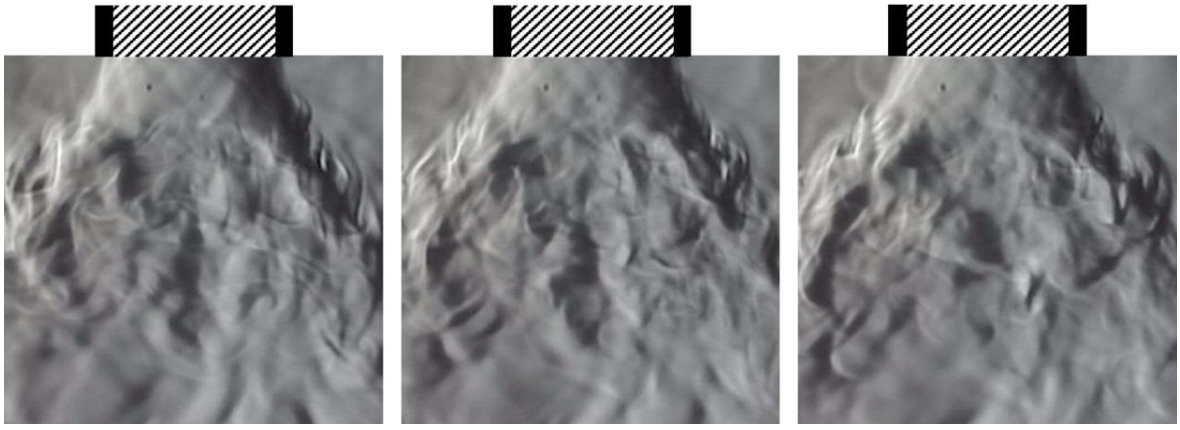

Figure 1.19. Sequential frames at 250 fps of SI side views for operating condition B. The non-striped pattern in the torch represents the confinement tube [71].

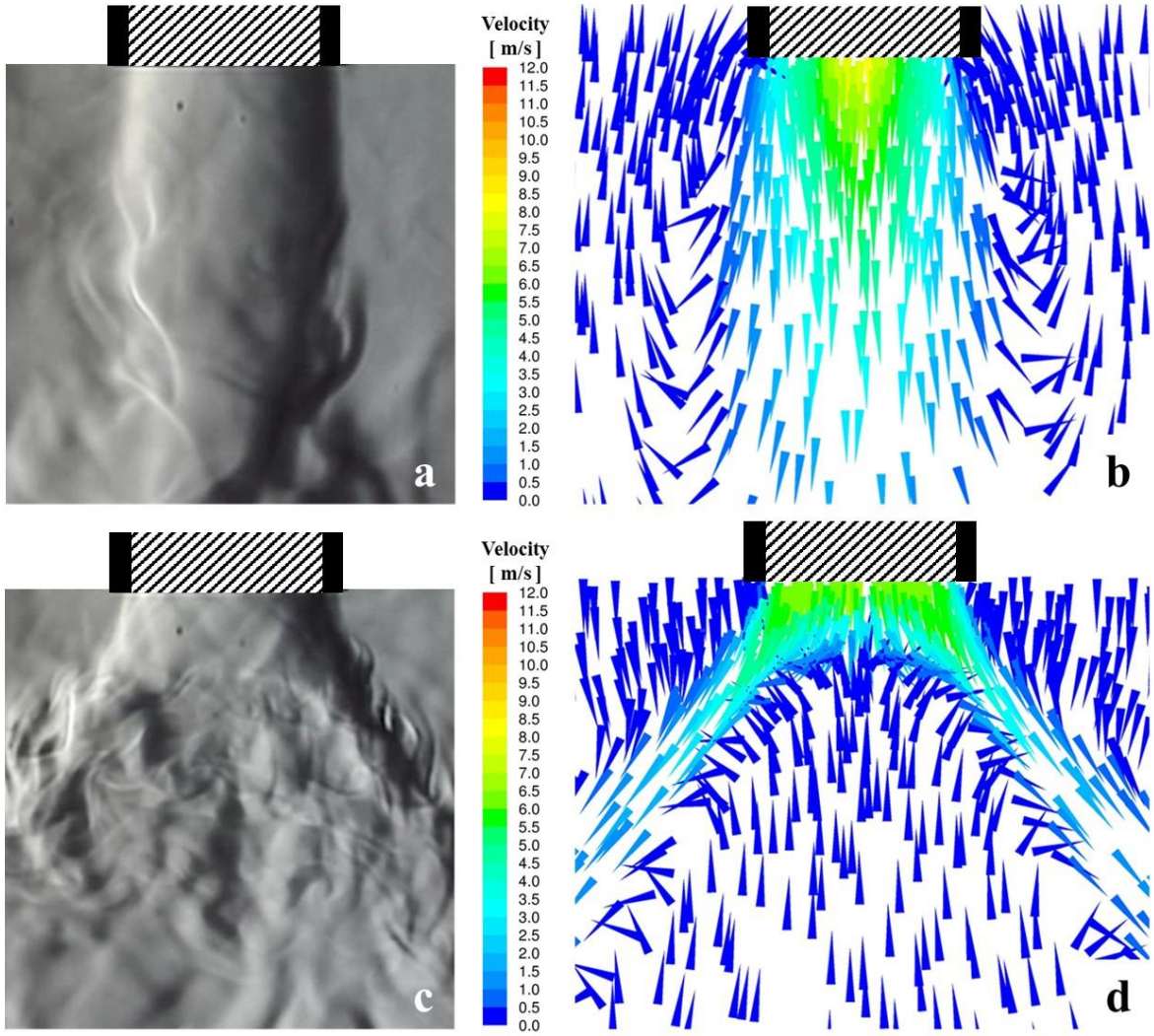

Figure 1.20. Comparison between experimental and numerical results of 3-D simulations for operating conditions A and B: side view SI of the plasma plume (a) and simulated vector velocity field for condition A on plane *xz* (b); side view SI of the plasma plume (c) and vector velocity field for condition B on plane *xz* (d). The non-striped pattern in the torch represents the confinement tube [71].

SI frames of the operating condition C are shown in Figure 1.21. The interaction between the effluent of the discharge and the substrate induces an increase of turbulence with respect to a similar condition in a free flow regime (Figure 1.18); turbulent wave fronts can be observed propagating along the surface of the substrate from the impingement region. Velocity vector fields and temperature contours in the region where the RF torch effluent impinges on the substrate for the operating condition C are reported in Figure 1.22 and Figure 1.23, respectively. In this case a strong interaction occurs between the plasma plume and the substrate: the plume is split by the substrate (top part of Figure 1.22b and bottom part of Figure 1.22c) and eddies are formed sideways and below the substrate. In this case the temperature of the substrate is higher than 500 K, (up to 820 K in the central part of the substrate), with consequent changes

in the SS substrate oxidation and surface color [87]. In industrial applications such as high purity silica overcladding of preforms, the substrate is rotated and either the plasma source or the substrate translated, with an expected reduction on the substrate maximum temperature with respect to this idealized steady state process condition; which was used in order to simplify the acquisitions of the experimental data and avoid any perturbations due to substrate or torch movement.

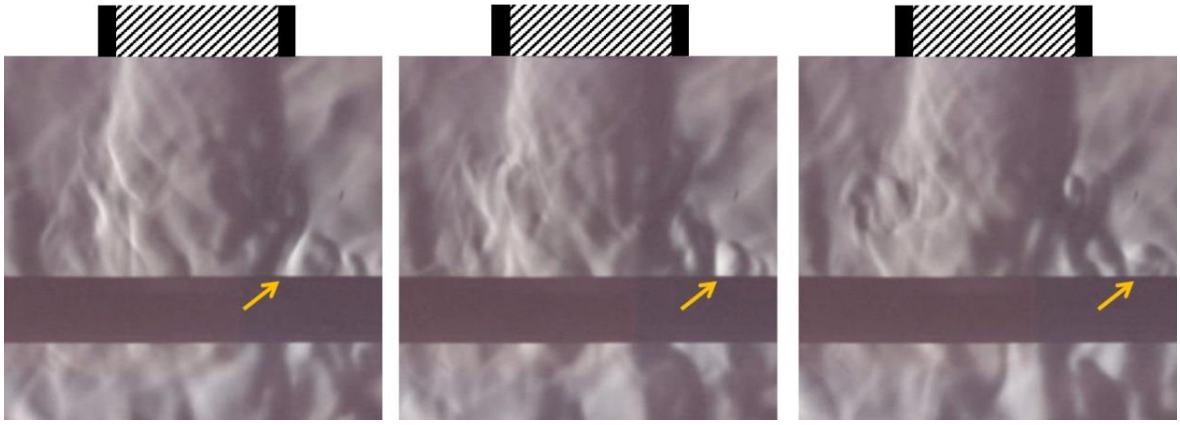

Figure 1.21. Sequential frames at 250 fps of SI side views for operating condition C, from a point of view perpendicular to the axis of the substrate. A turbulent wave front on the surface of the substrate is tracked by orange arrows. The non-striped pattern in the torch represents the confinement tube [71].

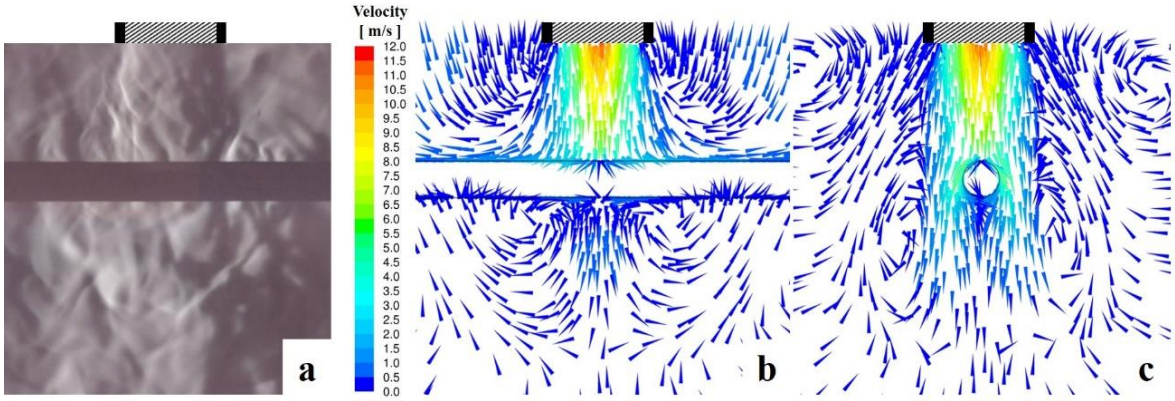

Figure 1.22. Comparison between experimental and numerical results of 3-D simulations for operating condition C: side view SI of the plasma plume (a) and simulated vector velocity field plotted on plane *xz* (b) and on plane *yz* (c). The non-striped pattern in the torch represents the confinement tube [71].

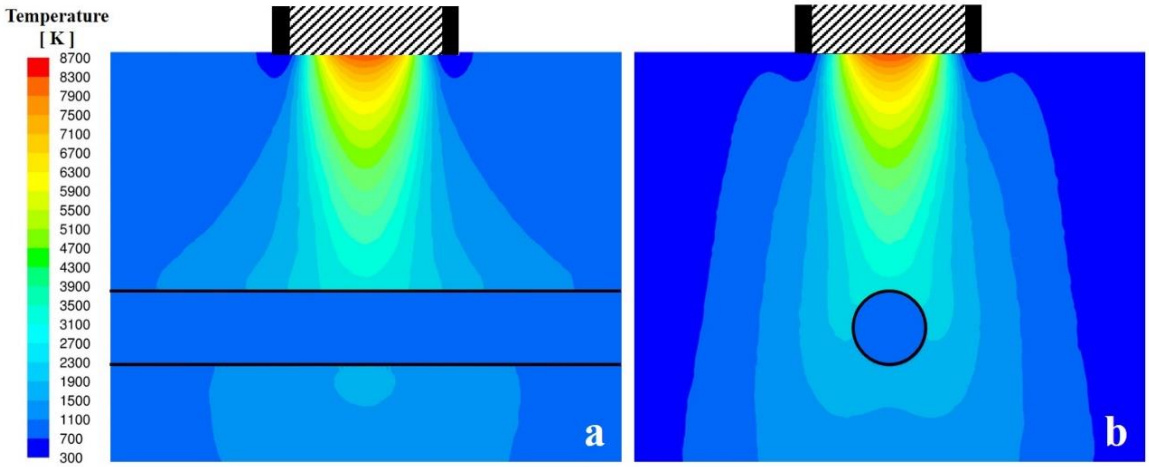

Figure 1.23. 3-D simulated contours of the temperature field plotted on plane *xz* (a) and on plane *yz* (b) in the region where the RF effluent impinges on the substrate while operating in condition C. The non-striped pattern in the torch represents the confinement tube [71].

Also the behavior of the jet of the RF torch operating in condition D while impinging on the cylindrical substrate has been analysed. Frames obtained from SI of the operating condition D from two perpendicular points of view are shown in Figure 1.24. A holder has been used to support the substrate while its axis is coaxial with the collimated beam (see picture in Figure 1.4). The holder disturbs the quality of SI imaging as it is shown in the bottom sequence of Figure 1.24. but it is not affecting the behavior of the torch effluent, being placed at one terminal end of the substrate. The plasma plume seems to be unaffected by the presence of the substrate, showing a similar behavior to the one observed in a free flow regime (condition B, Figure 1.19) for both the points of view.

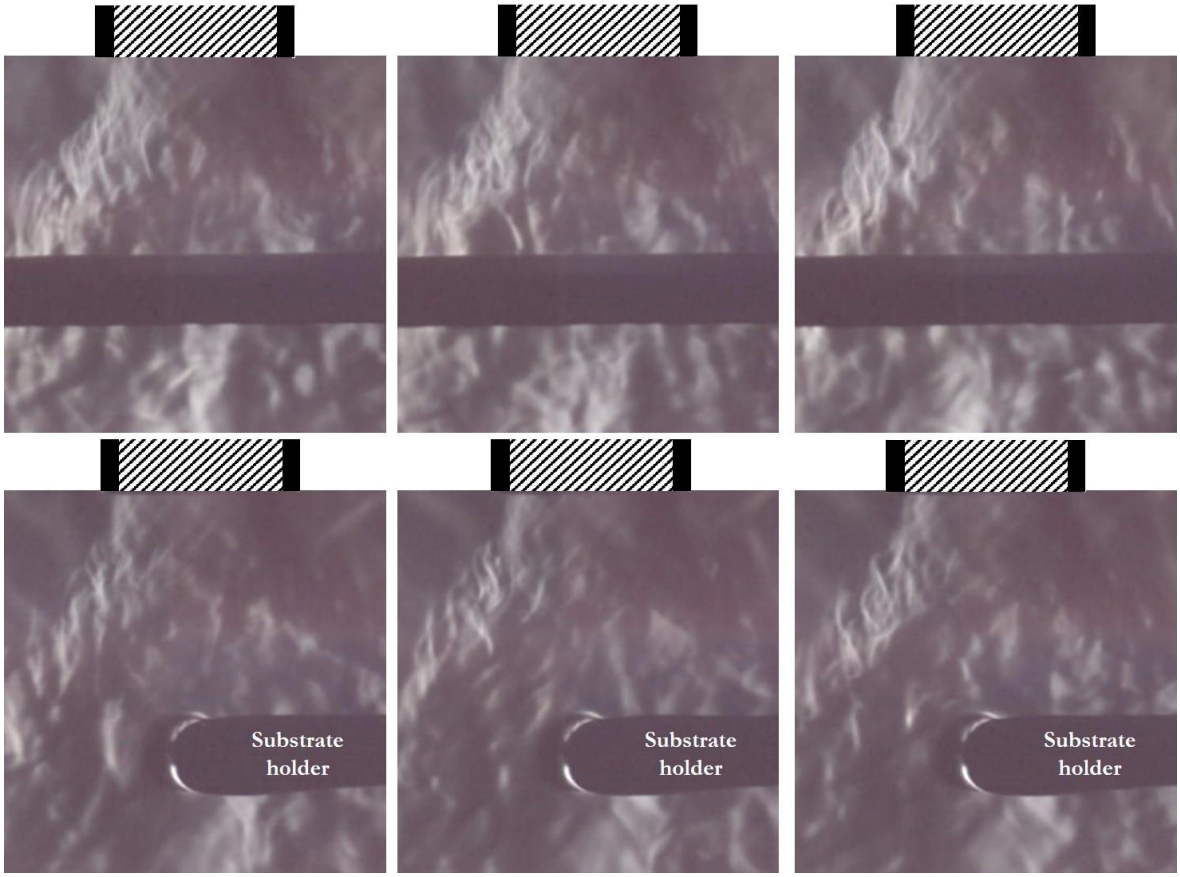

Figure 1.24. Sequential frames at 250 fps of SI side views for operating condition D. Two perpendicular points of view are presented: one perpendicular to the axis of the substrate (top) and one parallel to it (below). The non-striped pattern in the torch represents the confinement tube [71].

The comparison between frames obtained from SI and plots of the simulative velocity vectors from two perpendicular points of view, is reported in Figure 1.25. Also the velocity vectors field shows that the presence of the substrate downstream the exit of the torch doesn't affect significantly the overall shape of the plasma plume with respect to a similar condition (B) without any substrate (as shown in Figure 1.20d). The air counter flow is still present, surrounding the substrate while moving towards the torch outlet (Figure 1.20d).

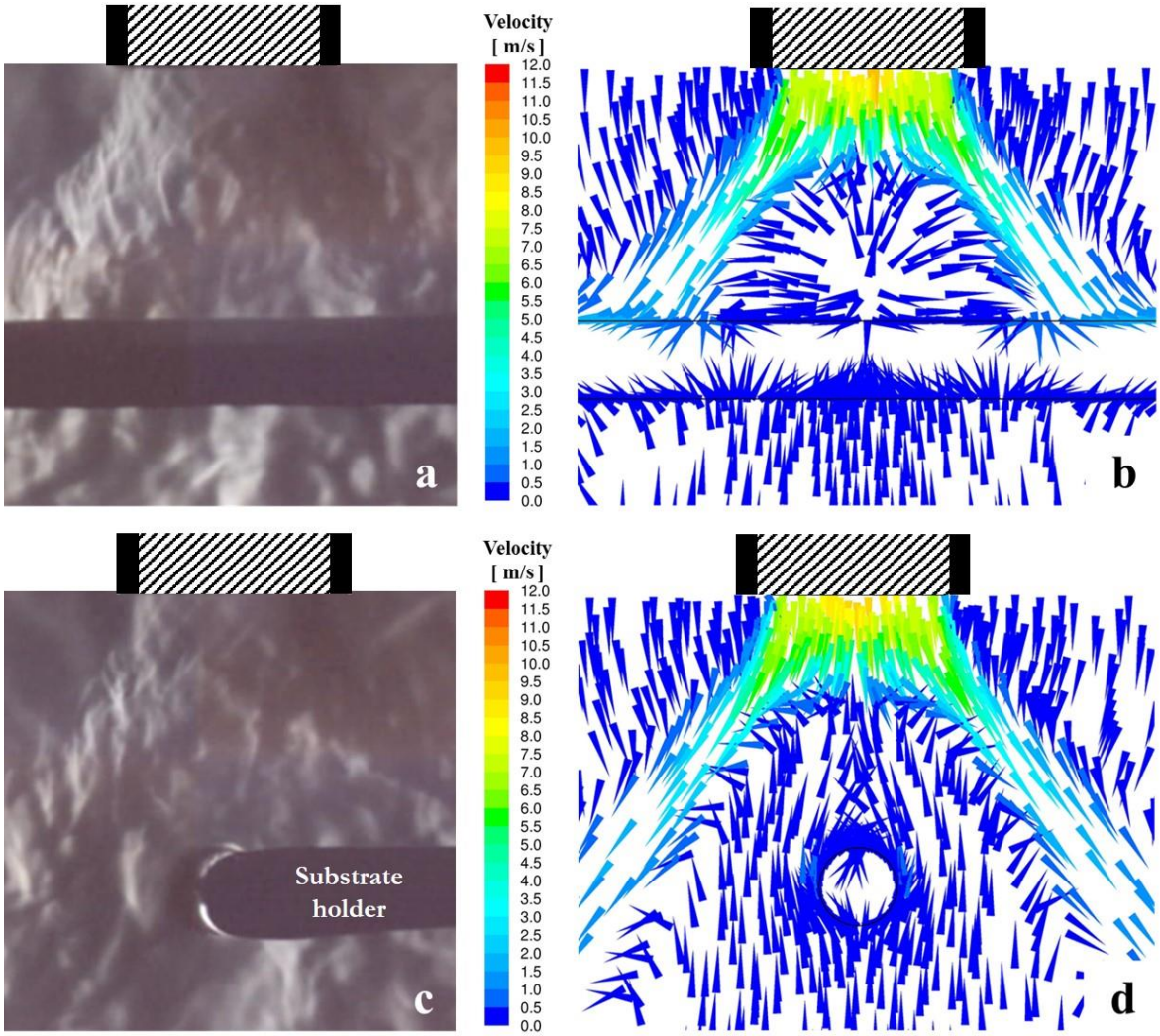

Figure 1.25. Comparison between SI side views (a, c) and 3-D simulated vector velocity field (b, d) of the region where the RF effluent impinges on the substrate while operating in condition D. Two perpendicular points of view are presented: one perpendicular to the axis of the substrate (a, b) and one parallel to the axis of the substrate (c, d). Vector velocity fields are plotted on plane *xz* (b) and *yz* (d) respectively. The non-striped pattern in the torch represents the confinement tube [71].

Also, the temperature contours reported in Figure 1.26 show that the interaction between the effluent of the discharge and the substrate is quite limited, as the latter reaches temperatures which are fairly lower than the ones of the melting range (1673 - 1723 K) [84]. The experimental temperature is 503 K, while the simulated one at the same point is 461 K.

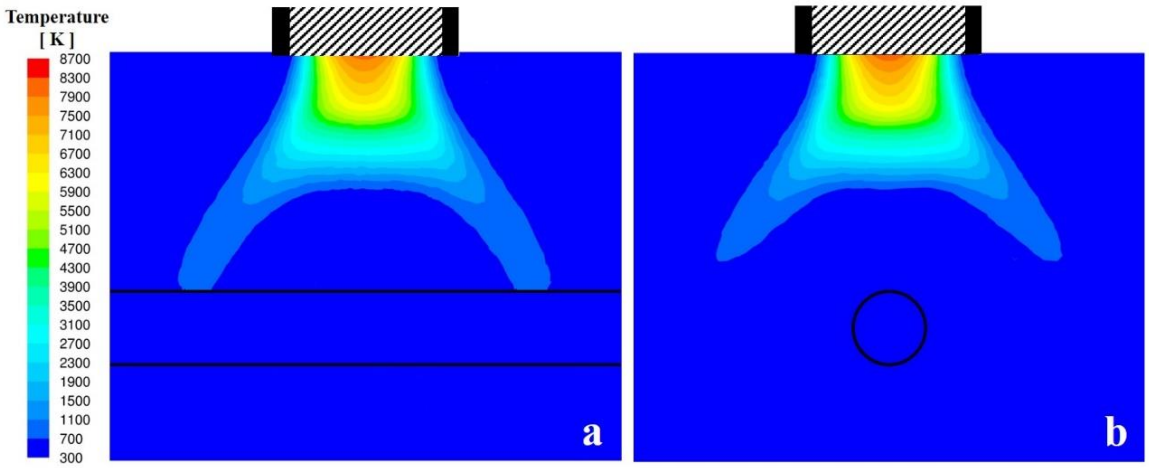

Figure 1.26. 3-D simulated contours of the temperature field plotted on plane *xz* (a) and on plane *yz* (b) in the region where the RF effluent impinges on the substrate while operating in condition D. The non-striped pattern in the torch represents the confinement tube [71].

The profiles of calculated temperature along the top generatrix of the cylindrical substrate for conditions C and D are shown in Figure 1.27. For condition C we can observe that there is a difference of more than 300 K between the center of the substrate and its peripheral zones, caused by the restricted area of interaction of the effluent of the discharge with the substrate. For condition D the average temperature compared to case C is lower along the whole line as the interaction of the plasma plume with the substrate is reduced. However, it shall be noticed that with this operating condition the highest temperatures are located in the two spots where the plume impinges on the substrate generating a zone between them (about 40 mm long) where the temperature is almost uniform and higher with respect to the rest of the substrate.

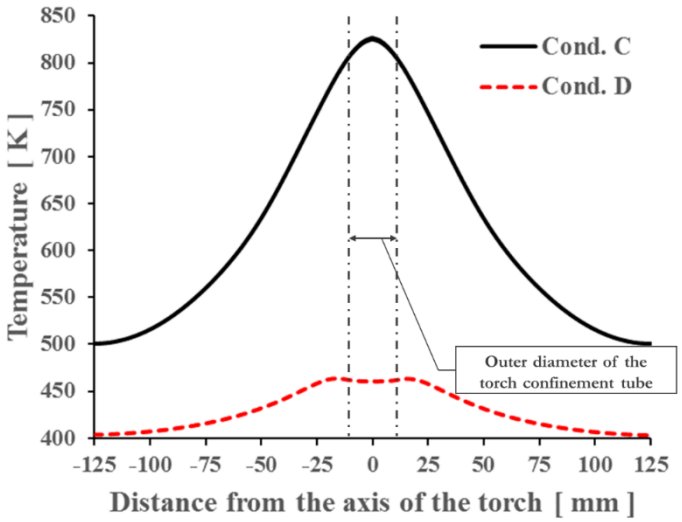

Figure 1.27. Profiles of calculated temperature on the top generatrix of the cylindrical substrate, (laying on plane *xz)* for the operating conditions C and D [71].

Concluding, temperatures isosurfaces are reported in Figure 1.28 to have a 3-D comparison of the shape of the plasma plumes obtained for the different operating conditions and configurations studied. When no substrate is present, the plasma plume shows a symmetrical shape (Figure 1.28A and 1.28B), while the presence of the substrate in the downstream region leads to an asymmetrical behavior of the plasma plume, caused by the interaction of the swirled gas flow with the substrate, as shown in Figure 1.28D. This behavior doesn't occur for operating condition C, as shown in Figure 1.28C, as it seems that the jet-like behavior reduces the region of interaction between the effluent and the substrate, showing a plane-symmetric behavior with *xz* as mirror plane. Based on these results, the behavior of the effluent of the RF torch while impinging on the substrate couldn't be studied solely performing 2-D axisymmetric simulations, as they would neglect phenomena that could induce a non-uniform treatment of the substrate, as shown in Figure 1.28D.

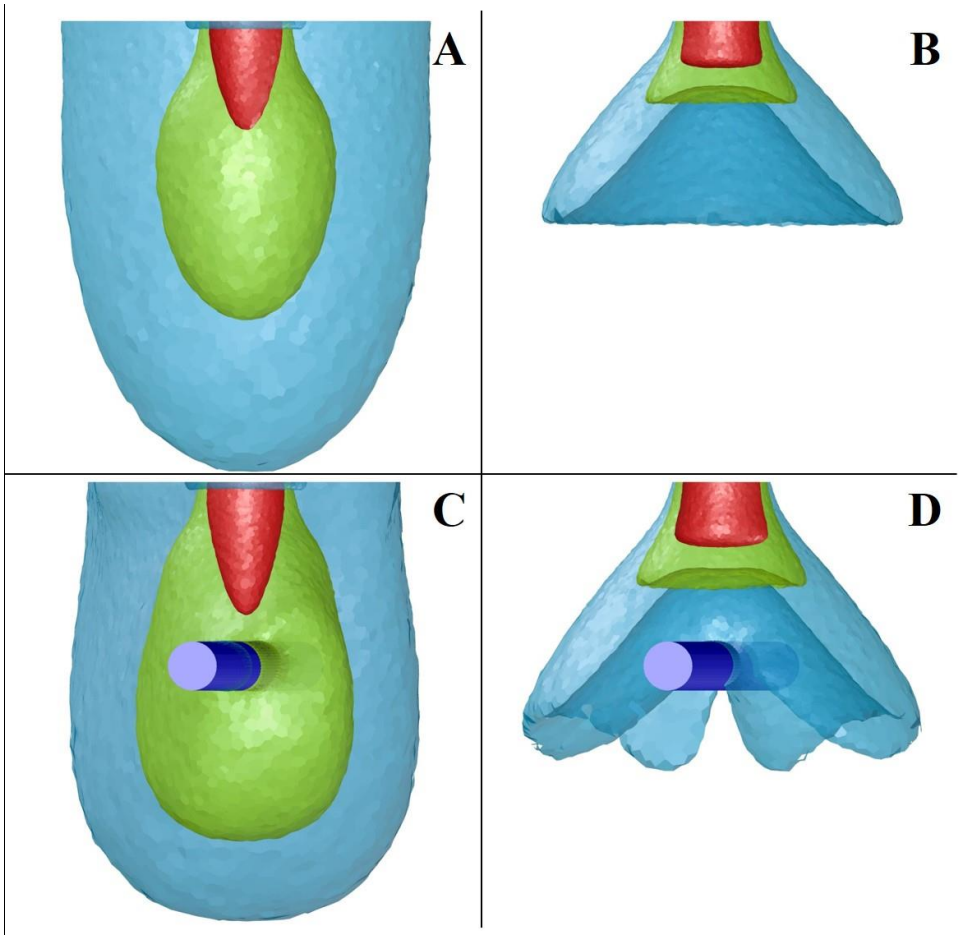

Figure 1.28. 3-D simulated temperature isosurfaces (red 3000 K, green 1000 K, teal blue 500 K) of the plasma plume studied in the four different operating conditions: condition A (A), condition B (B), condition C with the presence of the substrate (C) and condition D with the presence of the substrate (D) [71].

1.5. Conclusions

In this chapter an integrated approach was shown, based on the comparison of simulative and experimental data, for the design and the optimization of industrial processes assisted by RF thermal plasmas. A detailed investigation and characterization of the behavior of the effluent of a low-power atmospheric pressure RF plasma torch, operated at different power levels and with different gas flow rates, in a free flow regime or impinging on a cylindrical SS substrate has been performed, using simulations and diagnostics techniques and comparing their results. At first, the plasma discharge sustained in the torch was simulated under 2-D axisymmetric and LTE hypotheses for four operating conditions, so with the main aim of obtaining temperature and velocity profiles at the outlet of the torch. These calculated profiles were used as a hot gas boundary condition for 3-D simulations of the behavior of the effluent of the discharge in a free flow regime (operating conditions A and B) or with a substrate placed downstream the torch outlet (operating conditions C and D). HSI, SI and measurement of the temperature on the surface of the substrate by means of an IR sensor were performed to obtain experimental data, which were compared with the numerical results of the 3-D simulations in order to deeply characterize the plasma assisted test process which has been here considered as an example.

Two different behaviors of the effluent of the discharge have been observed, induced by the different sheath gas flow rates: a jet-like behavior for operating condition A and C, and a plasma plume with a bow-like geometry for operating conditions B and D. For conditions A and B, the simulated plasma temperature distributions show a good agreement with the shape of the plasma plume observed in HSI frames; on the other side, simulated contours of radiative power losses don't match with the light emitted from the plasma discharge when air entrainment in the jet occurs, as for operating condition B. This discrepancy could be ascribed to some probable non-equilibrium effects in the plasma fringes, caused by the interaction between the argon plasma and room temperature air. Further improvement to this study would be analyzing such discrepancies and use the most accurate experimental results as a tool to tune the simulation code with the aim of a better performance of process prediction.

The comparison between SI frames and the calculated vector velocity fields for the four operating conditions show that the fluid-dynamic characteristics of the plasma plume and turbulence phenomena induced by the presence of the substrate were properly reproduced by simulation. Furthermore, it was observed that for operating conditions D the presence of the

substrate downstream the torch outlet does not affect significantly the overall shape of the plasma plume, differently from condition C.

The calculated temperature fields and the experimental measurement confirm that the interaction between the effluent of the discharge and the substrate is very limited for condition D (with maximum substrate temperature lower than 500 K) compared to condition C (with maximum substrate temperature over 500 K). Condition D allows, in a static condition, to heat the substrate almost uniformly along the cylinder surface for 40 mm. However, the industrial processes by which this test study is inspired are usually carried out in dynamic conditions, with the substrates in relative motion with respect to the plasma torch (*e.g.* rotations, translations). These movements induce complex thermal and fluid-dynamic phenomena on the substrates and they should be implemented in the model to investigate a more realistic configuration, even if doing so represents a challenging task.

However, this work highlighted that, 3-D simulations are essentials to characterize the impingement of the effluent of the discharge on the substrate, as they may take into account non-axisymmetric phenomena occurring in these processes.

In accordance to the results obtained and discussed, the presented integrated approach proved to be a useful tool to in depth characterize simplified test processes assisted by low-power RF thermal plasmas, in order to design and optimize more realistic industrial ones.

References

[1]. T. B. Reed, J. Appl. Phys. **32**, 821 (1961).

[2]. J. Mostaghimi and M. I. Boulos, Plasma Chem. Plasma Process. **35**, 421 (2015).

[3]. M. I. Boulos, P. Fauchais, and E. Pfender, *Thermal Plasmas: Fundamentals and Applications* (Plenum Press, New York, 1994).

[4]. E. Pfender, Plasma Chem. Plasma Process. **19**, 1 (1999).

[5]. P. Fauchais, J. Phys. D. Appl. Phys. **37**, R86 (2004).

[6]. J. Heberlein and A. B. Murphy, J. Phys. D. Appl. Phys. **41**, 53001 (2008).

[7]. A. Montaser and D. W. Golightly, *Inductively Coupled Plasmas in Analytical Atomic Spectrometry* (Wiley-VCH, New York, NY, USA, 1992).

[8]. A. Montaser, *Inductively Coupled Plasma Mass Spectrometry* (Wiley-VCH, New York, NY, USA, 1998).

[9]. S. Neogi and J. Marin, Application of RF-inductive plasma for optical wave guide manufacture. In: ISPC-13 (1997), p.1851.

[10]. V. Colombo, C. Panciatichi, A. Zazo, G. Cocito, and L. Cognolato, IEEE Trans. Plasma Sci. **25**, 1073 (1997).
[11]. C. Panciatichi, P. Cocito, and M. C. N. De Leo, in *(Eds.), Prog. Plasma Process. Mater.*, edited by P. Fauchais and J. Amouroux (Begell House Inc, New York, USA, 1999), pp. 885–890.
[12]. B. Jouvenel and P. Ripoche, US5676863 A (1997).
[13]. E. Petitfrere, G. Lavanant, and B. Gouez, US6584806 B2 (2003).
[14]. A. Schultheis, K. Bräuer, and R. Schmidt, US9487429 B2 (2012).
[15]. A. Moradian and J. Mostaghimi, IEEE Trans. Plasma Sci. **33**, 410 (2005).
[16]. A. Moradian and J. Mostaghimi, Metall. Mater. Trans. B **39**, 280 (2008).
[17]. A. Chang, J. W. Carr, J. Kelley, and P. S. Fiske, US2005061782 A1 (2007).
[18]. C. Fanara, P. Shore, J. R. Nicholls, N. Lyford, J. Kelley, J. Carr, and P. Sommer, Adv. Eng. Mater. **8**, 933 (2006).
[19]. M. Castelli, R. Jourdain, P. Morantz, and P. Shore, Key Eng. Mater. **496**, 182 (2012).
[20]. N. Yu, R. Jourdain, M. Gourma, and P. Shore, Int. J. Adv. Manuf. Technol. **87**, 735 (2016).
[21]. Q. Xin, X. Su, S. Alavi, B. Wang, and J. Mostaghimi, Appl. Therm. Eng. **128**, 785 (2018).
[22]. V. Colombo, E. Ghedini, P. Sanibondi, M. Gherardi, A. Stancampiano, R. Laurita, A. Liguori, M. Boselli, and A. Fridman, WO2015019240 A1 (2015).
[23]. D. Barbieri, M. Boselli, F. Cavrini, V. Colombo, M. Gherardi, M. P. Landini, R. Laurita, A. Liguori, and A. Stancampiano, Biointerphases **10**, 29519 (2015).
[24]. M. I. Boulos, IEEE Trans. Plasma Sci. **6**, 91 (1978).
[25]. P. Proulx, J. Mostaghimi, and M. I. Boulos, Int. J. Heat Mass Transf. **28**, 1327 (1985).
[26]. J. Mostaghimi, P. Proulx, M. I. Boulos, and R. M. Barnes, Spectrochim. Acta Part B At. Spectrosc. **40**, 153 (1985).
[27]. J. Mostaghimi, P. Proulx, and M. I. Boulos, J. Appl. Phys. **61**, 1753 (1987).
[28]. M. Elhage, J. Mostaghimi, and M. I. Boulos, J. Appl. Phys. **65**, 4178 (1989).
[29]. J. Mostaghimi and M. I. Boulos, Plasma Chem. Plama Process. **9**, 25 (1989).
[30]. P. Yang, R. M. Barnes, J. Mostaghimi, and M. I. Boulos, Spectrochim. Acta - Part B At. Spectrosc. **44B**, 657 (1989).
[31]. J. Mostaghimi and M. I. Boulos, J. Appl. Phys. **68**, 2643 (1990).
[32]. P. Proulx, J. Mostaghimi, and M. I. Boulos, Int. J. Heat Mass Transf. **34**, 2571 (1991).
[33]. Z. Njah, J. Mostaghimi, and M. Boulos, Int. J. Heat Mass Transf. **36**, 3909 (1993).
[34]. D. Bernardi, V. Colombo, G. G. M. Coppa, and A. D'Angola, Eur. Phys. J. D **14**, 337 (2001).
[35]. D. Bernardi, V. Colombo, E. Ghedini, and A. Mentrelli, Eur. Phys. J. D-Atomic, Mol. Opt. Plasma Phys. **22**, 119 (2003).
[36]. D. Bernardi, V. Colombo, E. Ghedini, and A. Mentrelli, Eur. Phys. J. D **25**, 271 (2003).
[37]. D. Bernardi, V. Colombo, E. Ghedini, and A. Mentrelli, Pure Appl. Chem. **77**, 359 (2005).
[38]. D. Bernardi, V. Colombo, E. Ghedini, A. Mentrelli, and T. Trombetti, IEEE Trans. Plasma Sci. **33**, 424 (2005).
[39]. D. Bernardi, V. Colombo, E. Ghedini, and A. Mentrelli, Eur. Phys. J. D **25**, 279 (2003).
[40]. V. Colombo, E. Ghedini, and J. Mostaghimi, Ieee Trans. Plasma Sci. **36**, 1040 (2008).
[41]. V. Colombo, E. Ghedini, and P. Sanibondi, J. Phys. D. Appl. Phys. **43**, 105202 (2010).

[42]. M. Cai, A. Montaser, and J. Mostaghimi, Spectrochim. Acta Part B At. Spectrosc. **48**, 789 (1993).
[43]. M. Cai and A. Montaser, Appl. Spectrosc. **49**, 1390 (1995).
[44]. M. Cai, D. a. Haydar, A. Montaser, and J. Mostaghimi, Spectrochim. Acta Part B At. Spectrosc. **52**, 369 (1997).
[45]. C. M. Benson, S. F. Gimelshein, D. A. Levin, and A. Montaser, Spectrochim. Acta - Part B **56**, 1097 (2001).
[46]. C. M. Benson, J. Zhong, S. F. Gimelshein, D. A. Levin, and A. Montaser, Spectrochim. Acta Part B **58**, 1453 (2003).
[47]. H. Lindner and A. Bogaerts, Spectrochim. Acta - Part B At. Spectrosc. **66**, 421 (2011).
[48]. H. Lindner, A. Murtazin, S. Groh, K. Niemax, and A. Bogaerts, Anal. Chem. **83**, 9260 (2011).
[49]. M. Aghaei, H. Lindner, and A. Bogaerts, Spectrochim. Acta - Part B At. Spectrosc. **76**, 56 (2012).
[50]. M. Aghaei, H. Lindner, and A. Bogaerts, J. Anal. At. Spectrom. **27**, 604 (2012).
[51]. M. Aghaei, H. Lindner, and A. Bogaerts, J. Anal. At. Spectrom. **28**, 1485 (2013).
[52]. M. Aghaei, L. Flamigni, H. Lindner, D. Gunther, and A. Bogaerts, J. Anal. At. Spectrom. **29**, 249 (2014).
[53]. M. Aghaei and A. Bogaerts, J. Anal. At. Spectrom. **31**, 631 (2016).
[54]. A. Bogaerts and M. Aghaei, J. Anal. At. Spectrom. **32**, 233 (2017).
[55]. M. Shigeta, T. Sato, and N. H., Thin Solid Films **435**, 5 (2003).
[56]. M. Shigeta, T. Sato, and H. Nishiyama, Int. J. Heat Mass Transf. **47**, 707 (2004).
[57]. M. Shigeta and T. Watanabe, J. Mater. Res. **20**, 2801 (2005).
[58]. T. Watanabe, M. Shigeta, and N. Atsuchi, Int. J. Heat Mass Transf. **49**, 4867 (2006).
[59]. T. Watanabe, N. Atsuchi, and M. Shigeta, Thin Solid Films **49**, 1073 (2006).
[60]. M. Shigeta and T. Watanabe, J. Appl. Phys. **103**, 74903 (2008).
[61]. M. Shigeta, Plasma Sources Sci. Technol. **21**, 55029 (2012).
[62]. J. A. Horner and G. M. Hieftje, Spectrochim. Acta Part B **53**, 1235 (1998).
[63]. P. Yang, J. A. Horner, N. N. Sesi, and G. M. Hieftje, Spectrochim. Acta, Part B At. Spectrosc. **55**, 1833 (2000).
[64]. M. Baeva and D. Uhrlandt, Surf. Coatings Technol. **204**, 4044 (2010).
[65]. K. Y. Nagulin, D. S. Akhmetshin, A. K. Gilmutdinov, and R. a. Ibragimov, J. Anal. At. Spectrom. **30**, 360 (2015).
[66]. K. Y. Nagulin, I. V. Tsivilskiy, D. S. Akhmetshin, and A. K. Gilmutdinov, Spectrochim. Acta - Part B At. Spectrosc. **135**, 63 (2017).
[67]. M. Boselli, F. Cavrini, V. Colombo, E. Ghedini, M. Gherardi, R. Laurita, A. Liguori, P. Sanibondi, and A. Stancampiano, IEEE Trans. Plasma Sci. **42**, 2748 (2014).
[68]. M. A. Razzak, K. Kondo, Y. Uesugi, N. Ohno, and S. Takamura, J. Appl. Phys. **95**, 427 (2004).
[69]. D. Vacher, M. Lino da Silva, P. André, G. Faure, and M. Dudeck, Plasma Sources Sci. Technol. **17**, 35012 (2008).
[70]. T. Tamura, Y. Kaburaki, R. Sasaki, H. Miyahara, and A. Okino, IEEE Trans. Plasma Sci. **39**, 1684 (2011).
[71]. E. Traldi, M. Boselli, M. Gherardi, and V. Colombo, *A Simulative and Experimental*

Approach for the Design and Optimization of Atmospheric Pressure Low Power RF Thermal Plasma Processes, Plasma Process. Polym. **14**, 1600167 (2017), DOI: 10.1002/ppap.201600167, Copyright © 2016 WILEY-VCH Verlag GmbH & Co. KGaA, Weinheim. Reproduced with permission.
[72]. ANSYS Fluent Theory Guide – Release 15.0 (ANSYS Inc., 2013).
[73]. S. Xue, P. Proulx, and M. I. Boulos, Plasma Chem. Plasma Process. **23**, 245 (2003).
[74]. A. B. Murphy and C. J. Arundelli, Plasma Chem. Plasma Process. **14**, 451 (1994).
[75]. Y. Naghizadeh-Kashani, Y. Cressault, and A. Gleizes, J. Phys. D. Appl. Phys. **35**, 2925 (2002).
[76]. Y. Cressault and A. Gleizes, J. Phys. D. Appl. Phys. **46**, 415206 (2013).
[77]. A. Gleizes, Y. Cressault, and P. Teulet, Plasma Sources Sci. Technol. **19**, 55013 (2010).
[78]. J. J. Lowke and E. R. Capriotti, J. Quant. Spectrosc. Radiat. Transf. **9**, 207 (1969).
[79]. J. J. Lowke, J. Quant. Spectrosc. Radiat. Transf. **14**, 111 (1974).
[80]. A. Gleizes, M. Gongassian, and B. Rahmani, J. Phys. D. Appl. Phys. **22**, 83 (1989).
[81]. A. Gleizes, B. Rahmani, J. J. Gonzalez, and B. Liani, J. Phys. D. Appl. Phys. **24**, 1300 (1991).
[82]. A. Gleizes, J. J. Gonzalez, B. Liani, and G. Raynal, J. Phys. D. Appl. Phys. **26**, 1921 (1993).
[83]. T. Billoux, Y. Cressault, P. Teulet, and A. Gleizes, J. Phys. Conf. Ser. **406**, 12010 (2012).
[84]. North American Stainless, Flat Products Stainless Steel Grade Sheet (2007).
[85]. M. Boselli, V. Colombo, E. Ghedini, M. Gherardi, R. Laurita, A. Liguori, P. Sanibondi, and A. Stancampiano, Plasma Chem. Plasma Process. **34**, 853 (2014).
[86]. M. Boselli, V. Colombo, M. Gherardi, R. Laurita, A. Liguori, P. Sanibondi, E. Simoncelli, and A. Stancampiano, IEEE Trans. Plasma Sci. **43**, 713 (2015).
[87]. British Stainless Steel Association, Heat tint (temper) colours on stainless steel surfaces heated in air, https://www.bssa.org.uk/topics.php?article=140, (June, 2016).

2. Design and Optimization of Processes Assisted by Cold Atmospheric Pressure Plasma Sources for the Modification of Synthetic and Natural Polymeric Materials' Wettability

2.1. Literature Overview

Mankind has been employing polymers for thousands of years by using those naturally available, such as cotton, silk, linen and wool, although it has been unaware of their nature and great potentialities for long. Since the nineteenth century several studies have been carried in polymer science to comprehend and exploit polymers' characteristics, leading in the last decades to a global explosion in the production of polymeric materials. This phenomenon is due to the polymers' low-cost and the possibility to use them to obtain materials with various mechanical, thermal, electrical and chemical properties. In this frame several kinds of polymers have been realized, spanning from plastics available in everyday life, *e.g.* Polyethylene (PE), to high performance thermoplastics with extremely high chemical and thermal resistance, *e.g.* Polyether ether ketones (PEEK) and Polytetrafluoroethylene (PTFE) [1].

However, innovative and demanding applications can require specific combinations of mechanical, chemical and biological properties that can't be met by a polymer as made. In this perspective surface treatments are a valuable solution to overcome this issue: indeed, they enable to modify the surface chemical and biological properties of a polymeric substrate without affecting the mechanical properties, defined by the bulk properties of the material [2]. According to this strategy several methods to treat polymeric materials have been developed and employed to date in the industrial production of textiles, packaging materials, automotive components, membranes, biomedical devices and scaffolds [3–5].

Since the development of the first corona treatment by V. Eisby and the first deliberate deposition process performed by Goodman in 1960 [6,7], non-equilibrium plasmas have become a fundamental technology for polymers' surface processing. According to Wertheimer [6], non-equilibrium plasmas can affect polymeric surfaces by means of four main mechanisms: etching, functionalization, cross-linking and deposition. In the etching process, solid material is removed from the surface: this effect is produced by the ion bombardment and the energetic vacuum-UV radiation at low operating pressure and by chemical reactions at low and atmospheric operating pressure. The first two mechanisms produce scission reactions induced by energetic collisions or the absorption of photons, the last one consists of the interactions between the reactive species in the plasma discharge and the polymeric surface, that can lead to the gasification of the polymer [6,8]. The deposition process is almost the opposite of etching: a gaseous precursor, such as an organic monomer vapour or a reactive gas, is introduced in the reactive environment of the plasma discharge. Inside the discharge the precursor is subjected to different phenomena, such as chemical reactions and dissociations induced by high energy electron collisions, producing radicals and volatile fragments that can be deposited on the substrate via surface-chemical reactions thus producing an organic or inorganic coating [6,9]. In functionalization, the plasma discharge is generated in a non-polymerizable gas (usually O_2, N_2, NH_3, noble gases) and it affects the polymers by means of energetic particles, radicals and UV radiation, breaking the covalent bonds on the surface polymer's molecules and producing active surface sites. These sites can react with the reactive species in the plasma forming functional groups on the material surface, such as hydroxyl and carboxylic groups, which modify the material surface chemistry and accordingly its wettability, adhesive bond strength and other properties [6,8,9]. Finally, cross-linking is sustained by the same mechanisms of functionalization, but in this case the reactions take place between two radicals on polymer chains thus forming a bridge between them [5,10]. Usually these mechanisms occur at the same time during a plasma treatment and the operating parameters of the process, such as the gas composition, the pressure, the power supply's characteristics and the geometry of the source, are fundamental to determine which mechanism is dominant over the others [5,8].

The described variety of effects that non-equilibrium plasma treatments can induce on polymers' surface makes them interesting and valuable for scientific research and industry, allowing to adopt different surface modification strategies according to process-constraints. Among all the possible surface modifications that can be obtained using this technology, probably the one more frequently carried out is the modification of polymers' wettability; its level and potential modification impacts the manufacturing of several products, such as

biomaterials and medical devices, flexible and printed electronics, textiles, packaging materials and many others [5,10–15]. The modification of polymeric materials' wettability can be performed adopting different plasma processes, such as functionalization and coating deposition, usually focused on affecting the surface chemistry of the material without altering the surface roughness. Indeed, by introducing hydrophilic (hydroxyl, carboxylic, alcoholic, amine) or hydrophobic (fluorine, silane) functional groups onto the surface, plasma functionalization can increase or decrease the surface energy and consequently the wettability. The same effects can be achieved depositing thin films characterized by desired functional groups or grafting them on the plasma functionalized surface.

As described, both low pressure and atmospheric pressure cold plasmas have been widely employed to induce surface modification of polymers. Nevertheless, CAPs are becoming the most pervasive industrial technology in this field since they do not require expensive vacuum systems and they can be easily implemented in existing production lines, even if they usually lack in the fine control of the plasma chemistry and physics with respect to low pressure plasmas. In this perspective, most of the literature on CAPs is focused on fundamental studies, in which several aspects that are relevant to employ CAP technology in industrial systems are not considered, such as the difficult to operate in controlled atmosphere. Consequently, it is necessary and important to integrate fundamental studies with the one concerning industrial-scale feasibility, in order to develop processes that can really be effective in the production of high value-added polymeric materials.

Most of my Ph.D. studies were aimed at the design, optimization and implementation of CAP technology in industrial systems: in the following pages two of these studies are presented, concerning the modification of polymers' wettability by means of different surface modification mechanisms. In the first study, a plasma-functionalization process to increase the hydrophilicity of polyester mats to improve their biocompatibility was developed and characterized. The obtained results and information led to the realization of a preindustrial prototype designed to carry out the same process in realistic operating conditions. In the second one, the design and characterization of a plasma source for the hydrophobizaton of cotton threads in dynamic conditions are described, reporting also the preliminary study on the deposition of fluorocarbon coatings that was carried out in a static configuration.

2.2. *Dielectric Barrier Discharge Plasma Source for In-line Treatment of Polymeric Films to Increase their Wettability: Preliminary Study and Up-scale of the Plasma Source*

2.2.1. Introduction

The constant innovations in the biomedical field require the production of disposable and non-disposable medical devices and scaffolds with tailored properties. Thanks to the higher flexibility in the design of the shape as well as the superior possibility to tailor the physical and chemical characteristics of the final products, usually combined with reduced production costs, polymers increasingly play a dominant role in the realization of these devices with respect to "traditional" materials, such as metals, ceramics and glass [1]. An example of this trend is the extensive use for biomedical applications of polyesters, such as Polyethylene terephthalate (PET), Polybutylene terephthalate (PBT) and their blends: their thermal, mechanical, and chemical properties make them a functional material to produce medical instruments, vascular grafts, labware, blood filters, artificial heart valve sewing rings and medical textiles. However, their chemical and biological properties could be unsatisfactory for certain applications, since they could present a low hemocompatibility or a low selectivity in the filtration of specific cells thus producing failures when employed as made [16–18].

As mentioned above, the use of cold plasmas for the surface modification of polymers is a reliable and valuable solution in this perspective, as this technology allows to deeply modify the surface properties of the treated materials without affecting the bulk characteristics [2,5,13,19]. Several plasma techniques can be employed to obtain surfaces with specific characteristics, such as plasma functionalization, plasma-polymerization (deposition), plasma post-irradiation grafting and syn-irradiation grafting [5]. Plasma functionalization is the simplest among these processes, as it can be performed using only non-polymerizable gases such as He, Ar, N_2 or air to introduce functional groups or produce free radicals on the surfaces, thus without the need of monomers or other chemical reagents [5,19].

At atmospheric pressure, this kind of treatment has been performed on industrial scale using corona sources since the fifties, however Dielectric Barrier Discharge (DBD) configurations have become widely employed for this purpose recently, since they can more easily prevent surface damages induced by the discharge and can be operated with simpler power supplies [20].

Plasma functionalization is mainly employed to increase the hydrophilicity of materials, which can be a fundamental characteristic for several applications of polyesters, especially to increase their blood compatibility and filtration efficiency [16,21–25]. In this perspective, several studies have been performed on the plasma functionalization of PET and PBT to increase their wettability using both low pressure plasmas [17,26,27] and CAPs [24,28–30].

Hereunder, a preliminary investigation on the potentialities of plasma functionalization of PBT mats using a lab-scale DBD source operated in nitrogen is reported. The effects of the treatment on the polymers' wettability and morphology were evaluated and the information obtained from this study was used to design and develop a DBD plasma source. This plasma source was opportunely implemented in a preindustrial Roll-to-Roll machine, thus realizing a prototype plasma system suitable to perform feasibility studies on in-line treatment of polymeric materials.

2.2.2. Large Area Plasma Surface Treatment for the Increase of the Hydrophilicity of PBT Mats

2.2.2.1. Materials and Methods

To perform the plasma functionalization treatment on PBT mats with a surface area up to 600 cm^2, a volumetric DBD source with a liquid high voltage (HV) electrode was realized and employed in the experimental setup depicted in Figure 2.1a. The plasma discharge volume is approximately 210 x 300 x 1 mm^3 and it is enclosed in a Polycarbonate (PC) structure (Figure 2.1b), which is constituted of the dielectric barrier (a PC sheet 5 mm thick) and a rectangular PC chamber containing the ground electrode, as can be seen in Figure 2.1a. Two gas fittings at the ends of the PC structure act as gas inlet and gas outlet, thus allowing to flush a desired gas mixture inside the plasma source. The liquid HV electrode is powered by a HV amplifier (Trek model 30/20-H-CE) connected to a function generator (Stanford Research model DS335, 3

MHz) and the voltage signal employed is characterized by a square waveform with a Peak Voltage (PV) and a frequency of 18 kV and 500 Hz, respectively. The ground electrode consists of an aluminium plate 5 mm thick whose edges were rounded and electrically insulated. PBT samples, with a thickness of 200 μm, have their edges fixed on the ground electrode by means of insulating tape. Before the ignition of the plasma discharge, 5 slpm of N_2 (purity ≥99,98%) are introduced into the reaction chamber for 1 minute to purge the discharge volume. The gas flow passes through a diffuser realized with glass wool, which ensures a better distribution of the gas in the discharge volume. The same flow rate is kept constant for the whole treatment time of 3 minutes. During the tests, the voltage and current waveforms were acquired using a HV probe (Tektronix Tektronix P6015A) and a current probe (Pearson 6585) connected to an oscilloscope (Tektronix DPO 40034), as shown in Figure 2.1a.

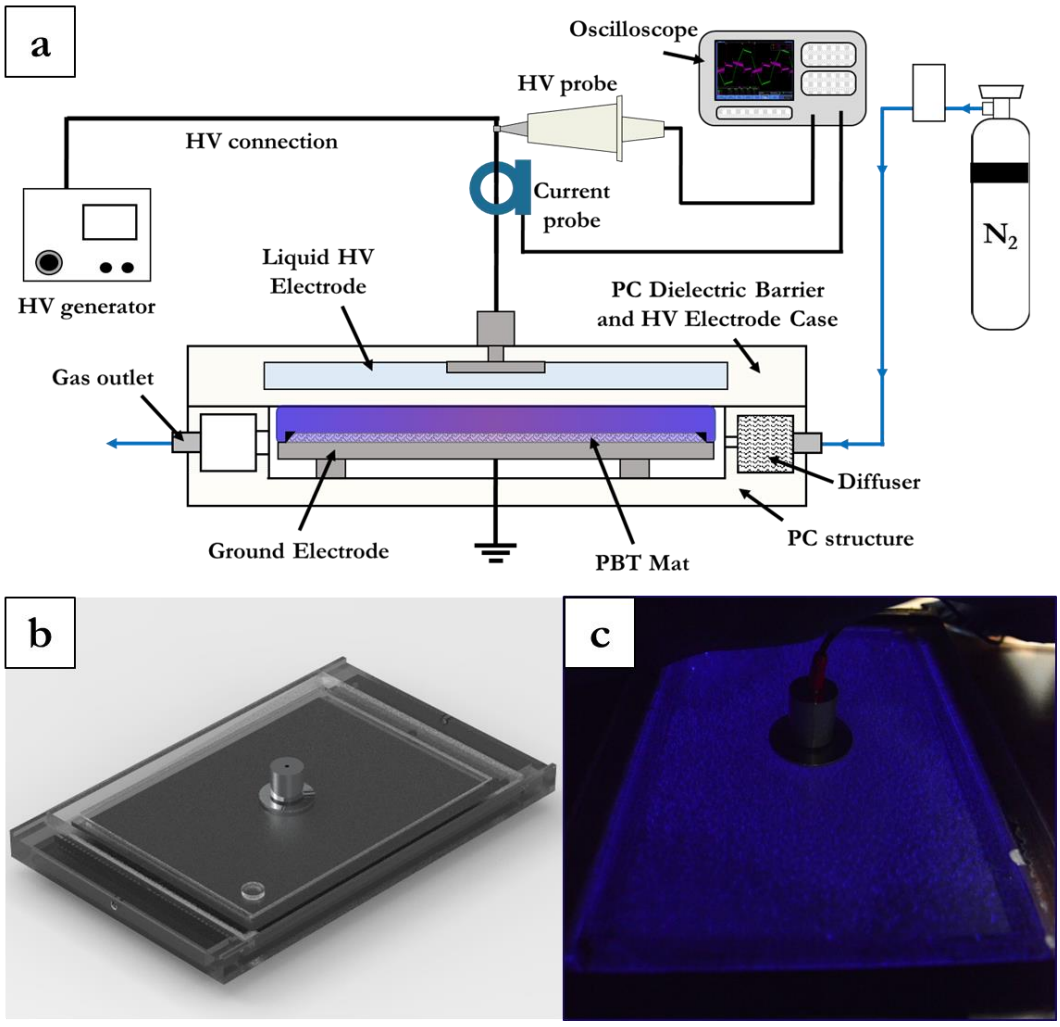

Figure 2.1. Experimental setup for the treatment of PBT mats (a); a rendering of the plasma source (b) and a picture of the operating DBD source (c) where uniformly distributed microdischarges can be observed.

At the end of the treatment the sample is removed from the ground electrode and then characterized.

Attenuated Total Reflectance-Fourier Transform Infrared (ATR-FTIR) spectroscopy was employed to study the chemical structure of the untreated and treated PBT mats. The spectrometer (Agilent Cary 660 FTIR spectrophotometer) was equipped with an ATR sampling accessory, using a diamond crystal as internal reflection element. Spectra were acquired at RT in absorbance mode, from 4000 to 400 cm^{-1} with a resolution of 2 cm^{-1} and a total of 32 scans for each spectrum.

Similarly, SEM imaging (Phenom ProX SEM) was employed to evaluate the effect of plasma treatment on the morphology of the samples. During the characterization, an accelerating voltage of 15 kV was applied on the samples which were previously sputter coated with gold.

The wettability of untreated and plasma-treated samples was evaluated by measuring the time required by 3 drops (2 μl) of a saline solution (distilled water + NaCl 10 w%) to be completely absorbed in the samples once deposited. Furthermore, a preliminary analysis of the treatment stability was performed by subjecting smaller treated samples (100 x 100 mm^2) placed inside autoclave pouches to steam-sterilization at 121°C for 20 min (LABO1, Newmed srl). Once sterilized, the samples were dried for 48 hours at 40°C and wettability of the samples was measured again.

2.2.2.2. Results and Discussion

The average value of the volumetric power density was calculated from the voltage and current waveforms acquired during the treatment (shown in Figure 2.2), resulting to be around 0.75 W/cm^3. Several short intense current peaks are present during the positive and negative half-cycles, thus confirming that the DBD source is operating in a filamentary regime and not in a glow-discharge regime, as can be observed also in Figure 2.1c. According to several studies [20,31–33], at atmospheric pressure this regime can be associated by high power operating conditions or by the presence of oxygen and other impurities.

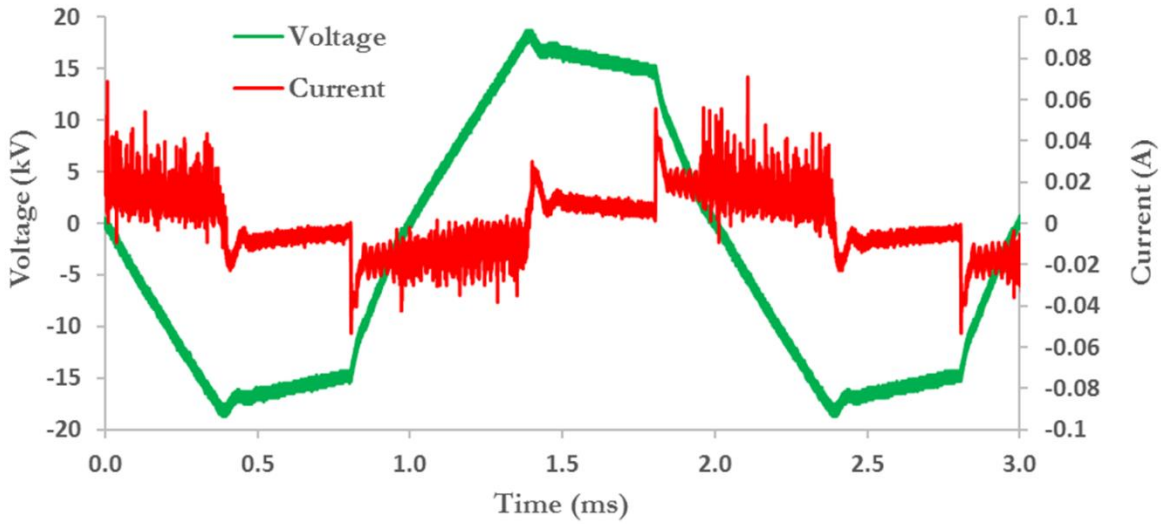

Figure 2.2. Voltage and current waveforms obtained from the DBD plasma source.

Concerning the surface chemistry of PBT mats, no plasma-induced modifications were detected from the IR-spectra (Figure 2.3). This result can be explained by the fact that only the outermost surface layers of the material (few nanometers) are affected by the plasma functionalization when non-polymerizable gases are used for the process, as reported elsewhere [34]; therefore the substrates' thickness modified by the treatment is much lower than the characteristic sampling depth of ATR-FTIR, which is around ~1 μm [35].

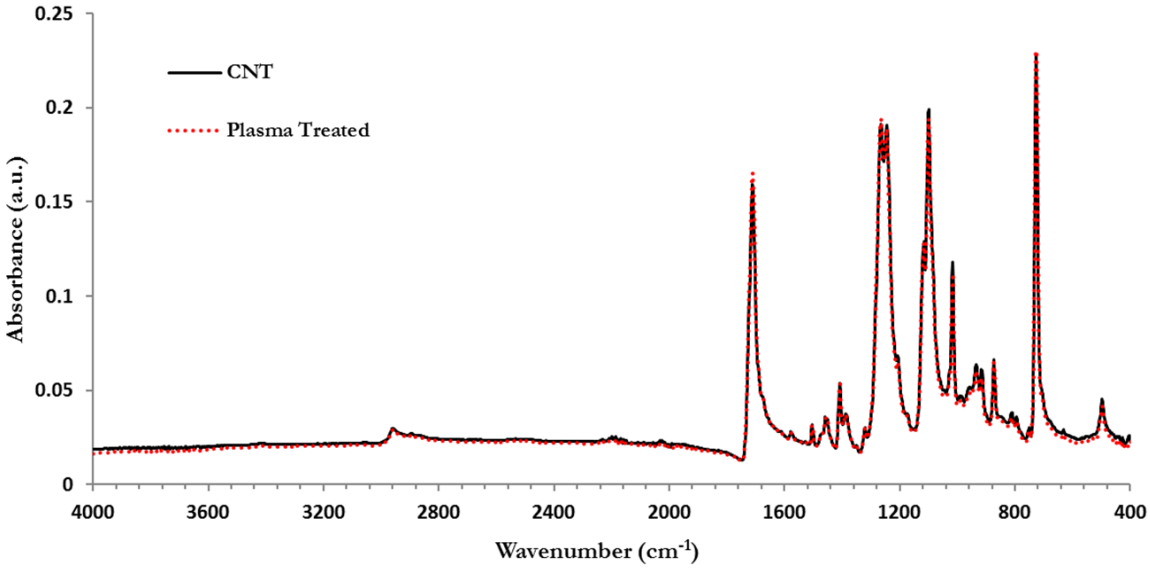

Figure 2.3. IR spectra of untreated PBT mats (CNT) and plasma-treated ones.

Images obtained from SEM (Figure 2.4) reveal that the plasma treatment didn't affect the morphology of the PBT fibres of the mats, even if the DBD source was operating in a filamentary regime and the mats were directly placed on the grounded metal surface; this configuration has been demonstrated could possibly damage polymeric materials for long treatment times due to the localized energy transfer of the microdischarges [29].

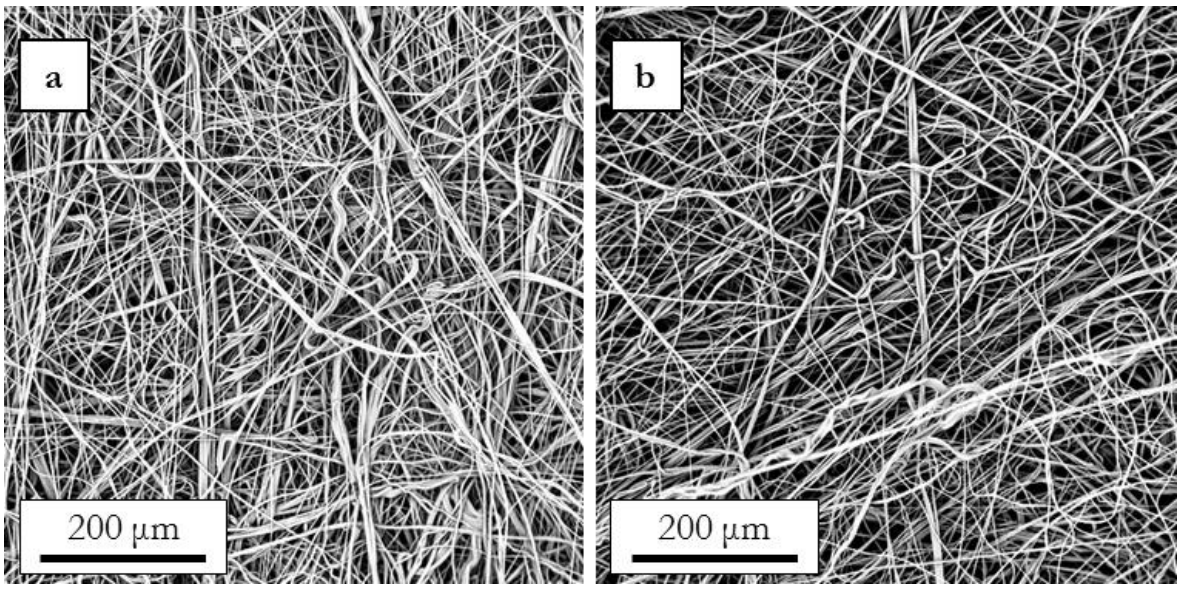

Figure 2.4. SEM images of the fibres of untreated (a) and plasma treated (b) PBT mats.

Although no significant differences were detected between untreated and treated samples from the IR spectra and the SEM images, the wettability tests highlighted two completely different behaviours. As shown in Figure 2.5, the drops deposited on nitrogen plasma treated PBT mats are absorbed almost immediately (Figure 2.5a), while no absorption can be observed for the untreated mats even several minutes after the drop deposition (Figure 2.5b). Unexpectedly, the treated samples are still hydrophilic after the sterilization and drying process, as can be observed in Figure 2.5c, whereas a strong hydrophobic recovery usually occurs when plasma-functionalized polymers are exposed to water vapour or after storage in air at temperatures higher than room temperature [36,37]. This result may be of interest for several biomedical applications where long-term stability of the surface hydrophilicity is required. However, further investigations are necessary to evaluate whether the retention of the hydrophilicity may be the effect of the samples' degradation. Indeed, it has been reported that steam-sterilization can induce the degradation of polyesters, although PBT is more stable to such sterilization technique with respect to other polyesters [1].

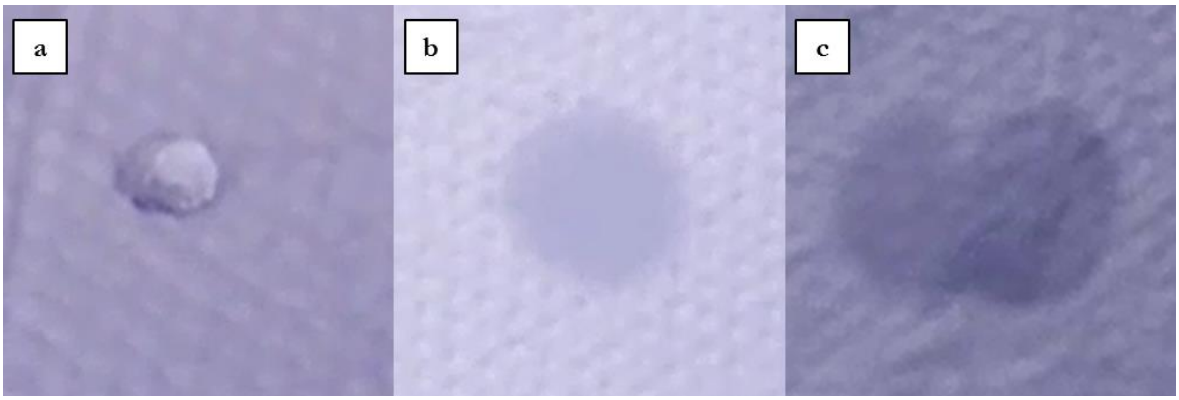

Figure 2.5. Wettability tests on PBT mats: stable water drop on the untreated sample (a), darker areas related to the absorption of the drops in the as-treated sample (b) and in the sterilized and dried sample (c).

2.2.3. Development of a Plasma Prototype System for In-line Treatment of Polymeric Films

To evaluate the industrial feasibility of the studied plasma-assisted processes, a plasma prototype system for in-line treatment of polymeric foils was developed, as shown in Figure 2.6. This system includes most of the components already presented in the experimental setup of Fig. 2.1, such as the manual flow controller, a dielectric barrier discharge plasma source and a high voltage generator, although some changes were made to adapt that configuration to an in-line treatment process.

A customized version of Alma*PULSE* (AlmaPlasma s.r.l.) was selected as HV generator for its versatility in enabling to control the frequency, PV and duty cycle of the applied voltage and consequently the characteristics of the plasma discharge. Furthermore, the capacity of this generator to sustain high volumetric density powers (up to 7 W/cm^3 for the large area DBD source presented before) make it suitable for in-line treatment of polymeric materials.

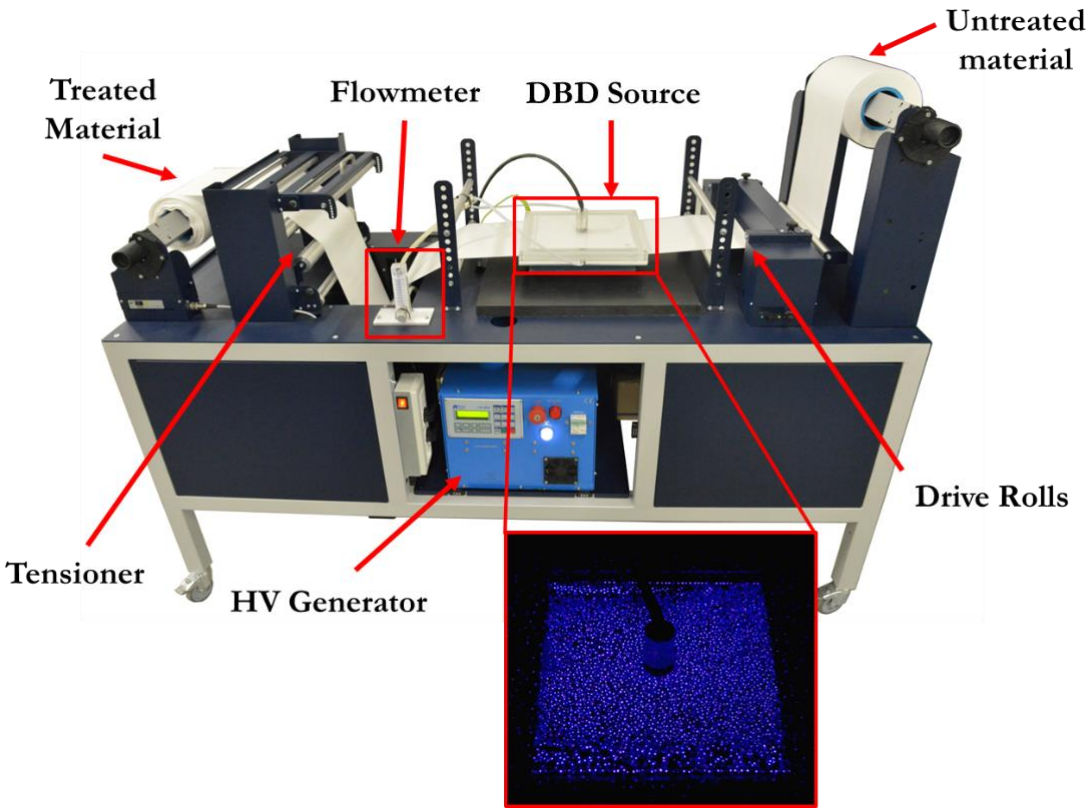

Figure 2.6. Picture of the Roll-to-Roll system developed for in-line plasma treatment of polymeric films and detail of the DBD plasma source processing a polymeric film.

Even if some geometrical characteristics and materials of the DBD source were almost unmodified with respect to the one employed in section 2.2.2.1 (discharge volume, the use of a liquid HV electrode with a polymeric dielectric barrier, the use of a ground electrode made of aluminium), a DBD source was realized according to a design suitable for in-line processing of films, as represented in Figure 2.7. In particular, a different configuration of the gas inlets and gas outlets was designed in order to grant some degree of control on the composition of the atmosphere inside the discharge volume. Indeed, the gas inlets are placed in the centre of the lateral walls of the source, thus allowing to inject the desired gas in the midst of the source. From the centre of the source the gas flows towards the small gaps separating the Polytetrafluoroethylene (PTFE) bars, which define the film transition area. This configuration makes possible to fairly efficiently remove the air inside the plasma source and keep some control on the gas composition of the discharge by employing contained gas flow rates. Furthermore, the low friction coefficient of PTFE makes easier the films to pass through the plasma source. Both the realized DBD plasma source and HV generator, together with a flow meter, were properly assembled in a Roll-to-Roll system, thus allowing to treat polymeric

materials at high speed (up to 10 m/min) in a controlled atmosphere and study the functionalization process on a preindustrial scale.

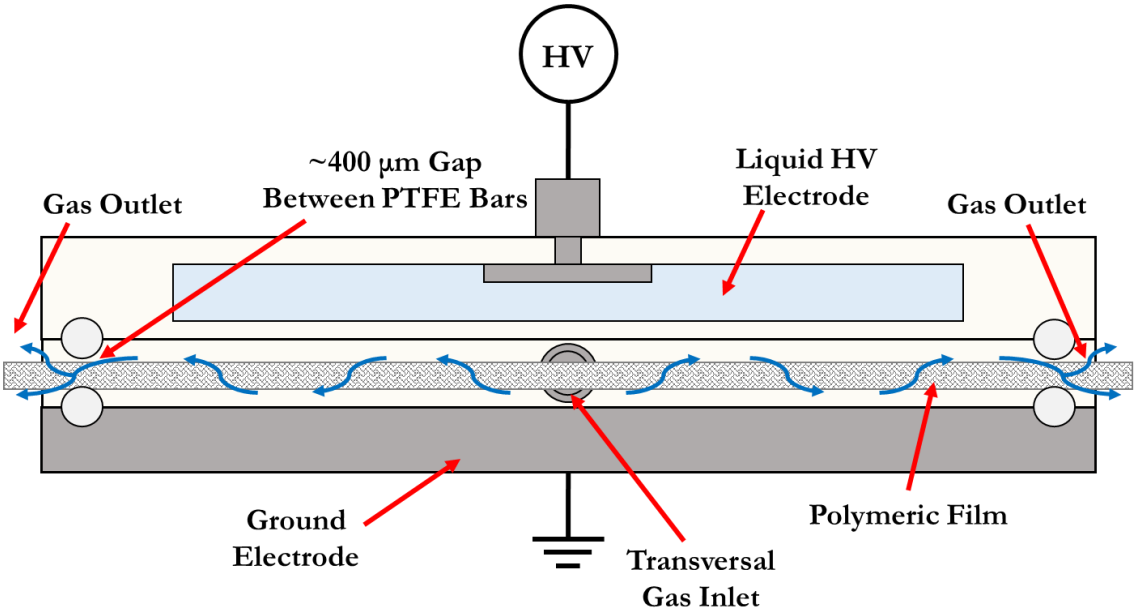

Figure 2.7. Scheme of the DBD source designed for in-line treatment of polymeric materials, with details on the arrangement for the gas distribution.

2.2.4. Conclusions

In this chapter the results achieved on the study of the potentialities of plasma functionalization to increase the hydrophilicity of PBT mats and the following development of a plasma prototype system for in-line treatment of polymeric materials were presented.

A large-area (~600 cm^2) DBD plasma source was operated at atmospheric pressure in a static configuration to confer hydrophilic properties to PBT mats. The plasma filamentary discharge, generated in nitrogen, has been demonstrated to be effective in increasing the wettability of the polymeric samples without affecting their morphology, as it could be expected from the observed filamentary discharge regime. Furthermore, plasma treated samples turned out to be still hydrophilic after being sterilized and dried. However, further investigations must be carried out to fully comprehend the evolution of the surface chemistry and morphology of samples during the different steps presented. For example, although there was no opportunity to use X-ray Photoelectron Spectroscopy (XPS) during the reported activities, this analytical technique should be employed to understand whether they are nitrogen, hydroxyl or other functional groups that induce the change in the wettability of the polymeric material and to evaluate the

effects of the steam-sterilization process on the wettability and chemical structure of the PBT mats.

In order to perform an industrial-oriented investigation of this process in a more realistic setup, a plasma prototype Roll-to-Roll system was developed to enable in-line treatment of polymeric films. This system was designed and realized in such a way to ensure the possibility to control the gas composition and the power conferred to the plasma discharge; the system represents therefore a flexible instrument to perform preindustrial studies aimed at the investigation of the potentialities of plasma-functionalization.

2.3. Reduction of the Wettability of Natural Textiles by means of Cold Atmospheric Pressure Plasma Sources

2.3.1. Introduction

The interest of the textile industry for plasma treatments has increased in the last years mainly due to the growing request for green, sustainable and cost-competitive processes to replace the conventional wet chemical ones during the different phases of textiles production (preparation, colouration and finishing). In particular, CAP sources have become important in the last decade as they can be "easily" implemented in already existing production lines and they present lower capital and running costs with respect to low pressure ones [8,12,38–41].

Among their possible applications in textile industry, CAP sources can be employed to increase the hydrophobicity of natural textile fibres, thus obtaining waterproof fabrics, preserving at the same time their original characteristics such as water vapour permeability, which is fundamental for the comfort of the garments [38,41]. This process leads to the introduction of hydrophobic functional groups, *e.g.* fluorine and silane, at the surface of the textile fibres and it can be performed in different ways, such as plasma-assisted polymerization of a monomer or polymerizing gas (single-step processes) and plasma-grafting techniques (two steps processes)

[38]. Several studies have been performed on this topic, both on natural and synthetic fabrics, using low pressure [42–65] and atmospheric pressure cold plasmas [66–73]. However, so far only a single work has been published on the plasma-hydrophobization of single yarns or threads [50], which would be an interesting solution for industry as it allows to keep the higher flexibility of threads with respect to fabrics and to avoid shadowing effects [10,12]. Another fundamental issue to be considered is the scalability of the plasma sources and processes to the industrial level: usually textiles production requires winding speeds of the yarns in the order of hundreds of m/min, therefore plasma treatment has to be effective at similar speeds or it could be not implementable or economically sustainable.

In this chapter, the study to realize an industrial prototype system for the plasma-assisted hydrophobization of cotton threads using a fluorinated gas at atmospheric pressure as precursor is reported. The first part of the chapter is focused on the treatment of cotton fabrics using an APPJ in a static configuration and on the characterization of the treated samples, which assessed the feasibility of the process. As a second step, a lab-scale winding system was realized in order to study the effectiveness of the APPJ for the treatment of materials in a dynamic configuration. As the treatment resulted ineffective at high winding speeds of the threads, in the last part of this chapter a more advanced prototype plasma source is designed and realized, and the preliminary results achieved using this source are presented.

2.3.2. Preliminary Study on the Plasma-Assisted Hydrophobization of Cotton Fabrics Using an APPJ in a Static Configuration

2.3.2.1. Materials and Methods

A preliminary study in a static configuration was performed to assess the feasibility of the hydrophobization processes by means of an APPJ, as shown in Figure 2.8. The plasma source employed is a single electrode dual gas plasma jet developed in our laboratory and reported in several previous works [74–78], in which more information on its characteristics can be found. The APPJ was driven by the HV pulse generator Alma*PULSE* (AlmaPlasma s.r.l.), operated at 18 kV, 20 kHz. A mixture of Ar (99,999%) and Octafluorocyclobutane (C_4F_8, 99,99%), whose composition was controlled by means of two flowmeters set at 3.7 slpm and 0.24 slpm respectively, was introduced into the plasma source through the primary gas channel [77,78]. 100% cotton fabrics with a dimension of 40 mm x 40 mm were used as samples and placed on

a 2 mm thick ceramic sheet (mica, muscovite), covering a floating electrode obtained from an aluminium foil. The distance between the plasma source and the dielectric surface was kept constant at 2 mm. Ar and C_4F_8 were flushed for at least 1 minute before igniting the plasma discharge thus removing the air contained in the plasma source and the gas connections. Two treatment times, 60 s and 120 s, were studied.

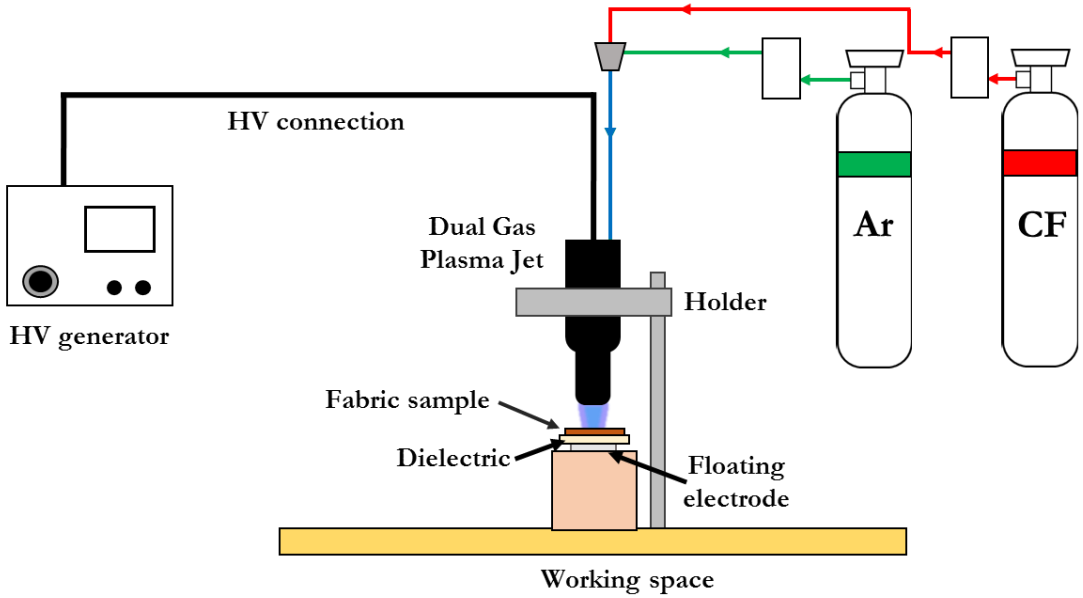

Figure 2.8. Experimental setup adopted for the hydrophobization process using an APPJ in a static configuration.

WCA measurements were performed to evaluate the wettability of the cotton fabrics before and after the plasma treatment. Measurements were carried out at room temperature using a commercial Kruss Drop Shape Analysis System DSA 30 and its software to evaluate the static contact angles. Sessile drop method was employed, using distilled water drops with a defined volume of 2 μl.

ATR-FTIR spectroscopy was used to characterize the chemical structure of the cotton fabrics before and after the plasma treatment. The spectrometer (Agilent Cary 660 FTIR spectrophotometer) was equipped with an ATR sampling accessory, using a diamond crystal as internal reflection element. Spectra were acquired at RT in absorbance mode, from 4000 to 400 cm^{-1} with a resolution of 2 cm^{-1} and a total of 32 scans for each spectrum.

SEM imaging was employed to study the effects of the treatment on the morphology of the samples, analysing the untreated samples and the samples treated for 120 s. The analysis was performed using a Phenom ProX SEM by applying an accelerating voltage of 10 kV on the samples after being sputter coated with gold. The same instrument was used to perform Energy

Dispersive X-ray Spectroscopy (EDS) to obtain more information on the chemical characteristics of the materials.

2.3.2.2. Results and Discussion

The treated area resulted in a circular spot with a diameter of approximately 4÷5 mm. WCA was impossible to be measured for both untreated and treated samples: it cannot be evaluated for the untreated cotton fabrics since the drops were absorbed immediately once deposited, while it cannot be evaluated for treated samples since the drops can't be deposited on the treated area, due to the high hydrophobicity of the substrate. These results highlighted that superhydrophobicity was achieved on the treated fabrics also for the shortest tested treatment time, as shown by the successive picture frames in Figure 2.9. Furthermore, the treated area results to be "non-sticky" as the water drops immediately slip on it once tilted. The same characteristics can be observed in the samples after storage in ambient air for one month, thus assessing that the treatment is not strongly affected by ageing phenomena.

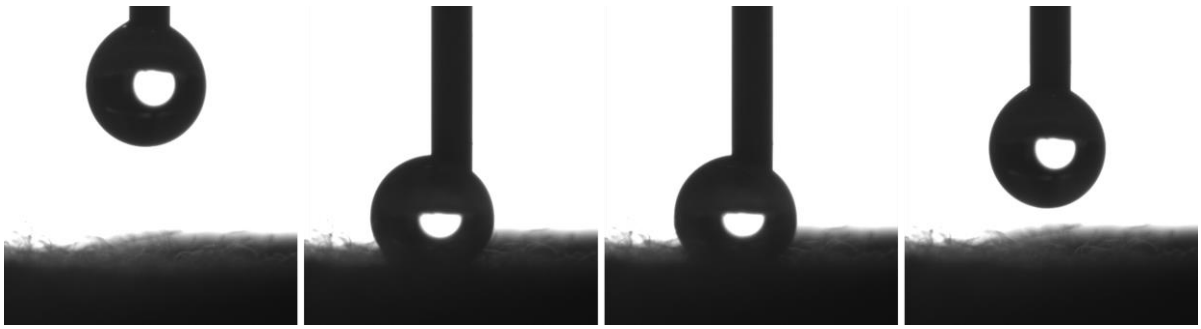

Figure 2.9. Frames of a water droplet approaching and being withdrawn from the super-hydrophobic cotton fabric (treatment time 60 s).

In Figure 2.10a the spectra of the untreated cotton fabrics and plasma treated fabrics for 60 s and 120 s are reported. The effects of the plasma treatment are clearly visible in two regions: the broad band region of OH stretching (3600-3000 cm^{-1}) [79,80] and in the region at 1300-1000 cm^{-1}, which is attributed to fluorine groups [79–81]. Furthermore, the peaks at 1200 cm^{-1} and 1150 cm^{-1}, corresponding to the asymmetric and symmetric CF stretching vibrations respectively [54,55], are clearly detectable. The reduction of OH groups and the increase of fluorine groups observed after the plasma treatment can be easily related to the

superhydrophobic behaviour of the treated fabrics; this effect is mainly due to fragmentation of the C_4F_8 in smaller radicals, such as CF, CF_2, CF_3, F, and their deposition on the substrate forming fluorine-rich coatings usually consisting of nanometric particles/islands [82,83]. Indeed, longer treatment times induce an increase of the absorbance in the region associated to fluorine groups (clearly visible in Figure 2.10b), which could be related to an increase of the thickness of the deposited coating.

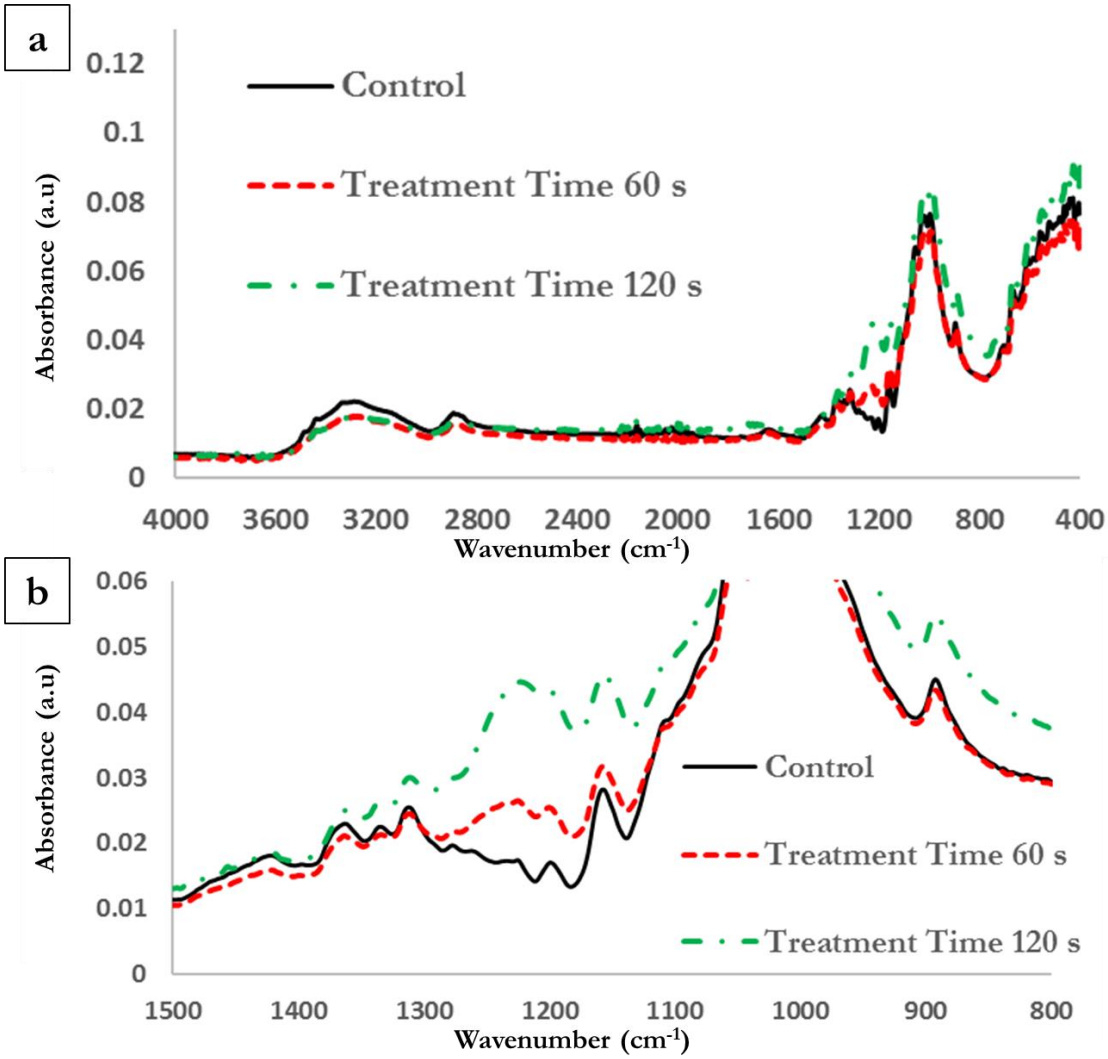

Figure 2.10. IR spectra obtained from untreated and plasma treated cotton samples: overall spectra (a) and detail of the spectra in the region characteristic of fluorine groups (b).

The morphology of the samples is shown in Figure 2.11: for the lowest magnifications no differences can be observed in the structure of the fabrics between the untreated and plasma treated samples (Figure 2.11a and Figure 2.11b), while for higher magnifications a coating can be seen on the treated samples (Figure 2.11d and Figure 2.11f). Indeed, the coating is characterized by small cracks transversal to the fibres orientation and by few sub-micrometric

particles (Figure 2.11f), which can't be observed in untreated samples (Figure 2.11c and Figure 2.11e). Differently from the works of Milella *et al.* [82] and Han and Moon [83] it was impossible to observe nanoislands on the surface of the treated samples. However, we can reasonably assume that in this case the coating is very smooth or characterized by very small nanometric structures, undetectable to the SEM: indeed, the uniform distribution of elemental fluorine on the treated surfaces was confirmed by the results obtained from EDS spectra, shown in Figure 2.12.

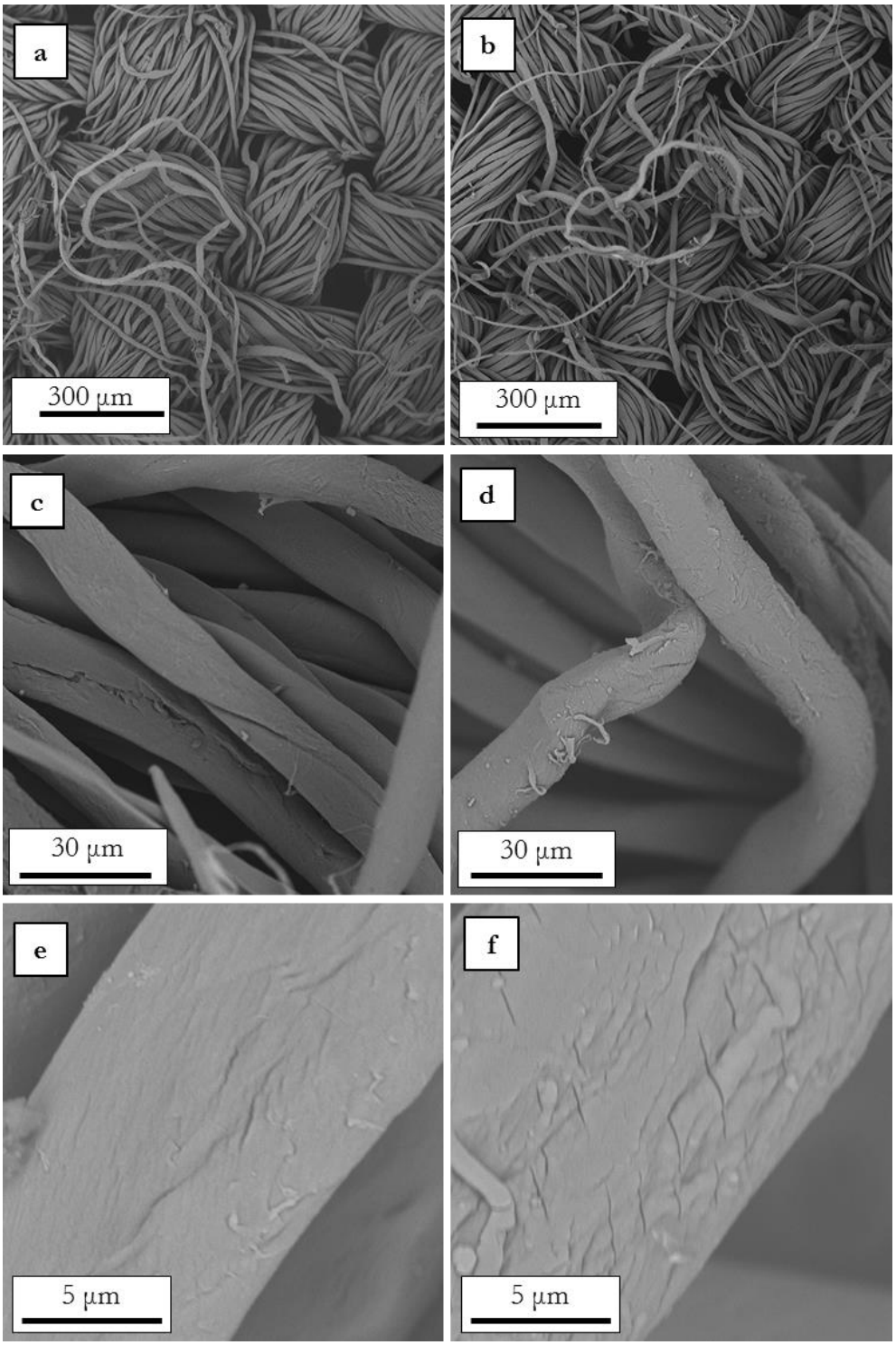

Figure 2.11. SEM images obtained from untreated (a, c, e) and plasma-treated (b, d, f) cotton fabrics at different magnifications. Cracks and sub-micrometric particles on the surface of the coating can be observed at high magnifications (d, f) for the treated fibres with respect to the untreated ones (c, e).

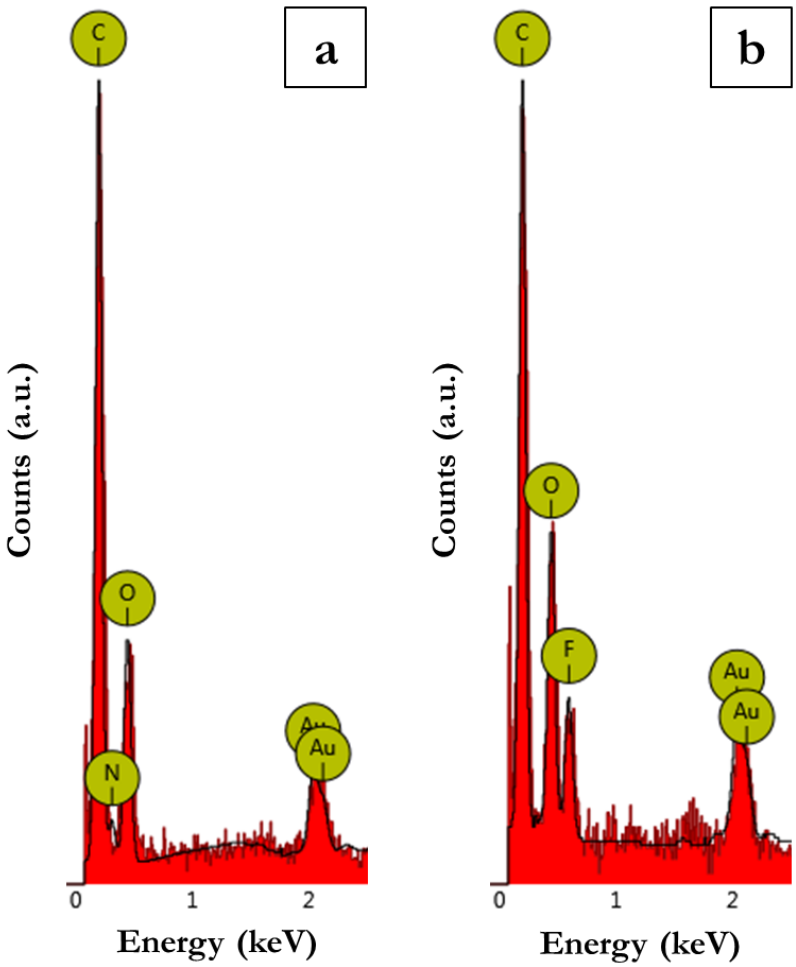

Figure 2.12. Region of the EDS spectra obtained for the untreated cotton sample (a) and for the plasma treated one containing fluorine (b).

Based on these promising results, the setup was modified in order to perform the same hydrophobization process on cotton yarns in a dynamic configuration.

2.3.3. Plasma-Assisted Hydrophobization of Cotton Threads Using an APPJ in a Dynamic Configuration

2.3.3.1. Materials and Methods

A winding system was realized to perform the plasma-hydrophobization process on threads in a dynamic configuration, as shown in Figure 2.13. The winding systems consist of a removable spool mounted on shaft moved by a DC brushless motor, whose velocity can be controlled in the range 0÷250 m/min by means of a driver and a shaft encoder. The thread (cotton, Gunze

count #20/2) is drawn from a tapered cone passing through a tensioner and some pigtail thread guides, which ensures that the thread passes correctly in the plasma discharge region at a fixed height of 1 mm above the dielectric surface. The rest of the setup is kept the same with respect to the one presented in section 2.3.2.1. Except for the PV that was increased to 20 kV, the operating conditions were not changed with respect to the ones previously employed and, two winding velocities were studied, 1 m/min and 10 m/min.

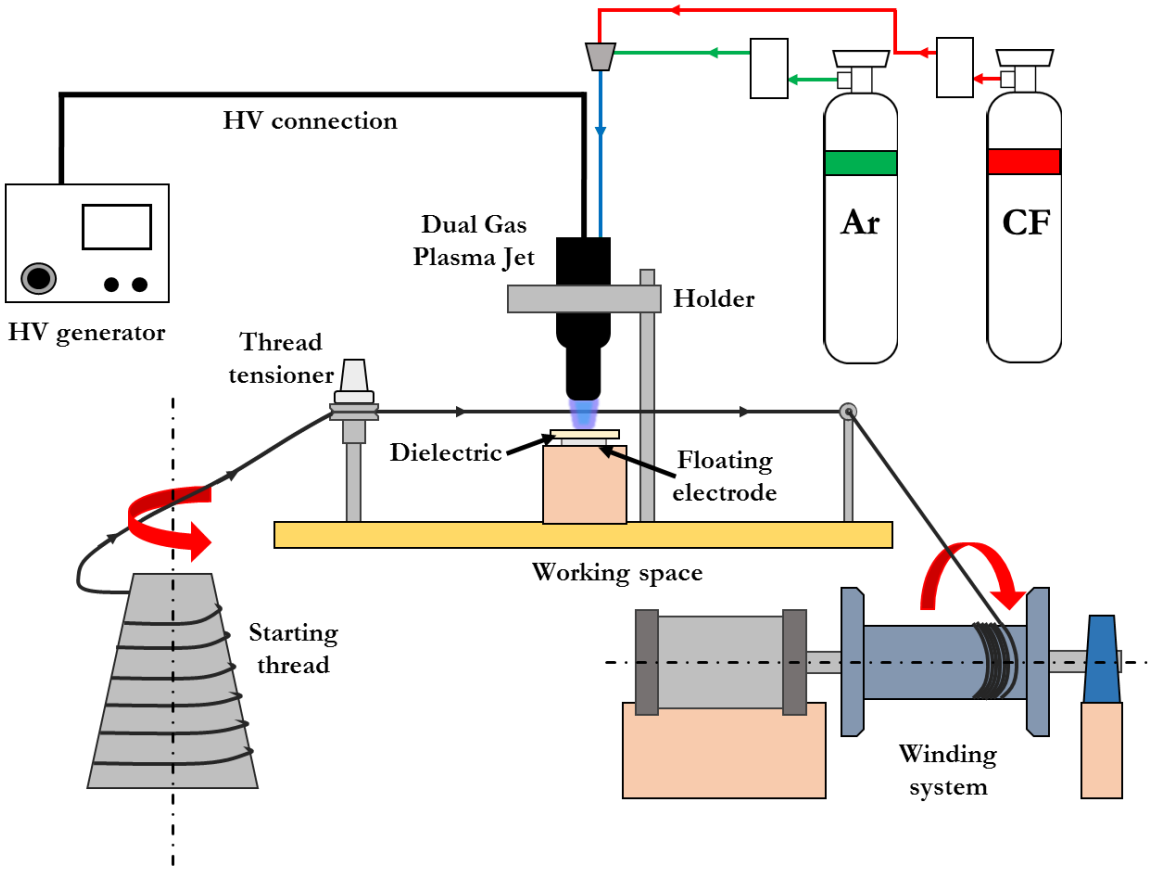

Figure 2.13. Experimental setup adopted to perform the hydrophobization process using an APPJ in a dynamic configuration.

To characterize the treated and untreated threads small mats were realized manually, winding the threads around glass substrates. Three drops (2 μl) of distilled water were deposited on the obtained samples to evaluate the mean absorption time of the mats, as shown in Figure 2.14; for due to the surface irregularity of these mats contact angle measurements could be characterized by a high uncertainty. The time required for the absorption of the drops was measured up to a maximum of 45 minutes, as for longer times evaporation could be the main mechanism inducing the shrinkage and disappearance of the drops.

ATR-FTIR spectroscopy was used to characterize the chemical structure of the untreated cotton threads and plasma treated ones, employing the operating parameters of the spectrophotometer as previously described.

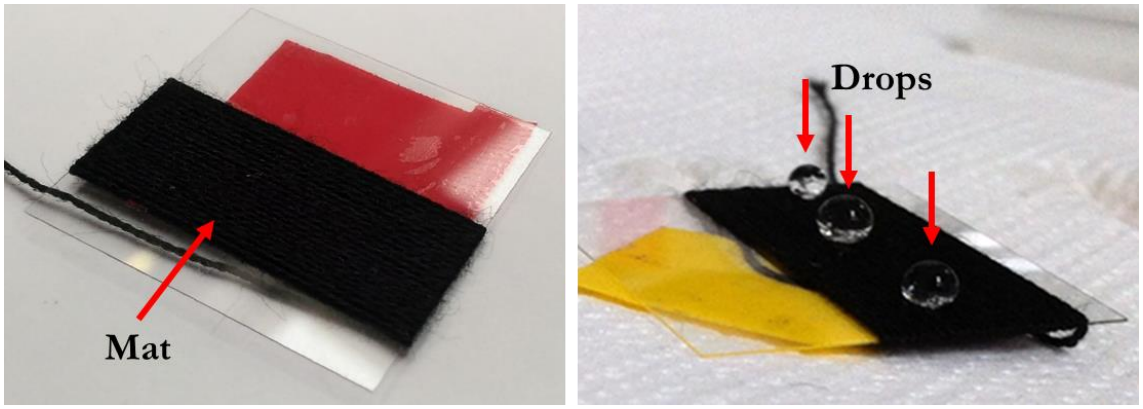

Figure 2.14. Mats prepared from the untreated and plasma-treated threads: sample as prepared on glass substrates (left); drops deposited on a mat to evaluate its hydrophobicity (right).

2.3.3.2. Results and Discussion

The mean values and standard deviations of the absorption times for the mats prepared from the untreated and plasma-treated threads are reported in Table 2.1. The drops were absorbed in a short time once deposited on the untreated samples, even if not immediately as occurring for cotton fabrics. At the lowest winding speed (1 m/min) the treatment was demonstrated to be effective as a strong increase in the mean value of the absorption time is observed despite of the high standard deviation, probably due to a lack of uniformity of the treatment. At the winding speed of 10 m/min the samples present the same absorption times of the untreated ones. It is possible that at high winding speeds the thickness of the deposited coating is not sufficient to properly cover the surface of the fibres due to the short residence time of the material in the plasma plume (evaluated to be around 0.02 s).

This consideration is confirmed by the IR-spectra of the untreated and treated cotton fibres, which resulted to be coincident (and therefore they are not reported). Considering that the characteristic spectrum of cotton is still visible also for long treatment times (as shown in Figure 2.10), it can be reasonably assumed that the coating deposited for high winding speeds is significantly lower than the sampling depth of ATR-FTIR spectroscopy. Furthermore, we can expect that the coating is not completely covering the fibres and therefore no significant change

in the wettability of the material can be detected at the macroscopic scale after the plasma process.

Table 2.1. Absorption times for mats prepared from untreated and plasma-treated cotton threads using the APPJ.

Winding speed [m/min]	**Absorption time [min sec]**
Untreated	1’45’’ ± 29’’
1	26’35’’ ± 10’13’’
10	1’47’’ ± 35’’

This issue highlights the need to increase the treatment time for high winding speeds to obtain a reliable hydrophobic surface, therefore a plasma source was expressly designed for this purpose.

2.3.4. Design and Preliminary Tests of a DBD Plasma Source for the Plasma-Assisted Hydrophobization of Cotton Threads in a Dynamic Configuration

2.3.4.1. Materials and Methods

A volumetric DBD plasma source, shown in Figure 2.15, was designed and realized to increase the residence time of the cotton threads inside the plasma region at high winding speeds.
The main body of the source is a Polymethyl methacrylate (PMMA) carved structure, working both as dielectric barrier, with a thickness of 5 mm, and as container for the HV liquid electrode. This structure is fastened to the ground electrode, made of aluminium and presenting a channel for the working gas (gas inlet of the source) and a separated internal channel fed by compressed air, used as cooling system of the electrode. When the PMMA structure and the ground electrode are fastened together the discharge volume (2 mm height x 12 mm width x 200 mm length) is formed. The geometry of the gas inlet and the exhausts, which are laterally placed in the source as shown in Figure 2.15, are designed to ensure that air is removed from the source once the operating gases are flushed.

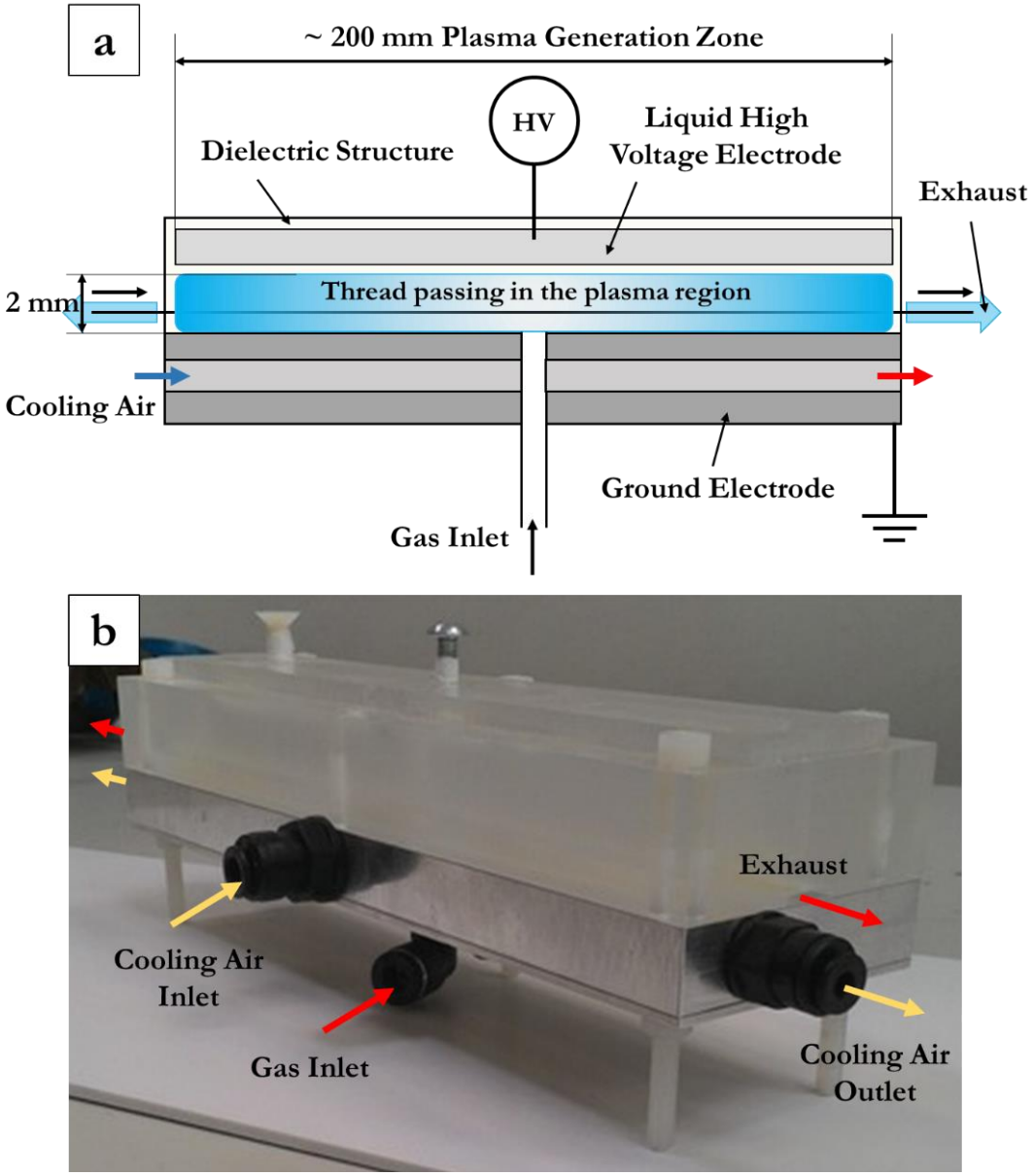

Figure 2.15. Schematic (a) and picture (b) of the DBD plasma source designed and realized for the treatment of threads at high speeds.

The DBD source was employed in the setup previously described (section 2.3.3.1) replacing the APPJ, as shown in Figure 2.16. The thread is forced to pass 1 mm above the ground electrode in the centre of the discharge volume by means of the thread tensioner and of the pigtail thread guides. The flow rates of Ar and C_4F_8 were set to 3.7 slpm and 0.6 slpm, respectively, for all the tests. As previously described, the gas mixture was flushed for at least 1 minute before igniting the plasma discharge thus removing the air contained in the plasma source and in the gas connections. The HV generator employed was a customized version of

Alma*PULSE* (AlmaPlasma s.r.l.). The electrical operating conditions and the thread speeds studied are presented in Table 2.2.

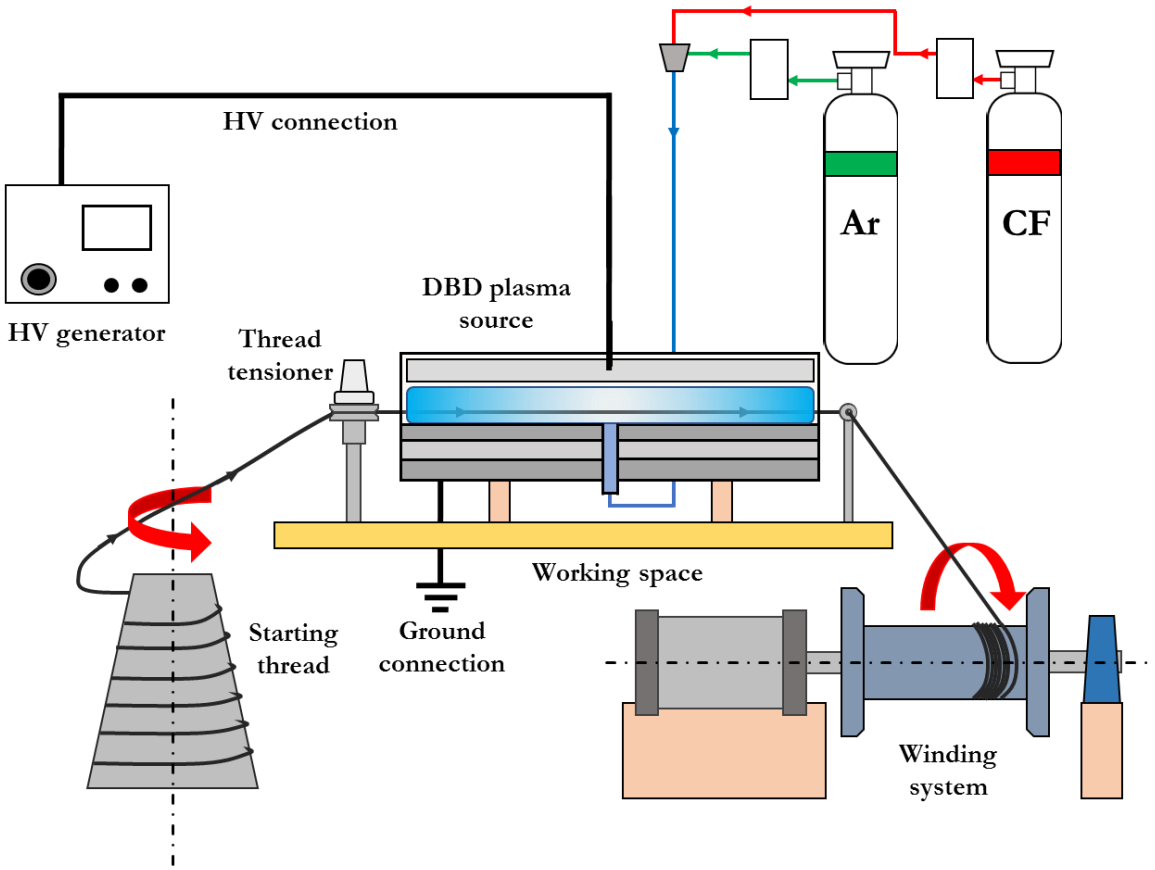

Figure 2.16. Experimental setup adopted to perform the hydrophobiation process using the DBD plasma source in a dynamic configuration.

Table 2.2. Investigated operating conditions for the DBD plasma source.

Operating condition	**PV [kV]**	**Frequency [kHz]**	**Duty Cycle [T_{on} ms/T_{off} ms]**	**Power [W]**	**Thread Speed [m/min]**
A	20	14	8/2	75	10
B	20	14	8/2	75	20
C	22.5	14	8/2	87	10

The characterization of the thread was performed according to the methods described in section 2.3.3.1, evaluating the absorption time of drops of distilled water deposited on mats prepared from the threads and the IR-spectra of the mats.

2.3.4.2. Results and Discussion

The mean values and standard deviations of the samples prepared for the different operating conditions previously described are reported in Table 2.3.

Table 2.3. Absorption times for mats prepared from untreated and plasma-treated cotton threads using the DBD source.

Operating condition	**Absorption time [min sec]**
Untreated	1’48’’ ± 28’’
A*	34’47’’ ± 14’30’’
B	7’27’’ ± 1’26’’
C*	41’01’’ ± 4’11’’

*= some drops required more than 45 minutes to be absorbed

For all the tested operating conditions an increase of the hydrophobicity of the samples is observed, even if it is very limited for the highest thread speed tested (20 m/min). Long absorption times are obtained for both conditions A and C (same thread speed, 10 m/min), however the threads treated in condition C present a smaller standard deviation with respect to the ones treated in condition A. While all the drops deposited on mats obtained from threads treated in condition C are characterized by long absorption times (>34 minutes), some drops obtained from the threads treated in condition A present very short absorption times (~10 minutes). This effect could be related to a lack of uniformity in the treatment caused by a lower deposition rate for condition A with respect to condition C, the latter characterized by a higher operating power. The influence of the power on the deposition rate can be assumed to be governed by the parameter defined by Yasuda W/FM (W is the discharge power, F the precursor flow rate, M its molecular weight) and the behaviour observed during the tests is characteristic of a polymerization performed in the “monomer sufficient region” (or “energy deficient region”) [84,85]. Indeed, if the plasma discharge is operating in this region, the increase of the parameter W/FM leads to an increase in the deposition rate, since there is a sufficient amount of monomer in the discharge atmosphere to be further activated and deposited. Therefore, we can expect that for higher operating powers (and so, higher deposition rates) all the surface of the thread is covered by the fluorine compounds even if the thickness of the coating could be less than uniform along it.

For all the three cases, the coatings resulted too thin to be detected by ATR-FTIR spectroscopy since no differences were observed between the IR spectra of the untreated and treated threads, as noticed in section 2.3.3.2.

Furthermore, the progressive formation of a thin Teflon-like film on the surface of the grounded electrode and on dielectric barrier one was observed in all the investigated cases. Even if the presence of the deposited film didn't sensibly affect the process during the tests, its growth could be a relevant issue in industrial applications in which the plasma sources have to run continuously for several hours or days. A possible solution to this issue could be the development of modular plasma sources operating in parallel and/or the development of sources with replaceable electrode and dielectric barrier. Moreover, the measurement of the voltage signal applied to the source can be performed to define the maintenance time for the single plasma source or its components, setting a threshold value of the PV below which they will have to be cleaned or replaced. All these technical solutions, once implemented in the source presented above, will provide us a reliable system to perform the process on an industrial scale.

2.3.5. Conclusions

In this chapter, the development of a system for the plasma-assisted hydrophobization of cotton threads in a dynamic configuration was presented. A preliminary study was carried out to evaluate the feasibility of the process: cotton fabrics were treated in a static configuration using an APPJ and C_4F_8 as precursor. The treated zone of the fabrics became superhydrophobic after the treatment showing also a non-sticky behaviour. The morphology of fibres resulted almost unaffected by the plasma treatment but the presence of an organofluorine coating was clearly assessed by means of ATR-FTIR and EDS.

Then the experimental setup was modified in order to make possible the treatment of cotton threads in a dynamic configuration. The absorption time of mats obtained from the untreated and treated threads was evaluated: for a speed of the thread of 1 m/min the treatment was effective increasing the absorption time of the samples (mean value 26'35'') with respect to natural cotton (mean value 1'45''), however at 10 m/min the treatment didn't modify the wettability of the yarns. This effect can be related to the short residence time of the threads in the plasma discharge.

To increase the residence time of the threads in the plasma discharge zone a DBD plasma source, whose length of the plasma generation volume is 200 mm, was designed, realized and

preliminary tested in different operating conditions. With this source a strong increase of the hydrophobicity was obtained for threads winded at 10 m/min (mean value >30') and a slight increase was obtained at 20 m/min (mean value 7'27''), however it can be supposed that the coating is not fully uniform over the fibres except for high operating powers.

The DBD source proved to be effective to treat the cotton threads also at high speeds, however further improvements are demanded to optimize the deposition process and to obtain more hydrophobic and uniform coatings; new operating conditions and new geometries of the setup require to be studied and investigated. The next step will be probably devoted to modify the setup so that the thread can pass several times inside the plasma discharge region before being collected on the winding spool. This change will improve the residence time of the thread in the DBD volume at a fixed winding speed without modifying the other parameters. Furthermore, new chemical, morphological and mechanical analysis will be performed on the threads in order to better understand the surface chemistry and mechanical characteristics induced by the plasma treatment.

References

[1]. V. R. Sastri, *Plastics in Medicals Devices: Properties, Requirements and Applications*, 2nd ed. (William Andrew, 2013).

[2]. P. K. Chu, J. Y. Chen, L. P. Wang, and N. Huang, Mater. Sci. Eng. R Reports **36**, 143 (2002).

[3]. G. Fourche, Polym. Eng. Sci. **35**, 968 (1995).

[4]. A. S. Hoffman, Macromol. Symp. **101**, 443 (1996).

[5]. T. Desmet, R. Morent, N. De Geyter, C. Leys, E. Schacht, and P. Dubruel, Biomacromolecules **10**, 2351 (2009).

[6]. M. R. Wertheimer, Plasma Chem. Plasma Process. **34**, 363 (2014).

[7]. J. Goodman, J. Polym. Sci. **44**, 551 (1960).

[8]. A. Fridman, *Plasma Chemistry* (Cambrige University Press, 2008).

[9]. A. Bogaerts, E. Neyts, R. Gijbels, and J. Van der Mullen, Spectrochim. Acta - Part B At. Spectrosc. **57**, 609 (2002).

[10]. H. Rauscher, M. Perucca, and G. Buyle, *Plasma Technology for Hyperfunctional Surfaces* (WILEY-VCH Verlag GmbH & Co. KGaA, 2010).

[11]. E. M. Liston, L. Martinu, and M. R. Wertheimer, J. Adhes. Sci. Technol. **7**, 1091 (1993).

[12]. R. Shishoo, *Plasma Technologies for Textiles* (Woodhead Publishing Limited, 2007).

[13]. K. Vasilev, S. S. Griesser, and H. J. Griesser, Plasma Process. Polym. **8**, 1010 (2011).

[14]. R. Morent, N. De Geyter, T. Desmet, P. Dubruel, and C. Leys, Plasma Process. Polym. **8**, 171 (2011).
[15]. K. N. Kim, S. M. Lee, A. Mishra, and G. Y. Yeom, Thin Solid Films **598**, 315 (2016).
[16]. J. Wang, C. J. Pan, N. Huang, H. Sun, P. Yang, Y. X. Leng, J. Y. Chen, G. J. Wan, and P. K. Chu, Surf. Coatings Technol. **196**, 307 (2005).
[17]. A. Vesel, I. Junkar, U. Cvelbar, J. Kovac, and M. Mozetic, Surf. Interface Anal. **40**, 1444 (2008).
[18]. X. Duan and R. S. Lewis, Biomaterials **23**, 1197 (2002).
[19]. S. Cheruthazhekatt, M. Černák, P. Slavíček, and J. Havel, J. Appl. Biomed. **8**, 55 (2010).
[20]. U. Kogelschatz, Plasma Chem. Plasma Process. **23**, 1 (2003).
[21]. A. J. A. Klomp, G. H. M. Engbers, J. Mol, J. G. A. Terlingen, and J. Feijen, Biomaterials **20**, 1203 (1999).
[22]. Y. Cao, J. Liu, R. Zhong, Q. Yu, and H. Wang, Artif. Cells. Blood Substit. Immobil. Biotechnol. **40**, 317 (2012).
[23]. E. J. Kim, G. D. Yeo, C. M. Pai, and I. K. Kang, J. Biomed. Mater. Res. - Part B Appl. Biomater. **90 B**, 849 (2009).
[24]. T. Xiaoliang and Y. Yonghui, Plasma Sci. Technol. **6**, 2463 (2004).
[25]. H. Gappa-Fahlenkamp and R. S. Lewis, Biomaterials **26**, 3479 (2005).
[26]. M. C. Coen, S. Nowak, L. Schlapbach, M. Pisinger, and F. Stucki, J. Adhes. **53**, 201 (1995).
[27]. B. Gupta, J. Hilborn, C. Hollenstein, C. J. G. Plummer, R. Houriet, and N. Xanthopoulos, J. Appl. Polym. Sci. **78**, 1083 (2000).
[28]. S. F. Miralai, E. Monette, R. Bartnikas, G. Czeremuszkin, M. Latreche, and M. R. Wertheimer, Plasmas Polym. **5**, 63 (2000).
[29]. G. Borcia, C. A. Anderson, and N. M. D. Brown, Surf. Coatings Technol. **201**, 3074 (2006).
[30]. K. Gotoh, Y. Kobayashi, A. Yasukawa, and Y. Ishigami, Colloid Polym. Sci. **290**, 1005 (2012).
[31]. U. Kogelschatz, B. Eliasson, and W. Egli, Le J. Phys. IV **7**, C4 (1997).
[32]. N. Gherardi, G. Gouda, E. Gat, A. Ricard, and F. Massines, Plasma Sources Sci. Technol. **9**, 340 (2000).
[33]. R. Brandenburg, V. A. Maiorov, Y. B. Golubovskii, H. E. Wagner, J. Behnke, and J. F. Behnke, J. Phys. D. Appl. Phys. **38**, 2187 (2005).
[34]. F. P. M. Mercx, Polymer **35**, 2098 (1994).
[35]. W. Urbaniak-Domagala, in *Advanced aspects of spectroscopy*, edited by M. A. Farrukh (InTech, 2012), pp. 85–104.
[36]. J. Nakamatsu, L. F. Delgado-Aparicio, R. Da Silva, and F. Soberon, J. Adhes. Sci. Technol. **13**, 753 (1999).
[37]. A. Vesel and M. Mozetic, Vacuum **86**, 634 (2012).
[38]. R. Morent, N. De Geyter, J. Verschuren, K. De Clerck, P. Kiekens, and C. Leys, Surf. Coatings Technol. **202**, 3427 (2008).
[39]. C. Kan, *A Novel Green Treatment for Textiles: Plasma Treatment as a Sustainable Technology* (CRC Press, 2014).
[40]. A. Zille, F. R. Oliveira, and A. P. Souto, Plasma Process. Polym. **12**, 98 (2015).

[41]. R. A. Jelil, J. Mater. Sci. **50**, 5913 (2015).
[42]. Y. Iriyama, T. Yasuda, D. L. Cho, and H. Yasuda, J. Appl. Polym. Sci. **39**, 249 (1990).
[43]. T. Yasuda, T. Okuno, M. Miyama, and H. Yasuda, J. Polym. Sci. Part A-Polymer Chem. **32**, 1829 (1994).
[44]. E. Krentsel, S. Fusselman, H. Yasuda, T. Yasuda, and M. Miyama, J. Polym. Sci. Part A Polym. Chem. **32**, 1839 (1994).
[45]. C. Riccardi, R. Barni, M. Fontanesi, B. Marcandalli, M. Massafra, E. Selli, and G. Mazzone, Plasma Sources Sci. Technol. **10**, 92 (2001).
[46]. E. Selli, G. Mazzone, C. Oliva, F. Martini, C. Riccardi, R. Barni, B. Marcandalli, and M. R. Massafra, J. Mater. Chem. **11**, 1985 (2001).
[47]. A. Raffaele-Addamo, C. Riccardi, E. Selli, R. Barni, M. Piselli, G. Poletti, F. Orsini, B. Marcandalli, M. Massafra, and L. Meda, Surf. Coatings Technol. **174–175**, 886 (2003).
[48]. S. Sigurdsson and R. Shishoo, J. Appl. Polym. Sci. **66**, 1591 (1997).
[49]. D. Hegemann, Adv. Eng. Mater. **7**, 401 (2005).
[50]. M. A. Keller, G. Fortunato, E. Körner, and D. Hegemann, Plasma Process. Polym. **4**, 1063 (2007).
[51]. E. Bertaux, E. Le Marec, D. Crespy, R. Rossi, and D. Hegemann, Surf. Coatings Technol. **204**, 165 (2009).
[52]. S. Li and D. Jinjin, Appl. Surf. Sci. **253**, 5051 (2007).
[53]. P. Chaivan, N. Pasaja, D. Boonyawan, P. Suanpoot, and T. Vilaithong, Surf. Coatings Technol. **193**, 356 (2005).
[54]. F. Hochart, R. De Jaeger, and J. Levalois-Grützmacher, Surf. Coatings Technol. **165**, 201 (2003).
[55]. M. J. Tsafack and J. Levalois-Grützmacher, Surf. Coatings Technol. **201**, 5789 (2007).
[56]. S. Vaswani, J. Koskinen, and D. W. Hess, Surf. Coatings Technol. **195**, 121 (2005).
[57]. T. Supasai, S. K. Hodak, and B. Paosawatyanyong, **28**, 2 (2007).
[58]. S. K. Hodak, T. Supasai, B. Paosawatyanyong, K. Kamlangkla, and V. Pavarajarn, Appl. Surf. Sci. **254**, 4744 (2008).
[59]. K. Kamlangkla, B. Paosawatyanyong, V. Pavarajarn, J. H. Hodak, and S. K. Hodak, Appl. Surf. Sci. **256**, 5888 (2010).
[60]. J. Vasiljević, M. Gorjanc, B. Tomšič, B. Orel, I. Jerman, M. Mozetič, A. Vesel, and B. Simončič, Cellulose **20**, 277 (2013).
[61]. P. Suanpoot, K. Kueseng, S. Ortmann, R. Kaufmann, C. Umongno, P. Nimmanpipug, D. Boonyawan, and T. Vilaithong, Surf. Coatings Technol. **202**, 5543 (2008).
[62]. D. Sun and G. K. Stylios, J. Mater. Process. Technol. **173**, 172 (2006).
[63]. A. Khoddami, O. Avinc, and S. Mallakpour, Prog. Org. Coatings **67**, 311 (2010).
[64]. G. R. J. Artus, J. Zimmermann, F. A. Reifler, S. A. Brewer, and S. Seeger, Appl. Surf. Sci. **258**, 3835 (2012).
[65]. C. Canal, F. Gaboriau, S. Villeger, U. Cvelbar, and A. Ricard, Int. J. Pharm. **367**, 155 (2009).
[66]. J. Lei, M. Shi, and J. Zhang, Eur. Polym. J. **36**, 1277 (2000).
[67]. K. H. Kale, S. S. Palaskar, and P. M. Kasliwal, Indian J. Fibre Text. Res. **37**, 238 (2012).
[68]. F. Leroux, C. Campagne, A. Perwuelz, and L. Gengembre, Appl. Surf. Sci. **254**, 3902 (2008).

[69]. Y. Y. Ji, H. K. Chang, Y. C. Hong, and S. H. Lee, Jpn. J. Appl. Phys. **47**, 4687 (2008).
[70]. A. Ramamoorthy, A. El-Shafei, and P. Hauser, Plasma Process. Polym. **10**, 430 (2013).
[71]. K. K. Samanta, A. G. Joshi, M. Jassal, and A. K. Agrawal, Surf. Coatings Technol. **213**, 65 (2012).
[72]. D. Parida, M. Jassal, and A. K. Agarwal, Plasma Chem. Plasma Process. **32**, 1259 (2012).
[73]. R. Molina, J. M. Teixidó, C. W. Kan, and P. Jovančić, ACS Appl. Mater. Interfaces **9**, 5513 (2017).
[74]. V. Colombo, D. Fabiani, M. L. Focarete, M. Gherardi, C. Gualandi, R. Laurita, and M. Zaccaria, Plasma Process. Polym. **11**, 247 (2014).
[75]. M. Boselli, V. Colombo, E. Ghedini, M. Gherardi, R. Laurita, A. Liguori, P. Sanibondi, and A. Stancampiano, Plasma Chem. Plasma Process. **34**, 853 (2014).
[76]. M. Boselli, V. Colombo, M. Gherardi, R. Laurita, A. Liguori, P. Sanibondi, E. Simoncelli, and A. Stancampiano, IEEE Trans. Plasma Sci. **43**, 713 (2015).
[77]. A. Liguori, A. Pollicino, A. Stancampiano, F. Tarterini, M. L. Focarete, V. Colombo, and M. Gherardi, Plasma Process. Polym. **13**, 375 (2016).
[78]. A. Liguori, E. Traldi, E. Toccaceli, R. Laurita, A. Pollicino, M. L. Focarete, V. Colombo, and M. Gherardi, *Co-Deposition of Plasma-Polymerized Polyacrylic Acid and Silver Nanoparticles for the Production of Nanocomposite Coatings Using a Non-Equilibrium Atmospheric Pressure Plasma Jet*, Plasma Process. Polym. **13**, 623 (2016), DOI: 10.1002/ppap.201500143, Copyright © 2015 WILEY-VCH Verlag GmbH & Co. KGaA, Weinheim. Reproduced with permission.
[79]. B. H. Stuart, *Infrared Spectroscopy: Fundamentals and Applications* (John Wiley & Sons Ltd, 2004).
[80]. J. Coates, in *Encyclopedia of Analytical Chemistry*, edited by R. A. Meyers (John Wiley & Sons Ltd, Chichester, 2000), pp. 10815–10837.
[81]. G. Socrates, *Infrared and Raman Characteristic Group Frequencies: Tables and Charts*, 3rd ed. (John Wiley & Sons Ltd, 2001).
[82]. A. Milella, F. Palumbo, P. Favia, G. Cicala, and R. D'Agostino, Plasma Process. Polym. **1**, 164 (2004).
[83]. D. Han and S. Y. Moon, Thin Solid Films **587**, 34 (2015).
[84]. Y. Matsuda and H. Yasuda, Thin Solid Films **118**, 211 (1984).
[85]. H. Yasuda, *Plasma Polymerization* (Academic Press Inc., 1985).

3. Design and Development of Processes Assisted by Cold Plasma Sources to Produce Antimicrobial Nanocomposite Coatings

3.1. Literature Overview

Microorganisms were the first life forms to inhabit our planet around 4 billion years ago and, during the years, they have continuously evolved developing new abilities and mechanisms to proliferate in almost every kind of environment. However, this amazing adaptability represents also a critical issue in several industrial and biomedical fields, such as underwater cables, ship hulls, gas pipelines, heat exchangers, water filters, surgical implants, medical devices, ecc. [1,2]. Indeed, bacteria, fungi and other microbes can colonize the surface of the materials employed in these fields adversely affecting their functional properties, thus producing economic losses or health risks [1,2]. In the past this issue has been usually addressed by adopting an active approach, *i.e.* using biocide chemicals or antibiotics to kill the unwanted microorganisms. However, the massive use of these chemical products resulted in increasing water pollution and in the emergence of bacteria resistant to their effects, especially antibiotic-resistant bacteria [3]. A possible strategy investigated by many research groups to reduce the use of biocide chemicals and antibiotics is the realization of antibacterial (or antimicrobial) surfaces [1,2,4–6].

The aim of the antibacterial surfaces is to prevent or at least to reduce the adhesion and colonization of microorganisms on a surface, thus hindering biofilm formation. Biofilm formation is a step process, consisting in the adhesion of microorganisms in a planktonic state to a surface followed by their growth and the production of an extracellular matrix, which makes the microorganisms difficult to be removed or treated [1,7]. Antibacterial surfaces can perform their function adopting two main strategies, also simultaneously: they can resist or prevent the adhesion of the bacteria on the surface or they can actively inactivate the microorganisms causing their death [2]. In the first case the effect is due to the particular surface chemistry

and/or surface morphology, which unfavourably affect the attachment of bacteria [2]. In the second case the surface can induce the death of the microorganisms by means of different mechanisms, *e.g.* the release of biocide chemical agents or the rupture of the cells caused by mechanical interactions at the nanoscale [2]. The surfaces of the first kind can be classified as antibiofouling surfaces, while the ones of the second kind can be classified as bactericidal surfaces [2,6,8].

Great efforts have been devoted to the development of antibacterial coatings adopting different methods and materials for their realization, as reported in several works [1,2,4–6,9,10]. The wet chemical methods, such as sol-gel, spin-coating, dip-coating and electrochemical deposition [11–14], are by far the most commonly employed in this scientific field thanks to their simplicity and flexibility. Indeed, they can be used to obtain a great variety of coatings, from the ones that confer a particular surface chemistry to the substrate (*e.g.* hydrophilic, hydrophobic, oleophobic) to those that release biocide agents. However, the main issue related to the utilization of these methods consists of the extensive use of solvents, thus making them potentially detrimental to the environment, even though they result less polluting than the above mentioned active approaches.

In this perspective, a growing interest has arisen on the production of antimicrobial coatings by means of innovative techniques, especially non-equilibrium plasmas. Indeed, the great number of possible plasma-assisted processes allows adopting different strategies to obtain antimicrobial surfaces, tailoring the morphological and chemical characteristics of the coating without requiring great amounts of chemicals. Some examples of these strategies are the plasma-polymerization of antifouling polymers such as Polyethylene oxide-like (PEO-like) coatings [10,15,16], the grafting of antibacterial molecules like chitosan and quaternary ammonium compounds [8,10,15,16], the nanotexturing of surfaces to confer contact-killing properties or to inhibit bacterial adhesion [17–19], the deposition of coating releasing organic antibiotics or metallic ions acting as biocide agents [8,10,15,16,20]. However, also these approaches present some drawbacks that have to be considered during the development of an industrial process. The deposition of antifouling coatings by means of plasma-polymerization processes has been usually performed with low pressure plasma sources, which require the use of expensive equipment and batch production systems. Also sputtering processes to product layers or nanostructures of antibacterial metals present the same issues. The grafting of antibacterial molecules requires the development of multistep processes and frequently the use of expensive bioactive molecules. The nanotexturing of surfaces is a technology at its early stage of development and it is characterized by very high costs. Finally, it is difficult to achieve

a proper control of the release of biocide agents from nanocomposite coatings, sufficient to inactivate the undesired microorganisms without being harmful for health or environment, while lasting for a long period of time. Therefore, new studies must be performed to further develop and optimize these approaches.

Despite the aforementioned complexity, the production of nanocomposite coatings consisting of metallic or metal oxides nanoparticles (*e.g.* Ag, Cu, ZnO) embedded within a polymeric, inorganic or Diamond-Like Carbon (DLC) matrix has proven to be one of the more valuable and reliable solutions to obtain antimicrobial surfaces by means of plasma-assisted processes [8–10,15,20]. This strategy is based on the bactericidal effects of metallic ions [15,21–23], which are gradually released from the surface of metal or metal oxide nanoparticle through the coating matrix, thus being the main responsible of the antimicrobial effect [22–25]. Bare nanoparticles are rarely employed for this purpose, since they can be toxic for human health and other organisms, especially at high concentrations [26–29]. Therefore, a release of nanoparticles from the treated surface must be avoided, especially if the antimicrobial coating is realized for biomedical applications. This task is carried out by the nanocomposite coating matrix, in which the nanostructures are embedded thus preventing their release. Furthermore, the coating matrix secures also the adhesion of the whole nanocomposite coating to the treated surface.

During my Ph.D. studies I had the opportunity to work on this challenging topic, investigating and developing two different ways to produce antibacterial nanocomposite coatings containing metallic nanoparticles by means of non-equilibrium plasmas, which are reported in this chapter. The first method was carried out by means of two different low pressure plasma sources, using which a copper nanoparticles-hydrocarbon plasma-polymer nanocomposite was prepared. In the second study, an Atmospheric Pressure Plasma Jet (APPJ) was employed to perform a single step co-deposition process, which consists in the simultaneous plasma-polymerization of a monomer and in-flight synthesis of silver nanoparticles (Ag NPs).

3.2. Deposition of a Copper Nanoparticles-Hydrocarbon Plasma-Polymer Nanocomposite Coating by means of Cold Low Pressure Plasma Sources

3.2.1. Introduction

Several studies have been carried out on the realization of nanocomposite antibacterial coatings by means of low pressure plasmas, most of them involving the simultaneous or sequential use of Plasma Enhanced Chemical Vapour Deposition (PECVD) techniques and Physical Vapour Deposition (PVD) techniques [30–50].

PECVD techniques are generally employed to produce the coating matrix: monomers or reactive gases are introduced in the reaction chamber where the physics and chemistry of the plasma discharge induce their fragmentation. These fragments interact with the chemically reactive species of the plasma and then they are deposited on a substrate forming an inorganic or plasma-polymeric film [51]. Moreover, this film can be subjected to ion bombardment during the deposition process further modifying its final characteristics [52].

PVD techniques are mainly employed to produce the metallic nanostructures and are usually carried out by means of sputtering processes, using sources such as asymmetrical Radio Frequency (RF) discharges [30–39], magnetron sources [40–46] and Gas Aggregation Sources (GAS) [47–50]. The first step of the mechanisms governing the formation of nanostructures is the same for all the mentioned sources: the plasma source induces the ionization of the operating gas (generally Ar) and an ion bombardment occurs on the metallic target, from which metallic atoms are ejected. On the contrary, the nucleation and formation of the nanostructures from the ejected atoms could be very different depending on the employed source. In asymmetrical RF discharges and magnetron sources these phenomena are mediated by the interaction of the metallic atoms with the substrate or with the assembling coating, on which diffusion and aggregation processes induce the growth of the nanostructures or eventually metallic films [36,53,54]. In GASs clusters are formed due to the high density of atoms inside the aggregation chamber and then are flown out from the source as a beam of clusters that can be deposited on a substrate [54–56].

This difference in the formation of the metallic nanostructures is relevant also for the properties of the nanocomposite coating: the characteristics of the metallic nanoparticles synthesized using GASs, such as their size, are independent from the coating matrix deposition process. On the contrary, asymmetrical RF discharges and magnetron sources are generally employed performing simultaneously PECVD and PVD, using often a single source for both the processes [30–39,42–44,46]. In this configuration the operating parameters of the two processes are not completely independent and the nanostructures and matrix formation occur at the same time. Therefore, the nanostructures and the matrix mutually influence their growth and, as a consequence, their final characteristics in the nanocomposite coating, even preventing the formation of the metallic nanostructures in some cases [47]. Furthermore, GASs allow to have a better control on the distribution of the metallic clusters inside the matrix, as both homogeneous dispersed nanostructures in the matrix and layered composites can be obtained [47–49]. These differences in the structure of the coatings are represented in Figure 3.1, where a nanocomposite coating obtained from a PECVD-PVD process and from the two possible approaches described for GASs are depicted.

Although GASs present relatively low deposition rates with respect to the other sources [57], their superior capacity to tailor the characteristics and structure of the nanocomposite coating is very interesting for the realization of functional surfaces, such as antibacterial coatings for biomedical implants. Indeed, the effectiveness of these coatings is strictly dependent from their characteristics: the release of metallic ions in the surrounding media must be controlled and prolonged to ensure the antibacterial efficacy of the coating over time [8,33,34,39], and a good adhesion of the nanocomposite coating on the treated surface must be obtained [58–60].

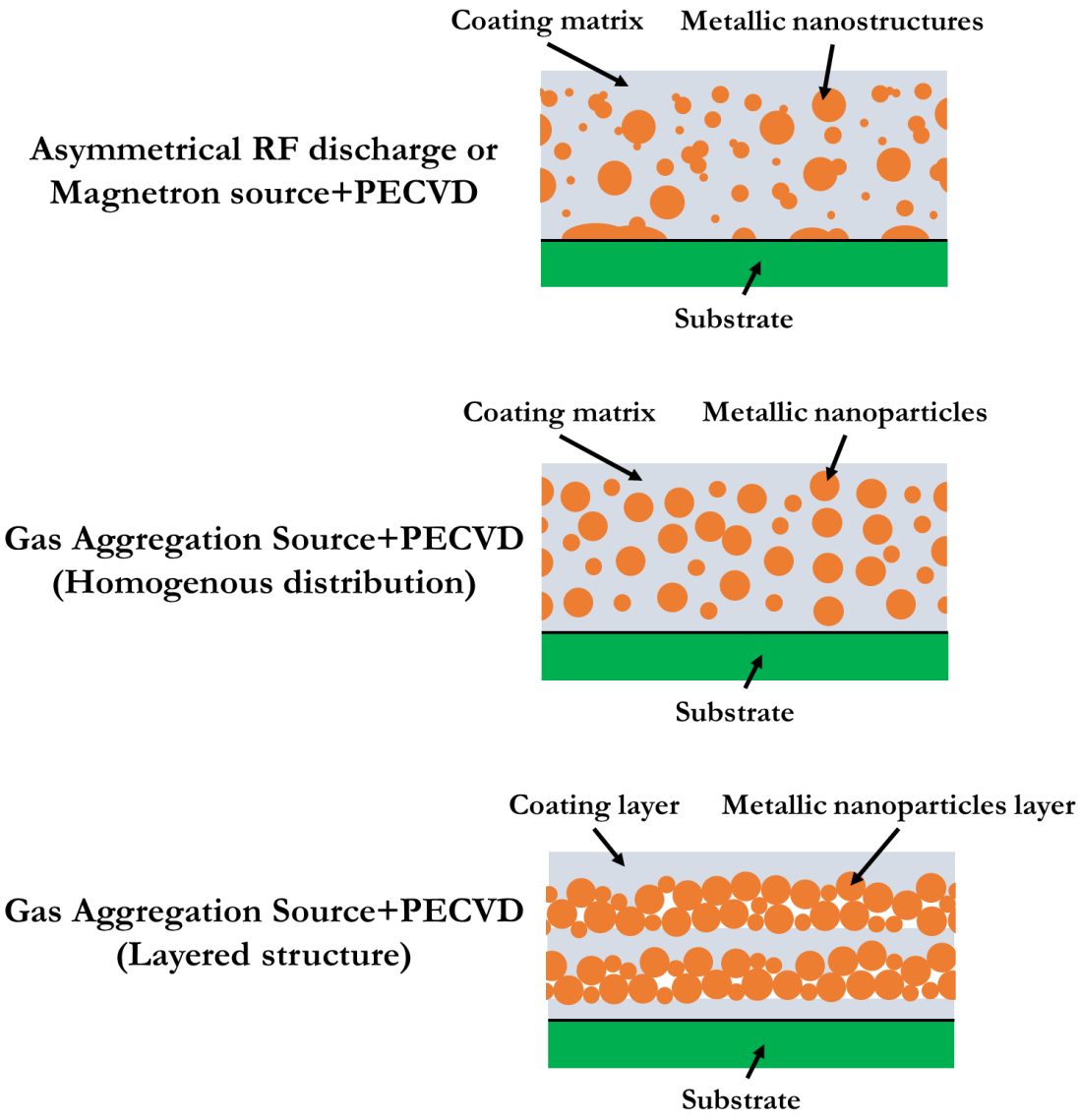

Figure 3.1. Different structure of nanocomposite coatings obtained employing different deposition strategies. From top to bottom: coating obtained employing simultaneously asymmetrical RF discharges or magnetron sources and PECVD technique, coating obtained employing simultaneously GAS and PECVD technique, coating obtained employing sequentially GAS and PECVD technique.

In this perspective, a preliminary study on the deposition of nanocomposite coatings consisting of a hydrocarbon (C:H) thin film covering copper nanoparticles (Cu NPs), was carried out by means of low pressure plasmas and it is presented in the following paragraphs. Cu NPs were deposited on Polyether ether ketone (PEEK) substrates using a GAS and then were covered by a thin layer of a C:H polymer deposited by a PECVD system. The samples so obtained were characterized by means of UV-Vis spectroscopy and Atomic Force Microscopy (AFM) to investigate their chemical and morphological characteristics, respectively, before and after being immersed in water. This activity was carried out in the Group of Physics of Thin Films

and Surfaces of the Department of Macromolecular Physics (Faculty of Mathematics and Physics, Charles University, Prague), where I spent a period of my Ph.D. studies as visiting fellow.

3.2.2. Materials and Methods

PEEK foils were employed as substrates for the deposition of the Cu NPs, which were deposited employing a GAS, depicted in Figure 3.2. The aggregation chamber of the GAS consisted of a water cooled Stainless steel (SS) cylinder, with an aggregation zone 100 mm long and with an inner diameter of 100 mm, ending in a conic nozzle whose orifice has a diameter of 1.5 mm. A DC planar magnetron source, operated at 200 mA, 290 V in constant current regime, was employed to sputter a 3" diameter Cu target (3 mm thick, purity grade ≥ 99,99%). Ar (purity grade 99.99%) was employed as working gas, keeping the operating pressure inside the aggregation chamber constant at 41 Pa. The distance between the substrates and the orifice of the GAS was 250 mm and the deposition time was 2 minutes.

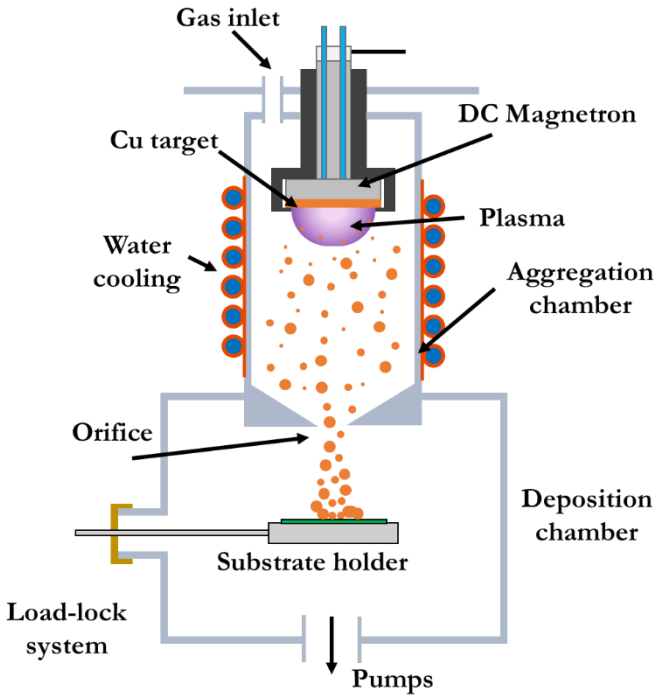

Figure 3.2. Experimental setup adopted for the deposition of Cu NPs.

The samples coated by the Cu NPs were then moved to another setup in which the Cu NPs were coated by a C:H plasma-polymer deposited by means of the PECVD system represented in Figure 3.3. The process was carried out in a SS deposition chamber which was pumped down to a pressure below 0.01 Pa by means of rotary and diffusion pumps before performing the coating deposition. A mixture of Ar (purity grade 99,99%) and n-hexane with a 7:1 ratio determined by their partial pressures was introduced inside the reactor reaching a total pressure of 5.5 Pa. A circular water-cooled SS electrode with a diameter of 81 mm, placed 50 mm distant from the substrate to be coated, was connected through a matching-network to a RF generator operated at frequency 13.56 MHz, with an applied power of 70 W.

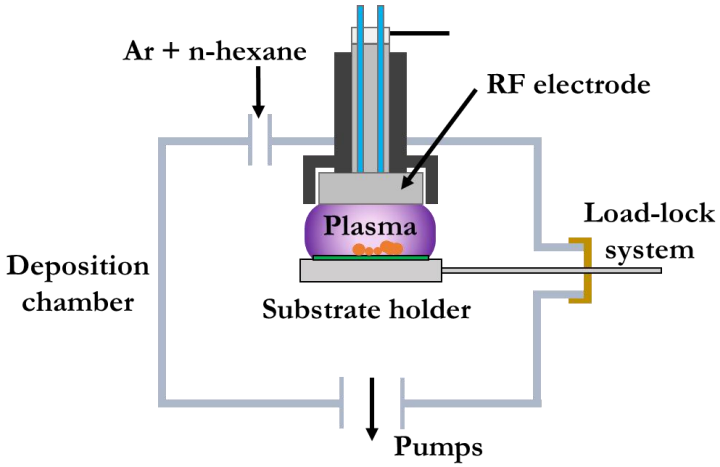

Figure 3.3. Experimental setup adopted for the deposition of C:H plasma-polymer.

A variable angle wavelength ellipsometer (Woollam M-2000) was employed to measure the thickness of a C:H plasma polymer film deposited on a silicon wafer for 10 minutes. In this way it was possible to evaluate the deposition rate of the PECVD process and consequently to define the deposition time required to obtain a C:H layer of a desired thickness over the nanoparticles. Once realized, the nanocomposite coating was characterized using an UV-Vis spectrophotometer (Hitachi U-2900) to study the potential effects of water on the state (metallic or oxidized) of the Cu NPs by evaluating their Localized Surface Plasmon Resonance (LSPR) absorption band. Indeed, the analysis was performed on as made samples and on samples previously immersed in deionized water for different time intervals (1 day, 2 days, 4 days and 7 days), which were dried before being characterized. Furthermore, AFM (NT-MDT Ntegra Prima), operating in semi-contact mode with standard silicon cantilever (Multi75Al-G, force constant 3 N/m, Budget Sensors), was employed to evaluate potential modifications in the

morphology of samples as made and immersed in deionized water for 7 days. In the last case, the sample was dried before being analysed.

3.2.3. Results and Discussion

The deposition rate of the PECVD process was obtained by measuring with the ellipsometer the thickness of the C:H plasma-polymer film covering the silicon wafer, and it resulted to be approximately 8 nm/min. Therefore, a deposition time of 300 s was chosen to perform the deposition of the C:H plasma polymer film over the CuNPs, given that an overlayer of 40 nm should ensure a good adhesion of the nanoparticles on the substrate and avoid their release.

The UV-Vis spectra of the samples so obtained on PEEK substrates are reported in Figure 3.4. The strong absorption occurring below 400 nm, especially in the UV region, is characteristic of the PEEK substrate, while the weak absorption band around 600 nm could be related to the Cu NPs' LSPR band [61–63], whose position and width are dependent from the nanoparticles' dimensions, inter-particles distance and their surrounding medium [64,65]. The coating is almost transparent for the analysed wavelengths, as observed from the spectrum of PEEK foil covered by a layer of C:H coating 10 nm thick (Figure 3.5). The absorption band of Cu NPs gradually decreases once the sample is immersed in water: this can be explained by the fact that the water can penetrate inside the coating and can interact with the metallic Cu NPs oxidizing their surface [66]. Indeed, it has been reported that the oxidation of Cu NPs induce a reduction of the characteristic LSPR peak or band in UV-Vis spectra [62,67]. The measured spectra suggested that the surface of the nanoparticles is completely oxidized after 7 days of immersion, as the LSPR band has completely disappeared at that time (Figure 3.4). These results confirm that the water can effectively interact with the Cu NPs oxidizing them, that is a preliminary condition for the release of copper ions, responsible of the antibacterial effects [24,66]. Since nanoparticles are initially in the metallic state, we can expect that the release of Cu^{2+} from the matrix will gradually increase in the first 7 days as the surface of all the Cu NPs will not be completely oxidized up to that moment.

The morphology of the coating wasn't affected by the immersion in water, as observed from AFM images in Figure 3.6. Indeed, the nanoparticles covered by the C:H coating can be recognized also after water immersion, without relevant differences in their distribution or dimension, as confirmed also by the roughness (RMS) which is almost the same (16 nm and 15

nm before and after immersion in water, respectively). Furthermore, no detachments of the nanocomposite coating from the substrate were observed, thus confirming its stability in water.

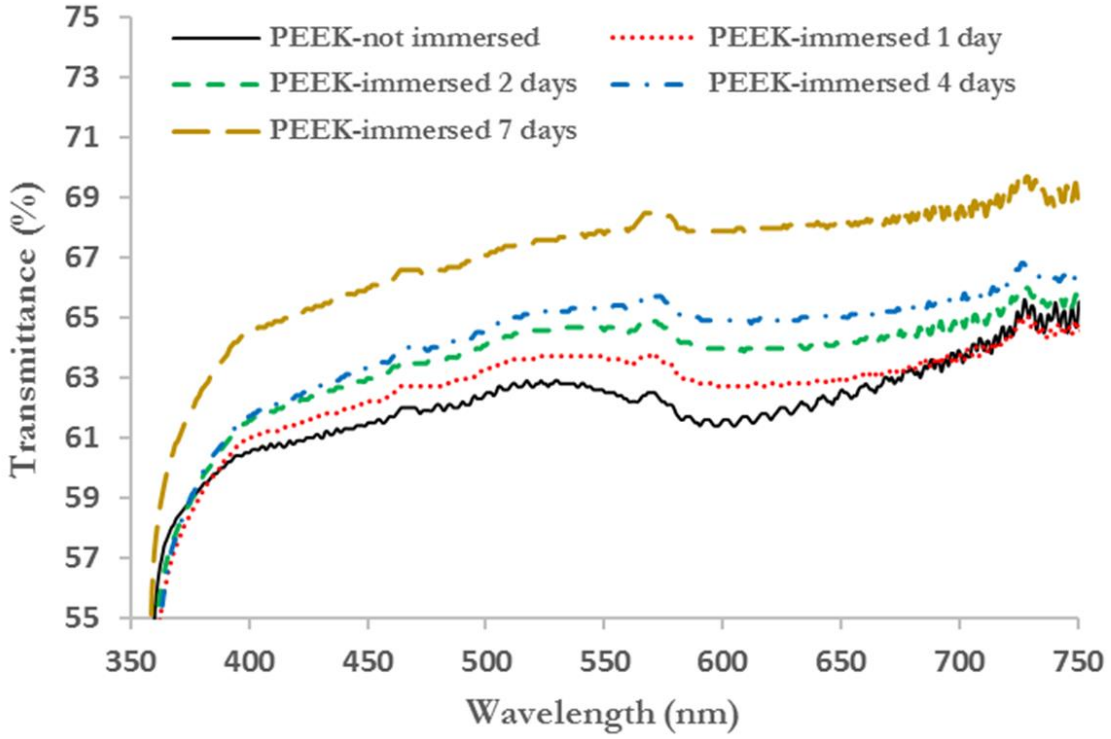

Figure 3.4. UV-Vis spectra of the nanocomposite coatings after being immersed in water.

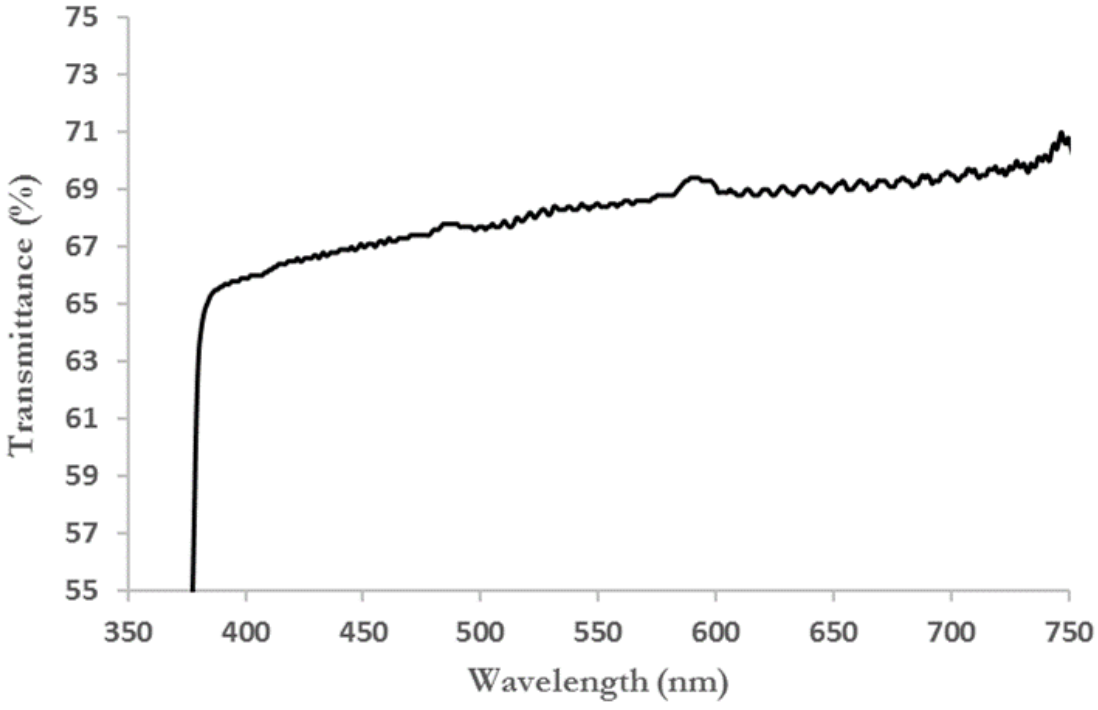

Figure 3.5. UV-Vis spectrum of a PEEK foil covered by 10 nm of the C:H coating.

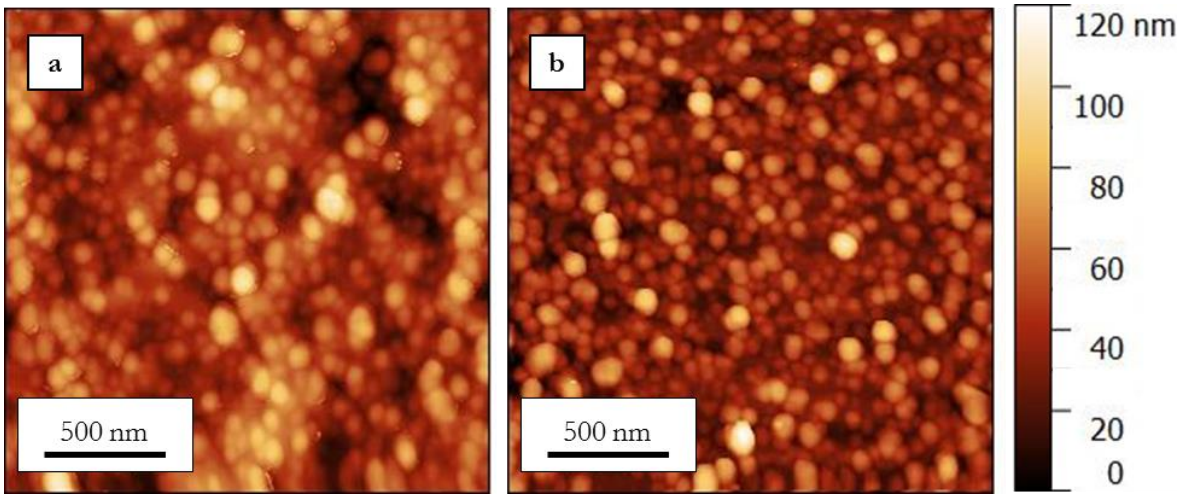

Figure 3.6. AFM images of the nanocomposite coating before (a) and after being immersed in deionized water for 7 days (b).

3.2.4. Conclusions

In this chapter the study of the characteristics of a nanocomposite coating consisting of a thin film of Cu NPs covered by a C:H plasma-polymer layer is presented. Cu NPs were deposited on PEEK substrates using a GAS and then covered by a C:H plasma-polymer deposited in a PECVD system. UV-Vis spectroscopy allowed to observe the progressive decrease of the Cu NPs' LSPR absorption band due to the oxidation of metallic Cu that occurred once the samples were immersed in water. This behaviour confirmed the interaction between water and the nanoparticles covered by the C:H plasma-polymer matrix and suggested the effective release of copper ions in the liquid medium, which is fundamental to achieve antibacterial properties. Furthermore, water immersion didn't affect the morphology of the coating, as assessed by AFM. However, further studies should be performed to understand its antibacterial potential and fully characterize its surface chemistry and morphology.

3.3. Co-deposition of Nanocomposite Coatings Containing Silver Nanostructures by means of a Non-Equilibrium Atmospheric Pressure Plasma Jet

3.3.1. Introduction

The production of nanocomposite thin coatings for antibacterial surfaces by means of low pressure plasmas and the capability to finely tailor the characteristics of the coatings by means of this technology has been presented in the previous chapter. However, as previously written, low pressure plasmas lack of the CAPs' flexibility which makes CAPs more easily implementable in industrial production lines.

In this perspective, research studies have been carried out on the deposition of nanocomposite coatings using non-equilibrium Atmospheric Pressure Plasma Jets (APPJ) [22,58,68–74]. Indeed, non-equilibrium APPJs are particularly interesting with respect to other atmospheric plasma sources, since they can be easily used to treat 3D surfaces and their scalability can be obtained realizing arrays of plasma jets [75–77]. Focusing on the literature, different approaches have been adopted to realize antibacterial nanocomposite coatings. Pfuch *et al.* have obtained antibacterial coatings using the APPJ BLASTER MEF system (TIGRES, Rellingen, Germany) [58,71–73], which generates a non-equilbirum plasma characterized by a gas temperature of 200÷300°C [73]. By introducing Hexamethyldisiloxane (HMDSO) vapours and a silver nitrate ($AgNO_3$) nebulized solution into the plasma discharge, the process allowed to perform simultaneously the synthesis of Ag NPs and the deposition of SiOx coatings, thus realizing a nanocomposite coating in which Ag NPs were embedded in a SiO_x matrix [58,71–73]. Indeed, it has been demonstrated that plasma sources can be employed to produce Ag NPs trough the reduction of Ag^+ in liquid solutions [78,79]. The process has been carried out also introducing copper nitrate, zinc nitrate solutions [73] and a Ag NPs suspension [72] as precursors of the metallic nanostructures inside the coating. Deng and co-workers have thoroughly studied the deposition of organosilicon coatings containing NPs on non-woven fabrics adopting a three step approach [22,69,70]. Firstly, the substrates are coated with an organosilicon thin film, then they are immersed in a suspension of NPs (Ag, Cu, ZnO) and dried, finally another organosilicon

thin film is deposited, thus effectively immobilizing the NPs and controlling the ion release. They have also produced antibacterial coatings in a single step process, introducing tetramethyldisiloxane (TMDSO) and Ag NPs (not in suspension) directly in the APPJ [68].

My colleagues and I have already worked on the production of antibacterial coatings using a non-equilibrium APPJ [74]. Nanocomposite coatings were produced employing the setup reported in Figure 3.7: acrylic acid vapours and a suspension of Ag nanopowders were introduced in a dual gas plasma jet thus depositing in a single step the plasma-polymerized polyacrylic acid (pPAA) and the Ag NPs [74]. Ag NPs and Ag NPs aggregates embedded in the pPAA matrix, characterized by a significant retention of carboxylic groups (21%), were observed [74]. Furthermore, agar disk diffusion tests were performed (using *Escherichia coli*), assessing the antibacterial properties of the nanocomposite coatings (Figure 3.8) [74].

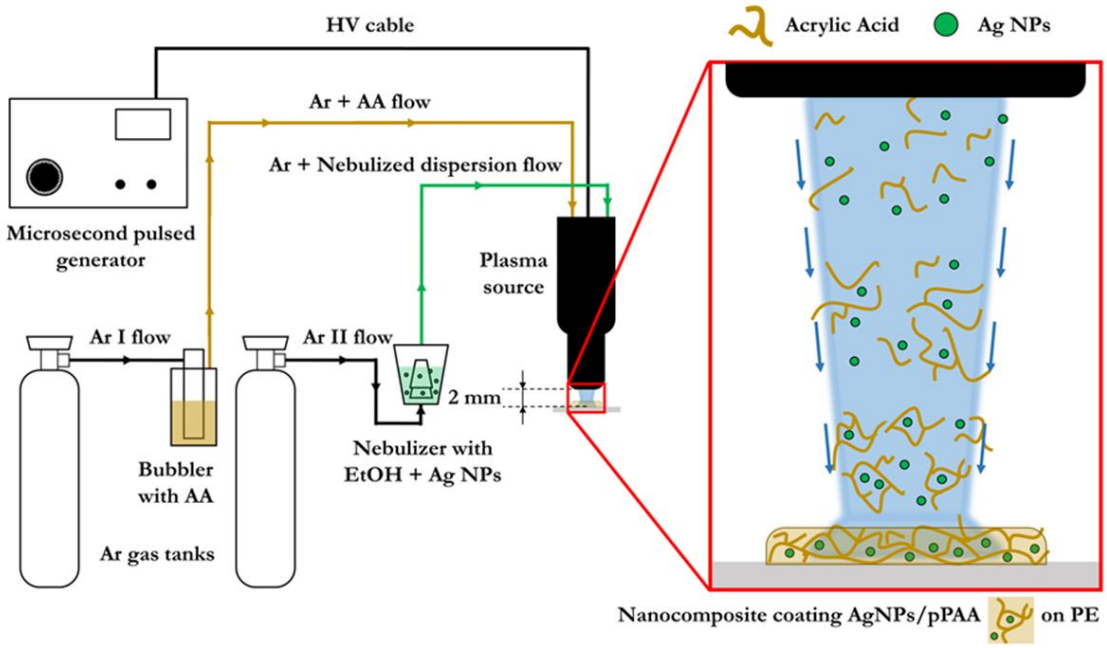

Figure 3.7. Experimental setup employed for the co-deposition process of Ag NPs/pPAA nanocomposite coating [74].

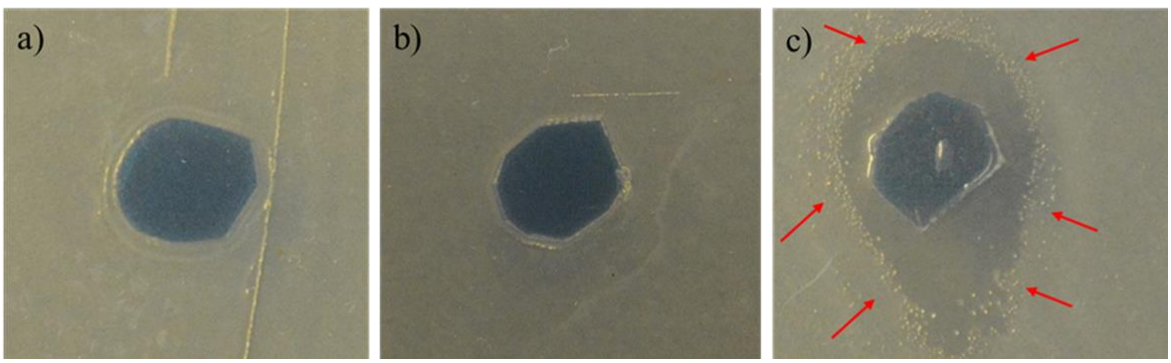

Figure 3.8. Growth inhibition zones of *E. coli* on TSA plates with uncoated substrate (a), pPAA coated substrate (b), and 5% Ag NPs/pPAA coated substrate (c) [74].

However, this approach presents some aspects that could be critical for its industrial implementation, such as the safety issues due to the employment of already fabricated Ag NPs. Furthermore, the direct injection of NPs in the plasma discharge seems to induce their aggregation, as observed in our study and in the work of Deng *et al.* [68], with a reduction of the silver ions release and consequently of the efficiency of the co-deposition process [25].
In this perspective, an approach similar to the one of Pfuch *et al.* reported above [58,71–73], based on the use of a $AgNO_3$ solution as precursor of the Ag NPs, was adopted to perform the in-flight synthesis of Ag NPs and the co-deposition process of nanocomposite coatings. A corona jet, whose design was based on the dual gas plasma jet previously developed by the author's research group [74,80–83], was realized to carry out these processes. Firstly, a feasibility study of the in-flight synthesis and deposition of Ag nanostructures from a nebulized aqueous $AgNO_3$ solution was carried out using the corona jet. Once deposited the Ag structures were analysed by means of Scanning Electron Microscopy (SEM) and Energy Dispersive X-ray Spectroscopy (EDS) in order to evaluate their characteristics. Then the co-deposition process of nanocomposite coatings, which consists in the simultaneous plasma-polymerization of organic monomers and in-flight synthesis of Ag NPs, was investigated using the corona jet. A nebulized $AgNO_3$ solution and AA or HMDSO vapours were employed as precursors of the nanocomposite plasma-polymers/Ag NPs coatings, whose chemical and morphological characteristics were investigated by means of Attenuated Total Reflectance-Fourier Transform Infrared (ATR-FTIR) Spectroscopy, SEM and EDS. Furthermore, the stability in water of the prepared coatings was investigated.

3.3.2. In-flight Synthesis and Deposition of Silver Nanoparticles on Glass Substrates Using a Non-Equilibrium Atmospheric Pressure Plasma Jet

3.3.2.1. Materials and Methods

An aqueous 50 mM silver nitrate ($AgNO_3$) solution, prepared using distilled water and $AgNO_3$ (purity grade ≥99,9%, Sigma Aldrich) stirred at room temperature for 10 minutes, was employed as precursor for the Ag NPs. The experimental setup employed to assess the feasibility of the in-flight synthesis of Ag NPs and to perform their deposition on glass substrates is shown in Fig. 3.9. To perform this process (and subsequently the co-deposition

process), a corona jet similar to the dual gas plasma jet developed in the author's research group [74,80–83] was realized (Figure 3.10a), making some changes with respect to that APPJ. A plastic external diffuser that can be mounted on the end of the plasma source was realized to introduce the nebulized solution flow only in the plasma plume, as shown in Figure 3.10b. The corona jet was powered by the HV generator Alma*PULSE* (AlmaPlasma s.r.l.), the Peak Voltage (PV) and the frequency being set to 13.5 kV and 14 kHz respectively. Two argon (99,999%) flows, controlled by a digital flowmeter (EL-FLOW®, Bronkhorst), were employed to sustain the plasma discharge and to carry the nebulized solution in the diffuser and then in the plasma plume. The first Ar flow of 1.7 slpm was introduced directly in the primary gas channel [80] of the corona jet, while the second one of 2.5 slpm passed through the nebulizer filled with 6 ml of the stirred solution and it was then introduced in the diffuser. The glass substrates (microscope slides, BRAND, Germany) were clean in ethanol and dried before the deposition process, which was performed keeping the distance between the substrates and the diffuser fixed at 2 mm. The deposition time was set to 10 minutes. Initially, some samples were prepared to assess if the flow of the nebulized solution in case of plasma not ignited is sufficient to synthesize metallic structures. These samples were prepared using the same operating conditions described before, except for the HV generator which was kept off during the deposition process.

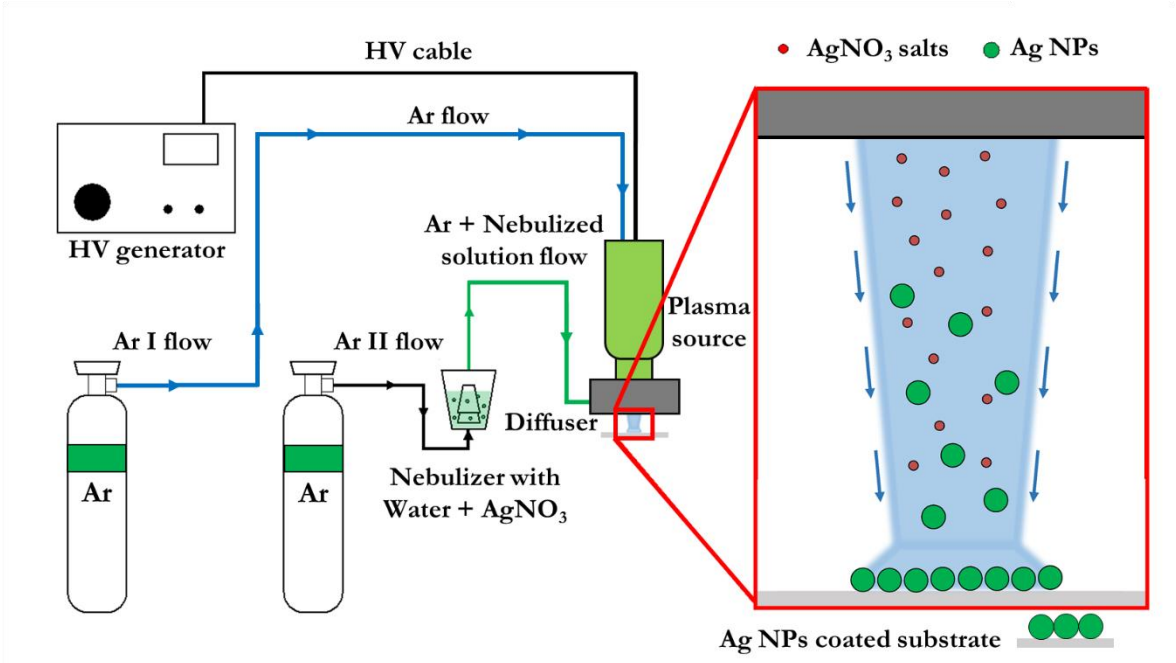

Figure 3.9. Experimental setup to assess the feasibility of the in-flight synthesis of Ag NPs.

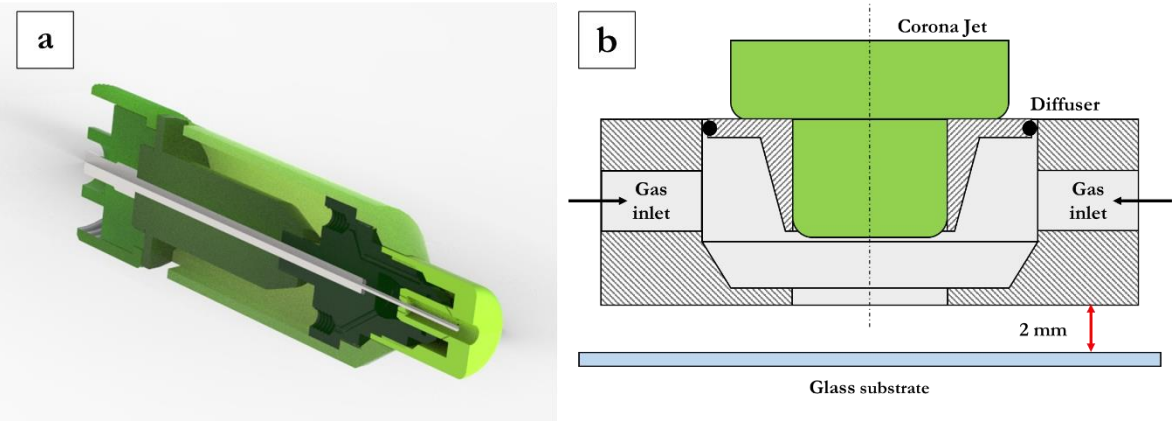

Figure 3.10. Cross-section of the corona jet employed in the experimental setup (a) and cross-section of the external diffuser mounted on the corona jet for the synthesis of Ag NPs (b).

To analyse the morphology and chemistry of the deposited materials, the Ag structures were transferred from the glass substrates onto carbon adhesives covering SEM stubs, placing the glass's treated face in contact with the adhesive and then removing the microscope slide. The samples so prepared were sputter coated with gold and analysed using SEM and EDS (Phenom ProX SEM), applying an accelerating voltage of 15 kV during EDS.

3.3.2.2. Results and Discussion

SEM imaging revealed that Ag structures were present both on the substrates exposed to the effluents of the corona jet when the plasma is not ignited and on those exposed to the plasma plume, as shown in Figure 3.11b and Figure 3.11c respectively. Conversely, the untreated substrates were almost completely clean (Figure 3.11a) except for some randomly distributed powders whose presence can be explained with an external contamination during the handling. Crystals of several microns (Figure 3.11b) and dispersed micrometric and sub-micrometric structures (Figure 3.11c) were observed on the substrates impinged by the flow carrying the aerosol of $AgNO_3$ and on the ones treated by the plasma discharge, respectively. The first ones were probably formed from the evaporation of the droplets of $AgNO_3$ solution, that leaves $AgNO_3$ crystals on the glass substrate, while the second ones consist of agglomerated Ag NPs that were synthesized in the plasma discharge.

The EDS spectra of the two samples confirmed this hypothesis as the nitrogen peak was found only in the crystals and not in the Ag structures deposited by the plasma discharge (Figure 3.12).

The oxygen peak can be related to the oxidation of the Ag NPs, while the carbon peak is due to the carbon adhesive.

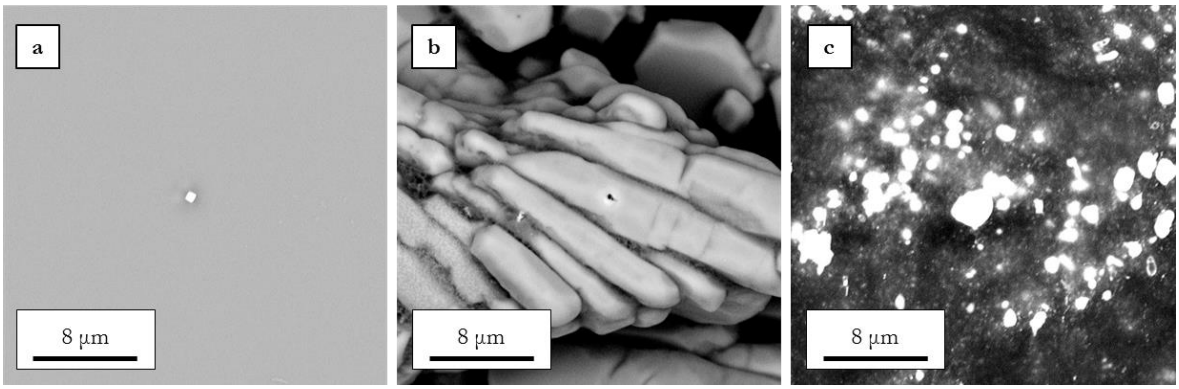

Figure 3.11. SEM images of the deposits transferred from untreated glass substrate (a), glass substrate impinged by the flow carrying the nebulized aqueous $AgNO_3$ solution while the plasma is not ignited (b) and glass substrate treated by the APPJ (c).

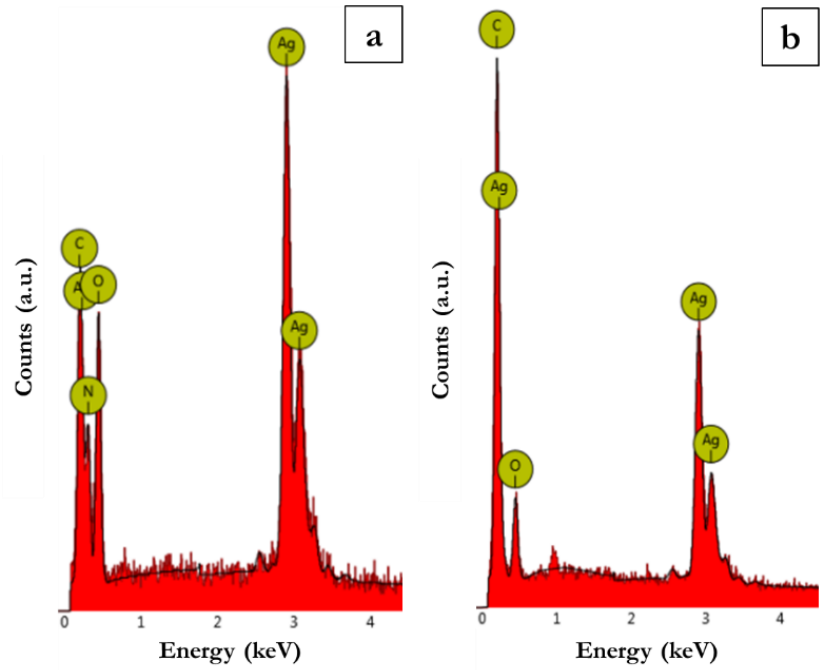

Figure 3.12. Region of the EDS spectra obtained for the deposits transferred from substrate impinged by the flow carrying the nebulized aqueous $AgNO_3$ solution (a) and substrate treated by the APPJ (b).

These results assessed the feasibility of the in-flight synthesis of Ag NPs using the developed corona jet and the external diffuser.

3.3.3. Co-deposition of a Plasma-polymer Matrix Containing In-flight Synthesized Silver Nanoparticles Using a Non-Equilibrium Atmospheric Pressure Plasma Jet

3.3.3.1. Materials and Methods

To perform the co-deposition process of the nanocomposite coatings, consisting of the simultaneous plasma polymerization of a monomer and in-flight synthesis of Ag NPs, the previously presented experimental setup (Figure 3.9) was implemented with a monomer evaporator system (CEM-system, Bronkhorst). The monomer evaporator system consists of a Coriolis liquid flow controller, a mass flow controller for the carrier gas and a controlled mixing and evaporation device, which allows to saturate the gas flow with the liquid vapours at a set value of temperature and to introduce the mixture into the plasma source, as shown in Figure 3.13. A flow of 0.2 g/h of AA (99%, anhydrous and stabilized, Sigma Aldrich) or HMDSO (98%, Sigma Aldrich) was introduced in the monomer evaporator, whose temperature was set at 40°C, and mixed with an Ar flow of 1.7 slpm before being injected in the corona jet primary channel [80]. Small square sheets (30 mm x 30 mm x 3 mm) of reinforced Polyurethane (PU), a polymer widely employed in biomedical devices, were used as substrates and placed at a distance of 2 mm from the diffuser. To produce the nanocomposite coatings, the operating parameters of the HV generator, the Ar flow rate introduced in the nebulizer, the amount of aqueous $AgNO_3$ solution in the nebulizer and the $AgNO_3$ concentration in the solution were not changed with respect to the those employed during the in-flight synthesis and deposition of Ag NPs, reported in 3.3.2.1. The deposition time was set at 5 minutes. In a first phase, depositions of plasma-polymer coatings were carried out, *i.e.* without the simultaneous synthesis of Ag NPs. To perform these depositions no Ar flow was introduced in the external diffuser, while all the other process parameters were the same as previously described.

ATR-FTIR spectroscopy was employed to characterize the chemical structure of the prepared samples. The spectrometer (Agilent Cary 660 FTIR spectrophotometer) was equipped with an ATR sampling accessory, using a diamond crystal as internal reflection element. Spectra were acquired at RT in absorbance mode, from 4000 to 400 cm^{-1} with a resolution of 2 cm^{-1} and a total of 32 scans were acquired for each spectrum. SEM imaging and EDS were also employed to characterize the morphology and the chemistry of the samples as done before. During the characterization an accelerating voltage of 15 kV was applied on the samples which were sputter coated with gold before.

To assess the stability of the coatings, samples were immersed in distilled water, dried and then characterized with ATR-FTIR spectroscopy, SEM imaging and EDS to evaluate possible modifications in their chemistry and morphology.

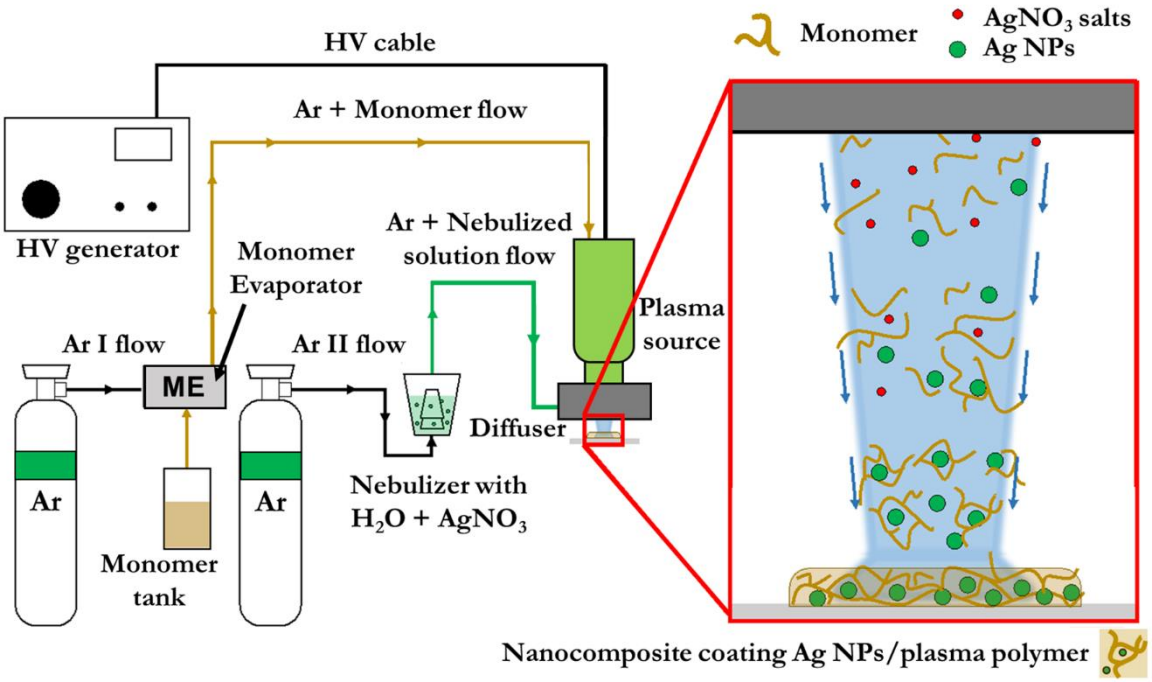

Figure 3.13. Experimental setup to perform the co-deposition process of nanocomposite coatings containing in-flight synthesized Ag NPs.

3.3.3.2. Results and Discussion

The differences between the IR-spectra of PU substrate, Ag NPs/pPAA and Ag NPs/pHMDSO can be observed in Figure 3.14. The IR spectrum of the nanocomposite coatings obtained using pPAA as matrix clearly shows a strong modification of the PU peak around 1700 cm^{-1}, caused by the peak of C=O stretching vibrations characteristic of the carboxylic functional groups at 1714 cm^{-1}, and a very broad band absorption in the region 3600-2400 cm^{-1}, both observed in other pPAA coatings [74,83,84]. Other characteristic features of pPAA coatings, such as the broad band of C-O stretching vibrations around 1335-1135 cm^{-1}, could not be easily recognized due to the complexity of IR spectrum of PU below 1240 cm^{-1}, although a general increase of the intensity is observed for all the peaks. The peaks of PU substrate at 1740 cm^{-1}, 1685 cm^{-1} and 1240 cm^{-1} are strongly affected and reduced by the deposition of AgNPs/pHMDSO coating, as well as the peaks at 2915 and 2855 cm^{-1} that can be related to C-H stretching vibrations [85,86]. The new shape of the absorption peak at 1240 cm^{-1} and the broad band absorption in

the region 3600-3000 cm^{-1} can be associated to the methyl groups of $Si–CH_3$ and to -OH functional groups, respectively [85,87]. Strong absorption bands are present around 1050 cm^{-1}, 900 cm^{-1} and 445 cm^{-1}, which can be associated to different silicon functional groups such as Si–O–C, Si-O-R, Si-OH and Si–O–Si [85]. Since no relevant differences were observed between the IR spectra of the coating made of only pPAA or pHMDSO and their respective nanocomposite coatings, the spectra of the former are not reported in Figure 3.14.

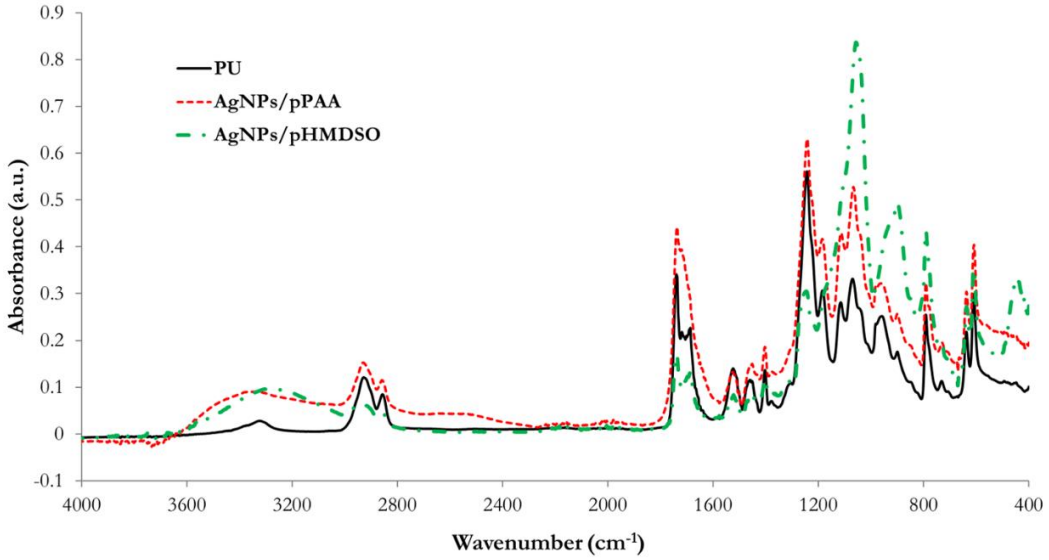

Figure 3.14. IR spectra obtained from the uncoated PU substrates, the Ag NPs/pPAA nanocomposite coating and the Ag NPs/pHMDSO nanocomposite coating.

The analysis of SEM images revealed that the PU substrates are characterized by a complex morphology (Figure 3.15a). Indeed, they present sub-micrometric particles that are the reinforcement fillers of the polymer (white dots in Figure 3.15a) and their surface is not flat, presenting several grooves. The samples coated by pPAA are very similar to the untreated sample and the reinforcement fillers are still visible under the coating (Figure 3.15b and Figure 3.15a). However, Ag NPs/pPAA coatings are clearly different from the untreated substrate: a high density of structures can be observed on the whole surface and some of them are much smaller with respect to the filler particles, thus they can be related to Ag nanostructures (encircled in red in Figure 3.15c). The reinforcement fillers are much less visible when the co-deposition process is performed using HMDSO as precursor (Figure 3.15d and Figure 3.15e). Also, Ag nanoparticles are less visible in the Ag NPs/pHMDSO coated samples with respect to Ag NPs/pPAA coated ones (Figure 3.15e and Figure 3.15c, respectively), even if some Ag nanostructures can be distinguished on the surface of the coating (encircled in red in Figure 3.15e). Furthermore, the surface of pHMDSO and Ag NPs/pHMDSO coated samples seems to be smoother with respect to the one of untreated samples, even if grooves are still detectable as

in Figure 3.15e. The EDS spectra further assessed the presence of Ag nanostructures in both the nanocomposite coatings (Figure 3.16b and Figure 3.16d) and the presence of silicon in the coatings obtained from HMDSO (Figure 3.16c and Figure 3.16d). Some elements, characteristic of the PU substrates and detected by the EDS analysis, are undisclosable and therefore they are not shown Figure 3.16.

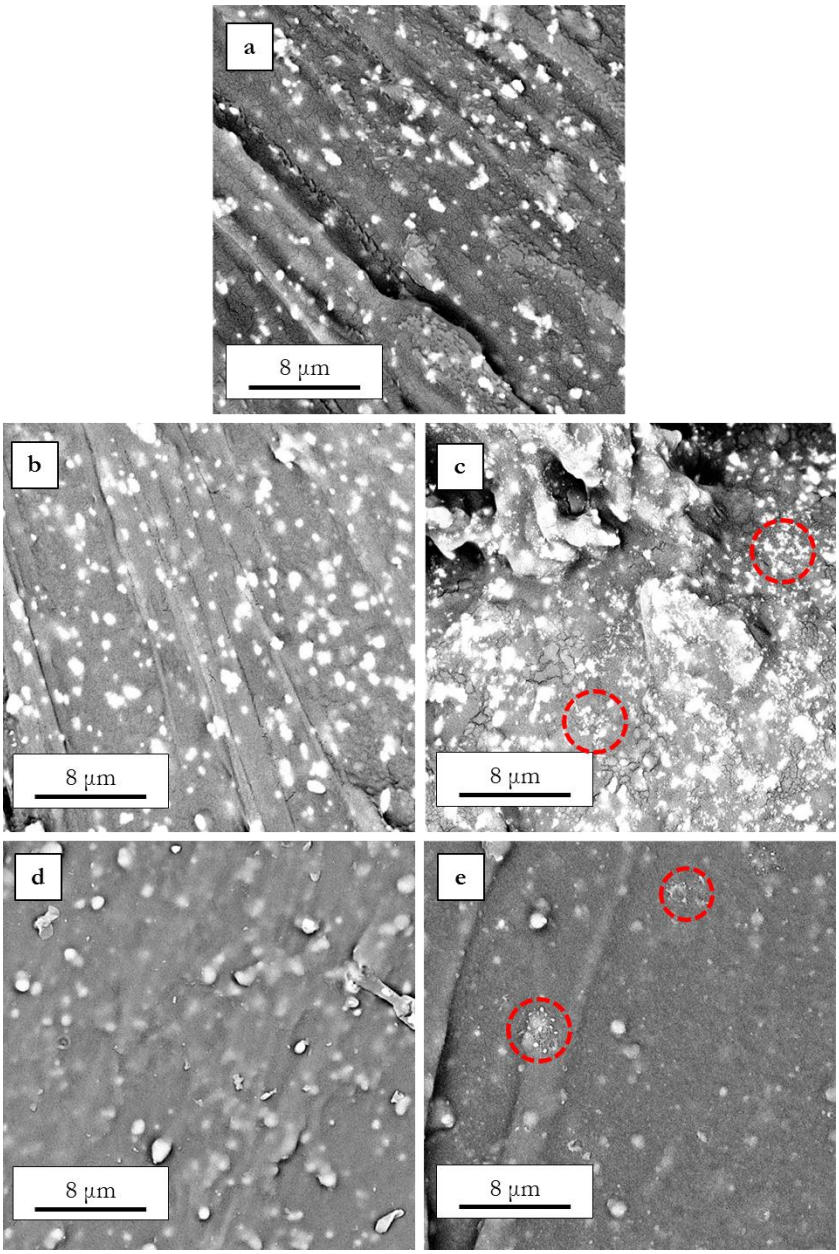

Figure 3.15. SEM images of the untreated PU substrate (a), pPAA coated sample (b), Ag NPs/pPAA coated sample (c), pHMDSO coated sample (d) and Ag NPs/pHMDSO coated sample (e). Some Ag structures and Ag NPs aggregates are circled in red in the nanocomposite coatings.

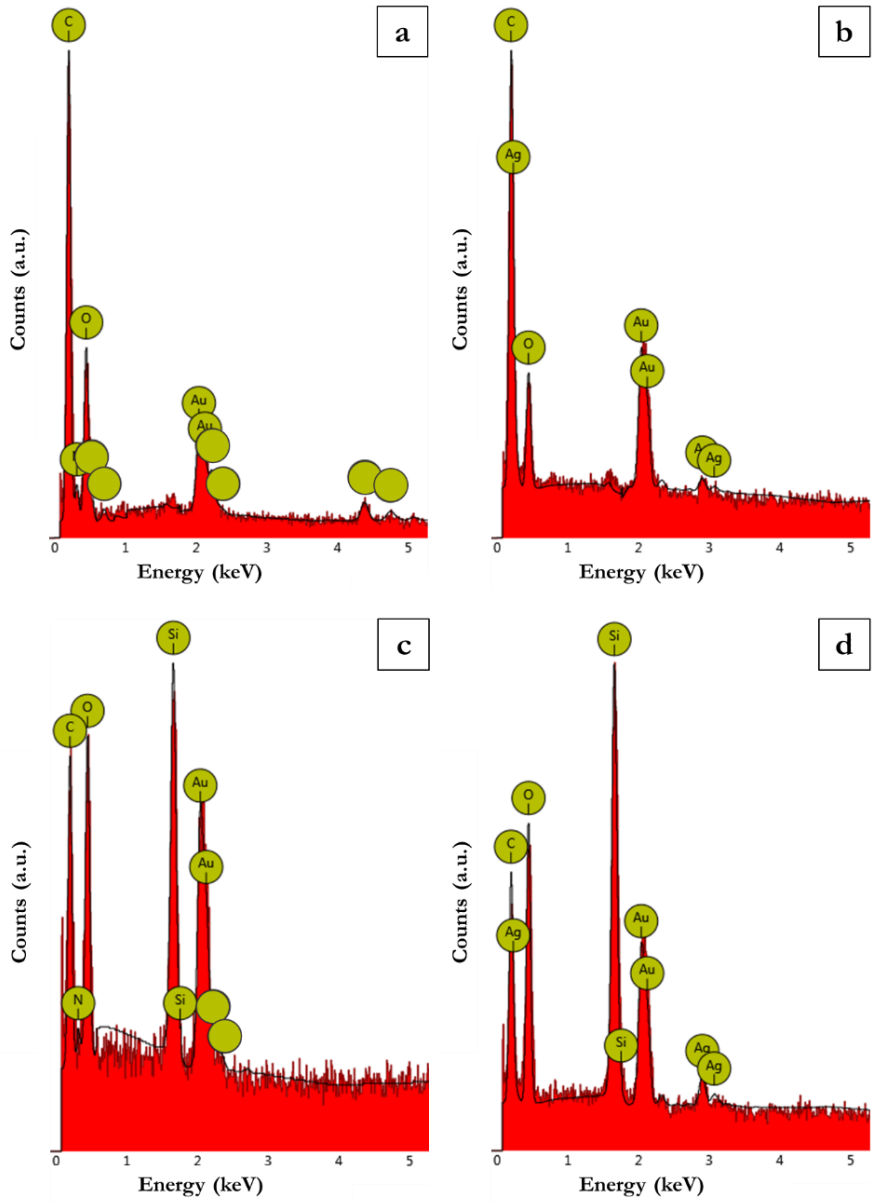

Figure 3.16. Region of the EDS spectra obtained for pPAA coated sample (a), Ag NPs/pPAA coated sample (b), pHMDSO coated sample (c) and Ag NPs/pHMDSO coated sample (d). Some elements, characteristic of the substrate, are undisclosable.

The Ag NPs/pPAA nanocomposite coatings resulted highly soluble in water as confirmed by the IR spectrum of the samples immersed in water for 1 minute, shown in Figure 3.17. As mentioned before, this behaviour is not acceptable for antibacterial coatings to be used in biomedical devices, since Ag NPs need not to be released in the surrounding medium.

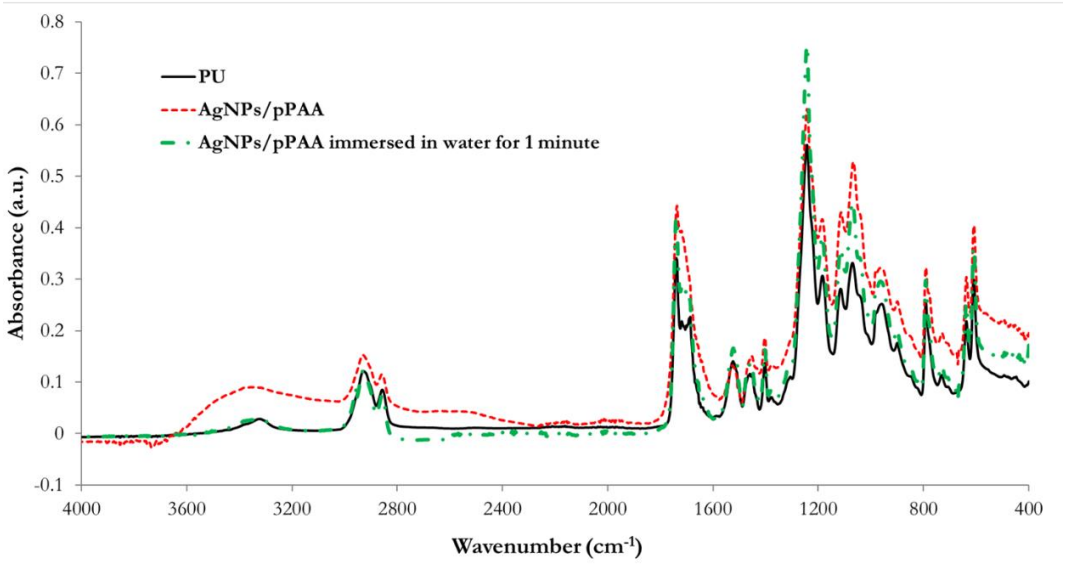

Figure 3.17. IR spectra obtained from the uncoated PU substrates, the Ag NPs/pPAA nanocomposite coating as deposited and the same samples after being immersed in distilled water for 1 minute.

In this perspective, good results were obtained for Ag NPs/pHMDSO coated samples, as the presence of the coating can be clearly assessed by ATR-FTIR spectroscopy after 4 days of immersion (Figure 3.18). However, some absorption peaks and bands were slightly affected after the immersion in water, especially in the regions of 3600-3000 cm^{-1} and 950-900 cm^{-1}.

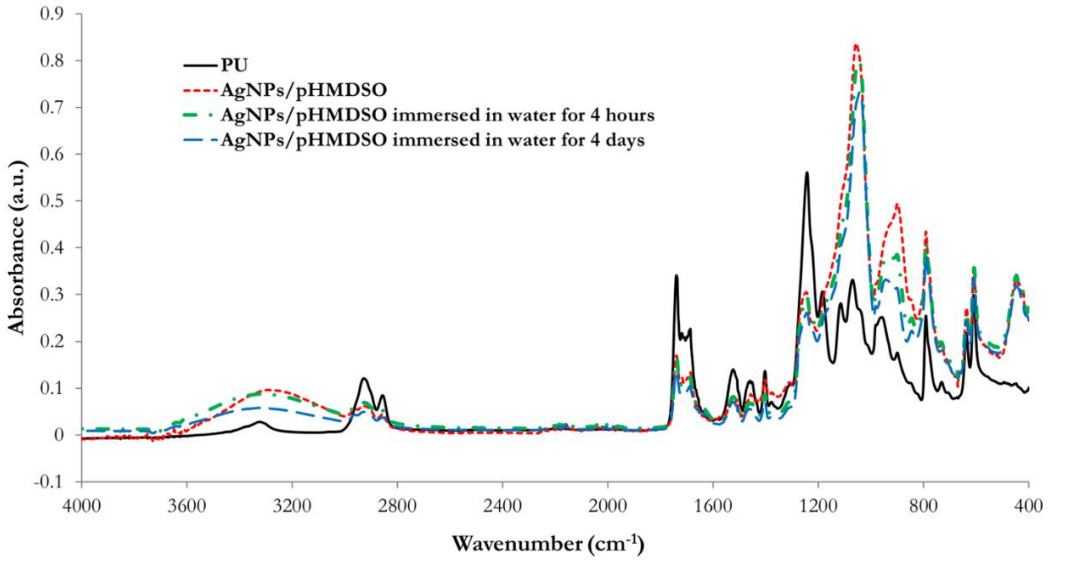

Figure 3.18. IR spectra obtained from the uncoated PU substrates, the Ag NPs/pHMDSO nanocomposite coating as deposited and the same samples after being immersed in distilled water for 4 hours and 4 days.

The organosilicon film is still clearly visible in the pHMDSO coated sample after being immersed in water for 1 day, thus confirming the stability of the polymer (Figure 3.19b).

However, the comparison of the SEM images obtained from the Ag NPs/pHMDSO and the ones for Ag NPs/pHMDSO coated samples immersed in water for 1 day revealed that the morphology of the nanocomposite coating was modified by the interaction with water (Figure 3.19c and Figure 3.19d). Indeed, the Ag nanostructures are no more detectable on the sample's surface, which seems to be made of nanoparticles coated by pHMDSO, dispersed in the matrix and partially protruding from its surface, so causing its particular "roughness" (Figure 3.19d). Furthermore, the surface is much less smooth with respect to the one of the sample which has not been immersed (Figure 3.19d and Figure 3.19c, respectively). These effects can be mainly explained by a limited swelling of the coating and by the removal from the surface of those Ag nanostructures which were not firmly anchored to the polymer matrix. Indeed, the removal of Ag nanostructures is also assessed by the EDS spectra obtained from the coatings, which reveal that the Ag peaks are significantly reduced after the immersion in water (Figure 3.20). This issue can be easily resolved applying a thin layer of pHMDSO on the top of the Ag NPs/pHMDSO nanocomposite coating, similarly to the final step performed in the works of Deng *et al.* [22,69,70], thus avoiding the release of nanostructures from the surface.

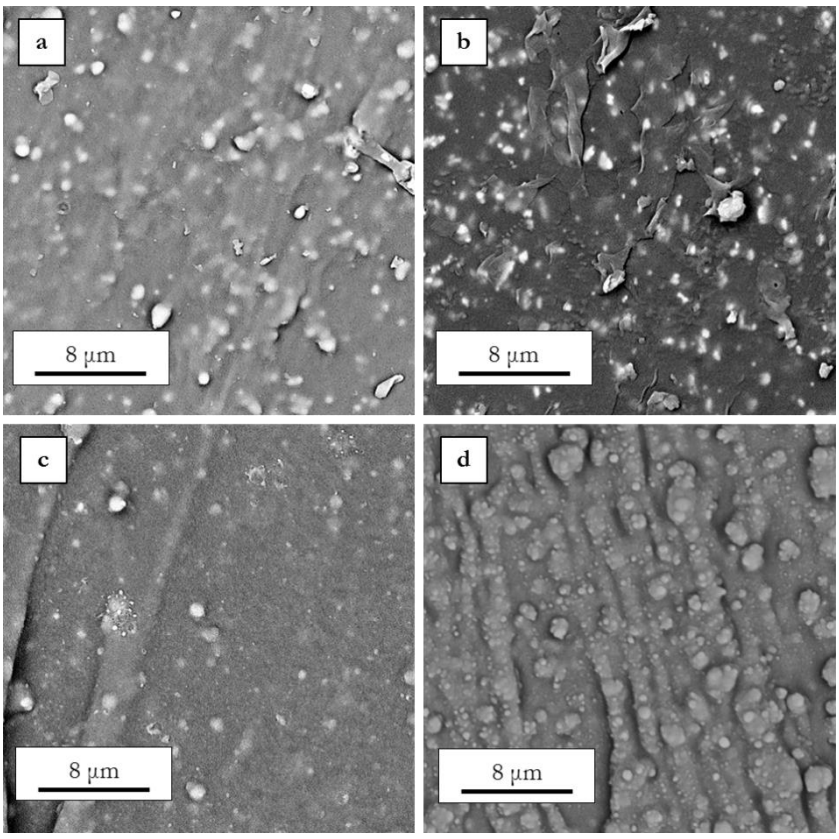

Figure 3.19. SEM images of pHMDSO coated sample (a), pHMDSO coated sample immersed in distilled water for 1 day (b), Ag NPs/pHMDSO coated sample (c) and Ag NPs/pHMDSO coated sample immersed in distilled water for 1 day (d).

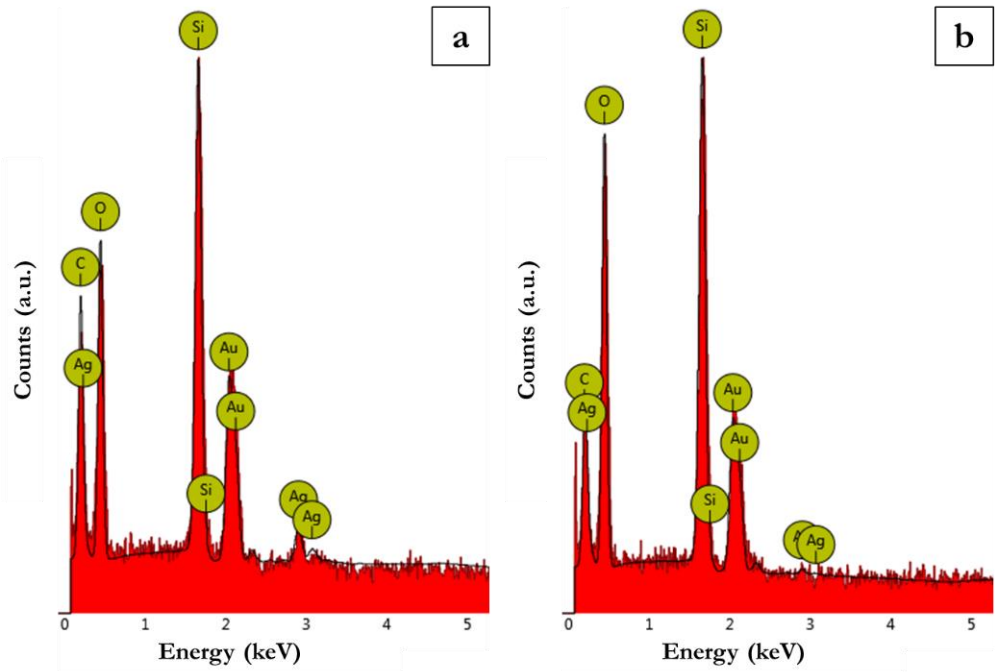

Figure 3.20. Region of the EDS spectra obtained for Ag NPs/pHMDSO coated sample (a) and Ag NPs/pHMDSO coated sample after being immersed in distilled water for 1 day (b).

3.3.4. Conclusions

In this chapter a co-deposition process of nanocomposite coatings containing in-flight synthesized Ag NPs using a corona jet plasma source was described. The first part was concerned on the feasibility study of the in-flight synthesis of Ag NPs by means of the developed corona jet and diffuser, using a nebulized aqueous $AgNO_3$ solution as precursor. The differences between $AgNO_3$ crystals deposited when the plasma is not ignited and the AgNPs particles synthesized by the reduction of Ag ions in the plasma discharge were assessed by SEM imaging and EDS.

Supported by these results, the co-deposition process was performed on PU substrates using two different monomers, AA and HMDSO, as precursors of the nanocomposite coating matrix. ATR-FTIR spectroscopy was employed to reveal the chemical characteristics of the two coatings and to assess their stability in water: while the Ag NPs/pPAA nanocomposite coatings turned out to be water-soluble, the Ag NPs/pHMDSO nanocomposite coatings resulted water-stable, thus being promising for biomedical applications. The morphological differences between the PU substrate, the plasma-polymers coated samples and the co-deposited coated

samples were studied by means of SEM imaging, thus observing the presence of Ag nanostructures in the nanocomposite coatings, as confirmed by the EDS analysis. Furthermore, the comparison of SEM images and EDS spectra obtained for Ag NPs/pHMDSO coated samples before and after water immersion revealed a modification of their morphology and a removal of Ag nanostructures from their surface. This issue can be easily resolved depositing a thin layer of pHMDSO on the surface of the co-deposited coating. Further studies will be necessary to assess the antibacterial efficacy of the coatings and their long-term stability and behaviour, as well as their mechanical properties.

References

[1]. G. D. Bixler and B. Bhushan, Philos. Trans. R. Soc. A Math. Phys. Eng. Sci. **370**, 2381 (2012).
[2]. J. Hasan, R. J. Crawford, and E. P. Ivanova, Trends Biotechnol. **31**, 295 (2013).
[3]. J. L. Martinez, Environ. Pollut. **157**, 2893 (2009).
[4]. A. Makhlouf and D. Scharnweber, *Handbook of Nanoceramic and Nanocomposite Coatings and Materials* (Butterworth Heinemann, 2015).
[5]. K. Vasilev, J. Cook, and H. J. Griesser, Expert Rev. Med. Devices **6**, 553 (2009).
[6]. M. Cloutier, D. Mantovani, and F. Rosei, Trends Biotechnol. **33**, 637 (2015).
[7]. Y. H. An and R. J. Friedman, J. Biomed. Mater. Res. **43**, 338 (1998).
[8]. A. Nikiforov, X. Deng, Q. Xiong, U. Cvelbar, N. DeGeyter, R. Morent, and C. Leys, J. Phys. D. Appl. Phys. **49**, 204002 (2016).
[9]. E. P. Ivanova and R. J. Crawford, *Antibacterial Surfaces* (Springer International Publishing, 2015).
[10]. E. Sardella, F. Palumbo, G. Camporeale, and P. Favia, Materials. **9**, 1 (2016).
[11]. R. Gupta and A. Kumar, Biomed. Mater. **3**, 34005 (2008).
[12]. B. Tomšič, B. Simončič, B. Orel, L. Černe, P. F. Tavčer, M. Zorko, I. Jerman, A. Vilčnik, and J. Kovač, J. Sol-Gel Sci. Technol. **47**, 44 (2008).
[13]. X. Pang and I. Zhitomirsky, Surf. Coatings Technol. **202**, 3815 (2008).
[14]. F. Pishbin, V. Mouriño, J. B. Gilchrist, D. W. McComb, S. Kreppel, V. Salih, M. P. Ryan, and A. R. Boccaccini, Acta Biomater. **9**, 7469 (2013).
[15]. K. Vasilev, S. S. Griesser, and H. J. Griesser, Plasma Process. Polym. **8**, 1010 (2011).
[16]. H. Rauscher, M. Perucca, and G. Buyle, *Plasma Technology for Hyperfunctional Surfaces* (WILEY-VCH Verlag GmbH & Co. KGaA, 2010).
[17]. E. P. Ivanova, J. Hasan, H. K. Webb, G. Gervinskas, S. Juodkazis, V. K. Truong, A. H. F. Wu, R. N. Lamb, V. A. Baulin, G. S. Watson, J. A. Watson, D. E. Mainwaring, and R. J. Crawford, Nat. Commun. **4**, 2838 (2013).
[18]. S. Wu, F. Zuber, J. Brugger, K. Maniura-Weber, and Q. Ren, Nanoscale **8**, 2620 (2016).
[19]. C. Serrano, L. García-Fernández, J. P. Fernández-Blázquez, M. Barbeck, S. Ghanaati, R. Unger, J. Kirkpatrick, E. Arzt, L. Funk, P. Turón, and A. del Campo, Biomaterials **52**, 291 (2015).

[20]. H. Biederman, Surf. Coatings Technol. **205**, S10 (2011).
[21]. J. A. Lemire, J. J. Harrison, and R. J. Turner, Nat. Rev. Microbiol. **11**, 371 (2013).
[22]. X. Deng, A. Yu Nikiforov, T. Coenye, P. Cools, G. Aziz, R. Morent, N. De Geyter, and C. Leys, Sci. Rep. **5**, 10138 (2015).
[23]. H. Palza, Int. J. Mol. Sci. **16**, 2099 (2015).
[24]. N. Cioffi, L. Torsi, N. Ditaranto, G. Tantillo, L. Ghibelli, L. Sabbatini, T. Bleve-Zacheo, M. D'Alessio, P. G. Zambonin, and E. Traversa, Chem. Mater. **17**, 5255 (2005).
[25]. R. Kumar and H. Münstedt, Biomaterials **26**, 2081 (2005).
[26]. R. J. Griffitt, J. Luo, J. Gao, J.-C. Bonzongo, and D. S. Barber, Environ. Toxicol. Chem. **27**, 1972 (2008).
[27]. A. M. Schrand, M. F. Rahman, S. M. Hussain, J. J. Schlager, D. A. Smith, and A. F. Syed, Wiley Interdiscip. Rev. Nanomedicine Nanobiotechnology **2**, 544 (2010).
[28]. A. Sarkar, M. Ghosh, and P. C. Sil, J. Nanosci. Nanotechnol. **14**, 730 (2014).
[29]. S. Chernousova and M. Epple, Angew. Chemie - Int. Ed. **52**, 1636 (2013).
[30]. P. Favia, M. Vulpio, R. Marino, R. D'Agostino, R. P. Mota, and M. Catalano, Plasmas Polym. **5**, 1 (2000).
[31]. D. J. Balazs, K. Triandafillu, E. Sardella, G. Iacoviello, P. Favia, R. Agostino, and H. Harms, in *Plasma Process. Polym.*, edited by R. D'Agostino, P. Favia, C. Oehr, and M. R. Wertheimer (Wiley-VCH, Weinheim, Germany, 2005), pp. 351–372.
[32]. E. Sardella, P. Favia, R. Gristina, M. Nardulli, and R. d'Agostino, Plasma Process. Polym. **3**, 456 (2006).
[33]. E. Körner, M. H. Aguirre, G. Fortunato, A. Ritter, J. Rühe, and D. Hegemann, Plasma Process. Polym. **7**, 619 (2010).
[34]. E. Körner, B. Hanselmann, P. Cierniak, and D. Hegemann, Plasma Chem. Plasma Process. **32**, 619 (2012).
[35]. B. Despax and P. Raynaud, Plasma Process. Polym. **4**, 127 (2007).
[36]. G. Guillemot, B. Despax, P. Raynaud, S. Zanna, P. Marcus, P. Schmitz, and M. Mercier-Bonin, Plasma Process. Polym. **5**, 228 (2008).
[37]. S. Zanna, C. Saulou, M. Mercier-Bonin, B. Despax, P. Raynaud, A. Seyeux, and P. Marcus, Appl. Surf. Sci. **256**, 6499 (2010).
[38]. C. Saulou, B. Despax, P. Raynaud, S. Zanna, A. Seyeux, P. Marcus, J. N. Audinot, and M. Mercier-Bonin, Plasma Process. Polym. **9**, 324 (2012).
[39]. A. Allion-Maurer, C. Saulou-Bérion, R. Briandet, S. Zanna, N. Lebleu, P. Marcus, P. Raynaud, B. Despax, and M. Mercier-Bonin, Surf. Coatings Technol. **281**, 1 (2015).
[40]. U. Schürmann, W. Hartung, H. Takele, V. Zaporojtchenko, and F. Faupel, Nanotechnology **16**, 1078 (2005).
[41]. V. Zaporojtchenko, R. Podschun, U. Schürmann, A. Kulkarni, and F. Faupel, Nanotechnology **17**, 4904 (2006).
[42]. Š. Meškinis, A. Vasiliauskas, K. Šlapikas, G. Niaura, R. Juškenas, M. Andrulevičius, and S. Tamulevičius, Diam. Relat. Mater. **40**, 32 (2013).
[43]. T. Juknius, M. Ružauskas, T. Tamulevičius, R. Šiugždiniene, I. Jukniene, A. Vasiliauskas, A. Jurkevičiute, and S. Tamulevičius, Materials. **9**, (2016).
[44]. A. Daniel, C. Le Pen, C. Archambeau, and F. Reniers, Appl. Surf. Sci. **256**, 82 (2009).
[45]. M. Agarwala, T. Barman, D. Gogoi, B. Choudhury, A. R. Pal, and R. N. S. Yadav, J. Biomed. Mater. Res. - Part B Appl. Biomater. **102B**, 1223 (2014).
[46]. Q. Chen, M. Zhou, Y. Fu, J. Weng, Y. Zhang, L. Yue, F. Xie, and C. Huo, Surf. Coatings Technol. **202**, 5576 (2008).
[47]. T. Peter, S. Rehders, U. Schürmann, T. Strunskus, V. Zaporojtchenko, and F. Faupel, J. Nanoparticle Res. **15**, 1710 (2013).
[48]. J. Hanuš, T. Steinhartová, O. Kylián, J. Kousal, P. Malinský, A. Choukourov, A.

Macková, and H. Biederman, Plasma Process. Polym. **13**, 879 (2016).
[49]. A. Kuzminova, J. Beranová, O. Polonskyi, A. Shelemin, O. Kylián, A. Choukourov, D. Slavínská, and H. Biederman, Surf. Coatings Technol. **294**, 225 (2016).
[50]. M. Vaidulych, J. Hanuš, T. Steinhartová, O. Kylián, A. Choukourov, J. Beranová, I. Khalakhan, and H. Biederman, Plasma Process. Polym. **14**, (2017).
[51]. A. Bogaerts, E. Neyts, R. Gijbels, and J. Van der Mullen, Spectrochim. Acta - Part B At. Spectrosc. **57**, 609 (2002).
[52]. L. Martinu and D. Poitras, J. Vac. Sci. Technol. A Vacuum, Surfaces, Film. **18**, 2619 (2000).
[53]. V. Zaporojtchenko, T. Strunskus, and K. Behnke, **14**, 467 (2000).
[54]. J. Kratochvíl, A. Kuzminova, O. Kylián, and H. Biederman, Surf. Coatings Technol. **275**, 296 (2015).
[55]. H. Haberland, J. Vac. Sci. Technol. A Vacuum, Surfaces, Film. **12**, 2925 (1994).
[56]. K. Wegner, P. Piseri, H. V. Tafreshi, and P. Milani, J. Phys. D. Appl. Phys. **39**, R439 (2006).
[57]. O. Polonskyi, P. Solař, O. Kylián, M. Drábik, A. Artemenko, J. Kousal, J. Hanuš, J. Pešička, I. Matolínová, E. Kolíbalová, D. Slavínská, and H. Biederman, Thin Solid Films **520**, 4155 (2012).
[58]. O. Beier, A. Pfuch, K. Horn, J. Weisser, M. Schnabelrauch, and A. Schimanski, Plasma Process. Polym. **10**, 77 (2013).
[59]. E. Kulaga, L. Ploux, L. Balan, G. Schrodj, and V. Roucoules, Plasma Process. Polym. **11**, 63 (2014).
[60]. E. Kulaga, L. Ploux, and V. Roucoules, Polym. Degrad. Stab. **116**, 1 (2015).
[61]. D. Mott, J. Galkowski, L. Wang, J. Luo, and C. J. Zhong, Langmuir **23**, 5740 (2007).
[62]. P. Kanninen, C. Johans, J. Merta, and K. Kontturi, J. Colloid Interface Sci. **318**, 88 (2008).
[63]. V. K. Abhinav, V. K. Rao, P. S. Singh, and S. P. Karthik, RSC Adv. **5**, 63985 (2015).
[64]. K. A. Willets and R. P. Van Duyne, Annu. Rev. Phys. Chem. **58**, 267 (2007).
[65]. G. H. Chan, J. Zhao, E. M. Hicks, G. C. Schatz, and R. P. Van Duyne, Nano Lett. **7**, 1947 (2007).
[66]. K. Delgado, R. Quijada, R. Palma, and H. Palza, Lett. Appl. Microbiol. **53**, 50 (2011).
[67]. X. Liu, W. Cai, and H. Bi, J. Mater. Res. **17**, 1125 (2002).
[68]. X. Deng, C. Leys, D. Vujosevic, V. Vuksanovic, U. Cvelbar, N. De Geyter, R. Morent, and A. Nikiforov, Plasma Process. Polym. **11**, 921 (2014).
[69]. X. Deng, A. Nikiforov, D. Vujosevic, V. Vuksanovic, B. Mugoša, U. Cvelbar, N. De Geyter, R. Morent, and C. Leys, Mater. Lett. **149**, 95 (2015).
[70]. A. Yu Nikiforov, X. Deng, I. Onyshchenko, D. Vujosevic, V. Vuksanovic, U. Cvelbar, N. De Geyter, R. Morent, and C. Leys, Eur. Phys. J. Appl. Phys **75**, 1 (2016).
[71]. S. Spange, A. Pfuch, C. Wiegand, O. Beier, U. C. Hipler, and B. Grünler, J. Mater. Sci. Mater. Med. **26**, 76 (2015).
[72]. R. Zimmermann, A. Pfuch, K. Horn, J. Weisser, A. Heft, M. Röder, R. Linke, M. Schnabelrauch, and A. Schimanski, Plasma Process. Polym. **8**, 295 (2011).
[73]. S. Gerullis, A. Pfuch, S. Spange, F. Kettner, K. Plaschkies, B. Küzün, P. V Kosmachev, G. G. Volokitin, and B. Grünler, Eur. J. Wood Wood Prod. **76**, 229 (2017).
[74]. A. Liguori, E. Traldi, E. Toccaceli, R. Laurita, A. Pollicino, M. L. Focarete, V. Colombo, and M. Gherardi, *Co-Deposition of Plasma-Polymerized Polyacrylic Acid and Silver Nanoparticles for the Production of Nanocomposite Coatings Using a Non-Equilibrium Atmospheric Pressure Plasma Jet*, Plasma Process. Polym. **13**, 623 (2016), DOI: 10.1002/ppap.201500143, Copyright © 2015 WILEY-VCH Verlag GmbH & Co. KGaA, Weinheim. Reproduced with permission.
[75]. Z. Cao, J. L. Walsh, and M. G. Kong, Appl. Phys. Lett. **94**, 21501 (2009).

[76]. K.-D. Weltmann, R. Brandenburg, T. von Woedtke, J. Ehlbeck, R. Foest, M. Stieber, and E. Kindel, J. Phys. D. Appl. Phys. **41**, 194008 (2008).
[77]. R. Foest, E. Kindel, A. Ohl, M. Stieber, and K. D. Weltmann, Plasma Phys. Control. Fusion **47**, B525 (2005).
[78]. Q. Shi, N. Vitchuli, J. Nowak, J. M. Caldwell, F. Breidt, M. Bourham, X. Zhang, and M. Mccord, Eur. Polym. J. **47**, 1402 (2011).
[79]. V. S. S. K. Kondeti, U. Gangal, S. Yatom, P. J. Bruggeman, V. S. S. K. Kondeti, U. Gangal, S. Yatom, and P. J. Bruggeman, **35**, 61302 (2017).
[80]. V. Colombo, D. Fabiani, M. L. Focarete, M. Gherardi, C. Gualandi, R. Laurita, and M. Zaccaria, Plasma Process. Polym. **11**, 247 (2014).
[81]. M. Boselli, V. Colombo, E. Ghedini, M. Gherardi, R. Laurita, A. Liguori, P. Sanibondi, and A. Stancampiano, Plasma Chem. Plasma Process. **34**, 853 (2014).
[82]. M. Boselli, V. Colombo, M. Gherardi, R. Laurita, A. Liguori, P. Sanibondi, E. Simoncelli, and A. Stancampiano, IEEE Trans. Plasma Sci. **43**, 713 (2015).
[83]. A. Liguori, A. Pollicino, A. Stancampiano, F. Tarterini, M. L. Focarete, V. Colombo, and M. Gherardi, Plasma Process. Polym. **13**, 375 (2016).
[84]. R. Morent, N. De Geyter, S. Van Vlierberghe, E. Vanderleyden, P. Dubruel, C. Leys, and E. Schacht, Plasma Chem. Plasma Process. **29**, 103 (2009).
[85]. G. Socrates, *Infrared and Raman Characteristic Group Frequencies: Tables and Charts*, 3rd ed. (John Wiley & Sons Ltd, 2001).
[86]. J. Coates, in *Encycl. Anal. Chem.*, edited by R. A. Meyers (John Wiley & Sons Ltd, 2000), pp. 10815–10837.
[87]. B. H. Stuart, *Infrared Spectroscopy: Fundamentals and Applications* (John Wiley & Sons Ltd, 2004).

Acknowledgments

In these three years several people have helped me to carry out so many activities and to conclude my Ph.D. studies and this dissertation. Indeed, it would have been impossible to complete my studies without all the suggestions, the assistance and the support they gave me.

First and foremost, I would like to express my gratitude to my supervisor Professor Vittorio Colombo, who convinced me to join the world of scientific research thus giving me the opportunity to experience the many challenging and interesting applications of plasma technology. I thank him also for his several advices and teachings during these years.

I would like to thank the rest of the members of the Research Group for Industrial Applications of Plasmas Matteo, Marco, Anna L., Augusto, Romolo, Anna M., Emanuele, Tommaso, Federica, Filippo and Alina. My thanks for all the time spent together discussing of science, performing experiments, developing new plasma sources and having fun.

Many thanks go to the whole Group of Physics of Thin Films and Surfaces of Charles University, especially to Professor Hynek Biederman and Dr. Ondrej Kylian, who allowed me living a great scientific experience in Prague.

The most important thanks go to my family Giorgio, Silvia, my grandparents and especially my parents, Guido and Elide, who have never stopped to support me in these years. Most of all, my parents' patience, sacrifice and commitment have always been an exemplum for me, without which I would not have been able to achieve these results.

To all those who are here remembered and also to those I forgot, my greatest gratitude.

Enrico Tralldi